

INFORMATION TO USERS

This was produced from a copy of a document sent to us for microfilming. While the most advanced technological means to photograph and reproduce this document have been used, the quality is heavily dependent upon the quality of the material submitted.

The following explanation of techniques is provided to help you understand markings or notations which may appear on this reproduction.

- 1. The sign or "target" for pages apparently lacking from the document photographed is "Missing Page(s)". If it was possible to obtain the missing page(s) or section, they are spliced into the film along with adjacent pages. This may have necessitated cutting through an image and duplicating adjacent pages to assure you of complete continuity.**
- 2. When an image on the film is obliterated with a round black mark it is an indication that the film inspector noticed either blurred copy because of movement during exposure, or duplicate copy. Unless we meant to delete copyrighted materials that should not have been filmed, you will find a good image of the page in the adjacent frame.**
- 3. When a map, drawing or chart, etc., is part of the material being photographed the photographer has followed a definite method in "sectioning" the material. It is customary to begin filming at the upper left hand corner of a large sheet and to continue from left to right in equal sections with small overlaps. If necessary, sectioning is continued again—beginning below the first row and continuing on until complete.**
- 4. For any illustrations that cannot be reproduced satisfactorily by xerography, photographic prints can be purchased at additional cost and tipped into your xerographic copy. Requests can be made to our *Dissertations Customer Services Department*.**
- 5. Some pages in any document may have indistinct print. In all cases we have filmed the best available copy.**

**University
Microfilms
International**

300 N. ZEEB ROAD, ANN ARBOR, MI 48106
18 BEDFORD ROW, LONDON WC1R 4EJ, ENGLAND

8116753

MCGINLEY, JOHN ANDREW

A DIAGNOSTIC STUDY OF CYCLOGENESIS IN THE LEE OF THE ALPS

The University of Oklahoma

PH.D. 1981

**University
Microfilms
International** 300 N. Zeeb Road, Ann Arbor, MI 48106

THE UNIVERSITY OF OKLAHOMA
GRADUATE COLLEGE

A DIAGNOSTIC STUDY OF CYCLOGENESIS
IN THE LEE OF THE ALPS

A DISSERTATION
SUBMITTED TO THE GRADUATE FACULTY
in partial fulfillment of the requirements for the
degree of
DOCTOR OF PHILOSOPHY

By
JOHN A. MCGINLEY
Norman, Oklahoma
1981

A DIAGNOSTIC STUDY OF CYCLOGENESIS IN THE LEE OF THE ALPS

Approved By

Philip K. Smith

John Day

James F. Kimpel

Robert James-Jones

Markus C. Vischler

DISSERTATION COMMITTEE

ACKNOWLEDGMENTS

I would like to express my gratitude to Dr. Yoshi Sasaki who has been for many years my advisor, teacher and friend. He has provided inspiration and discussion and always had faith in me even during difficult times. Thanks are due to Drs. Martin Jischke, Bob Davies-Jones, Jeff Kimpel, and Peter Ray who reviewed the manuscript, made suggestions, and asked some stimulating questions. Thanks also to Dr. Steve Bloom who reviewed the manuscript in its early form, and spent many hours in discussion and commiseration. A special thank you is due to Lynda Hooper who typed the manuscript. To my wife, Sheila, and my children, go appreciation for their understanding during this time. I hope there will be fewer days of working late in the future. I would like to dedicate this work to my parents Helen and Jack McGinley.

This research was supported by grants from the Naval Environmental Prediction Research Facility (N00014-79-C-0758) and the National Science Foundation (ATM 7723111).

ABSTRACT

Rawinsonde and satellite data are assimilated in a three dimensional analysis scheme which couples mass and momentum, and allows computation of vertical motion. This scheme is used to diagnose the characteristics of cyclone development in the lee of the Alps. By allowing the dimensions of the terrain and the data to define the appropriate magnitude of ageostrophic flow and vertical scale, we can obtain horizontal and vertical motion fields which reflect the proper ratio of flow around versus over the Alps. Using quasi-Lagrangian volumes moving with the upper wave and associated baroclinic zone, the evolution of frontal strength, vorticity, and energy is examined for two lee cyclone episodes.

The blocking effect on the cooler air and externally forced vertical motions are shown to increase the mean frontal zone strength as the wave interacts with the Alps.

The lee cyclone passes through distinct stages during its life.

These are:

1. Orographic stage, which is related to conservation of potential vorticity and production of shallow circulations.
2. Rapid development stage, where dynamically forced upward motion and terrain produced downward motion combine to concentrate vorticity at middle levels.

3. Transition stage, where increased thermal advection and movement away from the mountains allows the storm to grow baroclinically.

Evaluation of energy transformations show that mean kinetic energy within the volume (\bar{K}), is converted to perturbation kinetic energy (K'), during the orographic phase. Mean available potential energy (\bar{A}), is converted to perturbation available potential energy (A'), during the frontal strengthening phase. During rapid development, barotropic processes ($\bar{K} \rightarrow K'$) dominate the baroclinic processes ($A' \rightarrow K'$), however both contribute to development. During the transition stage, ($A' \rightarrow K'$) is the primary conversion although barotropic processes still play a role in increasing K' .

LIST OF SYMBOLS AND NOTATION

Variables and constants

a	earth radius
A	available potential energy, cross sectional area of volume
B	Planck function
c_p	specific heat at constant pressure
c_v	specific heat at constant volume
C	eddy viscosity
d	grid distance
f	Coriolis parameter
F	frontal strength, frictional sink
F_i	variational formalism
g	gravitational acceleration
H_0	amplitude of geopotential, scale height
k	wave number
K	Kinetic energy
L	wavelength, characteristic length
L_n	wavelength of twice sampling interval
p	pressure, phase shift
P	potential vorticity
q	mixing ratio
\dot{Q}	adiabatic heating rate
R_d	adiabatic energy

r^*	filter response
R	gas constant
R_g	geostrophic error
R_i	Richardson number
R_0	Rossby number
s	boundary of volume cross section
S	stability, energy source/sink, stretching deformation
t	time
T	temperature
u	west to east velocity
U	scaling for horizontal velocity
v	south to north velocity
x	distance coordinate west to east
y	distance coordinate south to north
z	height above earth
α	weighting factor, specific volume
β	variation of f along y , weighting factor controlling filtering response
γ	lapse rate, measurement error parameter, shape weighting factor
δ	variational operator, divergence
Δ	dynamic scaling parameter
Δ_c	appropriate Δ for Alps
ϵ	efficiency factor, emissivity
ζ	vertical component of relative vorticity
θ	potential temperature

κ	R/c_p
λ	longitude, Lagrange multiplier
π	$-\ln p$
ρ	density
σ	p/p_s vertical coordinate
$\dot{\sigma}$	$d\sigma/dt$
τ	vertical scaling parameter, transmissivity
ϕ	latitude
Φ	geopotential
ψ	geostrophic stream function $\frac{\Phi}{f}$
ω	vertical motion dp/dt
Ω	angular velocity of earth, vertical motion scale, Lagrange multiplier

Notation

(~)	observed data, or grided data fields
(^)	interpolated fields, dynamically adjusted fields
() _r	reference state, rawinsonde
(→)	vector
() _T	top of atmosphere
() _S	surface, satellite
() ₀	constant
()*	nondimensional
()"	ordinary 2nd derivative
() _a	adjusted, ageostrophic
() _c	variables satisfying mass continuity
() _{x,y,p}	partial derivatives
($\overline{\quad}$)	horizontal mean
()'	perturbation

Operators

∇ horizontal gradient

∇^2 horizontal Laplacian

∇_3^2 3 dimensional Laplacian

$\langle \rangle$ pressure integration $\int_{p_t}^{p_s} () \frac{dp}{g}$

$$\overline{(\quad)}^A = \frac{1}{A} \int_A () dA$$

$$(\quad)' = (\quad) - \overline{(\quad)}$$

$$\overline{(\quad)}^S = \frac{1}{S} \oint ds$$

TABLE OF CONTENTS

	Page
ACKNOWLEDGEMENTS	iii
ABSTRACT	iv
SYMBOLS AND NOTATION	vi
Chapter	
I. INTRODUCTION	1
II. THE ANALYSIS SCHEME	11
Background	11
Quality of Data	12
Analysis Errors	14
The Low Pass Filter	16
Satellite Data Assimilation	18
Dynamic Coupling	19
Selection of Parameters	27
Vertical Motion	28
Conservation of Potential Vorticity	33
Summary of Data Analysis	33
III. FRONTOGENESIS, ENERGETICS AND VORTICITY	36
Frontal Zones	36

Chapter	Page
The Frontogenesis Equation	36
Frontal Strength and Available Potential Energy	39
Partitioning of Energy Quantities	43
Vorticity	49
IV. CASE STUDIES AND RESULTS	51
Synoptic Situation	51
Quasi-Lagrangian Volumes	53
Vorticity	74
Energy	90
Baroclinicity and Scale of Lee Cyclone	99
V. Summary.....	104
Stages of Development	105
Conclusions and Recommendations	106
BIBLIOGRAPHY	110
Appendices	
1. ASSIMILATION OF SATELLITE DATA	114
2. DEVELOPMENT OF LOW PASS FILTER	119
3. HORIZONTAL SHAPE MATCHING	121
4. DYNAMIC ADJUSTMENT	122
5. MASS CONSTRAINT, IMPLIED VERTICAL SCALE	125
6. POTENTIAL VORTICITY CONSTRAINT AND GEOSTROPHIC ADJUSTMENT..	130
7. ENERGY TRANSFORMATION EQUATIONS.....	138

CHAPTER I

INTRODUCTION

Mountains of the earth play an important role in definition of world climatology (Trewartha, 1965). This influence extends not only to long term effects such as climates, but to the whole spectrum of time and space scales, from planetary, synoptic and lee waves, to gravity waves and turbulence.

Numerical simulations by many investigators (Bleck, 1977; Trevisan, 1976; Tibaldi et al. 1980) have attempted to isolate effects on middle latitude, large scale meteorological systems by terrain. Such studies are somewhat limited by how the terrain is represented, unknown nonlinear effects and contamination by boundaries. The thrust of these studies has been to simulate lee cyclogenesis, although other effects such as friction, and frontal modification are often seen in the course of the numerical integration.

Another avenue of investigation of terrain effects is the diagnostic approach. Unlike modern physics where theory frequently leads observation, observation of a phenomena and analysis of these observations are the first steps in the development of most meteorological concepts. At the recent Workshop on Mountains and Numerical Integration (European Center for Mid-Range Weather Forecasting), it was resolved to stress the value of observational description and diagnosis of atmosphere-terrain interaction using

available data in regions of interest. Past studies of this type (Hage, 1961; McClain, 1960) have been typically more qualitative than quantitative. As Phillips (1979), Sasaki et al. (1977), Sasaki and McGinley (1978), and Buzzi and Tibaldi (1978) showed, however, use of advanced objective analysis schemes can yield sound quantitative data as well.

The power of objective analysis is its ability to define processes at particular scales through the use of weighting factors which tune the resulting fields. The inherent weaknesses in this approach are the dependence on available data, both areally and temporally, and the subjective nature of weight selection. Development and use of an objective analysis model which minimizes the subjective aspects is a major goal of this paper.

For exploration of atmosphere-terrain interaction, there are abundant potential geographical regions of study. One of the more important and least understood atmospheric problems is the frequent and rapid cyclogenesis in the northern Mediterranean Sea, just south of the Alps. Storm development here has great impact on the populated parts of northern Italy, mainly on shipping and farming. Numerical models have shown a general inability to forecast this phenomenon. From the diagnostician's view this problem is appealing:

1. Europe has a very dense routine upper air network.
2. The mountains have a limited extent, are surrounded by flat terrain, and are populated enough to provide surface and upper air data.
3. The meteorological phenomena is frequent enough so that cyclogenetic events are likely in almost any data set obtained.

A major disadvantage is that the cyclogenesis frequently occurs over

the Mediterranean Sea. The problems of sparse data in this area can be alleviated by assimilation of satellite radiance data, and observation from ships and aircraft. It should be stressed early on as did Buzzi and Tibaldi (1978) in their case study of Alps cyclogenesis, that although the data is dense, it is capable of providing information for only the largest features of Alps-modified flow. Analysis techniques which introduce dynamical consistency into mass and motion fields have been shown to reduce the size of the spacial Nyquist wave up to a factor of two, (Stephens, 1971).

In earlier case studies, Sasaki and McGinley (1978) and Buzzi and Tibaldi (1978) found that the mountains had a profound influence on the strength of the primary zone of baroclinicity (the frontal zone). As the frontal zone passed the mountains a marked increase in frontal strength (measured by $|\nabla\theta|$, where θ is potential temperature) occurred. Prior to the frontal intensification, lee cyclone development was already underway. The combination of strengthening environmental baroclinicity and its collocation with a fully formed circulation would have obvious development potential, even with simple baroclinic theory, (Holton, 1972). Numerical work by Merkiné (1975) and Merkiné and Kalnay-Rivas (1976) showed similar frontal strengthening over an Alps-like barrier. The transition of a lee cyclone from a shallow downward motion dominated system to a more classic baroclinic structure has been documented by Johnson, et al. (1976) and Phillips (1979).

Flow over and around terrain features is governed by fundamental relationships of fluid dynamics on a rotating sphere. If we consider the flow to be inviscid and adiabatic, it must conserve its potential vorticity. If potential vorticity is defined as

$$p \equiv \frac{c_p \nabla_3 \ln \theta}{\rho} \cdot (\nabla_3 \times \vec{v}_3 + 2\vec{\Omega})$$

then

$$\frac{dP}{dt} = 0$$

where C_p is specific heat at constant pressure, θ is potential temperature, $\nabla_3 \times \vec{v}_3$ is the curl of the 3 dimensional velocity vector, $\vec{\Omega}$ is the earth's rotational vector, ∇_3 is the 3 dimensional gradient operator, and ρ is density.

For flow going up and over a very long orographic ridge, the effect of such a conserving principle is that the flow will be deflected to the left as anticyclonic vorticity is created at the ridge. This is in accordance with elevation of isentropic surfaces over the mountain ($|\vec{\nabla}_3 \theta|$ increases) and depression in the lee ($|\vec{\nabla}_3 \theta|$ decreases), and the necessary change in relative vorticity of the parcel, (Hess, 1959; p.252). The net horizontal displacement and variation of the Coriolis parameter with latitude, forces the parcel to oscillate stably as it continues downstream. This is the mechanism of what is termed the lee trough. See Figure I-1.

For an isolated barrier more complex considerations are necessary. Here the air has the possibility of going around the obstacle or over it, or a combination of both.

As shown by Proudman, and confirmed by Taylor (historical review by Morel, 1973), inviscid, incompressible flow has a quasi-two dimensional character in a rotating frame, and will deviate at all levels around even a small obstacle placed at the lower boundary. For the atmosphere at very large scales and terrain of large horizontal extent (small Rossby Number and vertical displacements), a similar phenomenon may be seen. That is, the air tends to flow around rather than over the barrier, even at levels far above

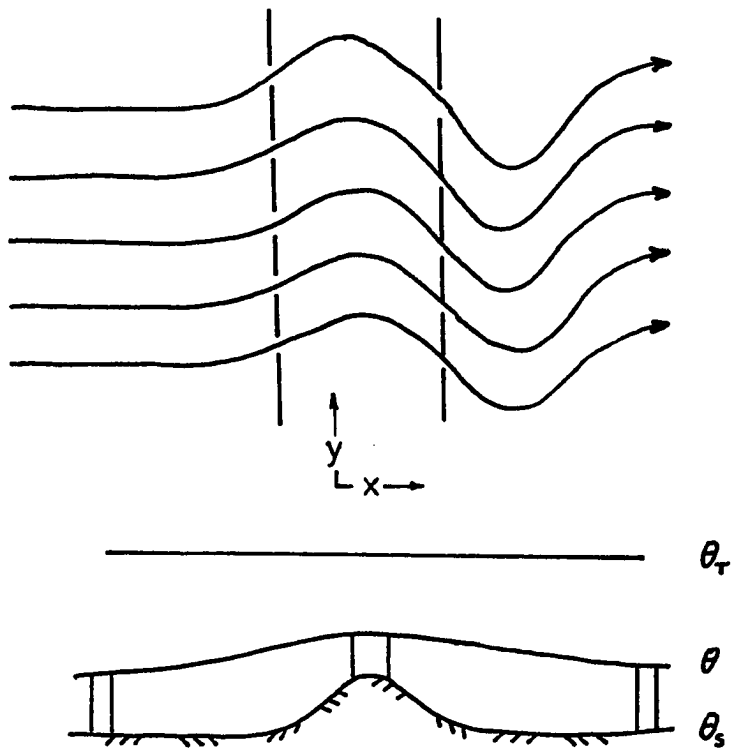


Fig. I-1. Streamlines over a ridge of long transverse extent. Diagram below shows how atmospheric columns reduce height when crossing ridge. θ_r is potential temperature at some layer undisturbed by the terrain; θ_s is at surface; θ at top of column.

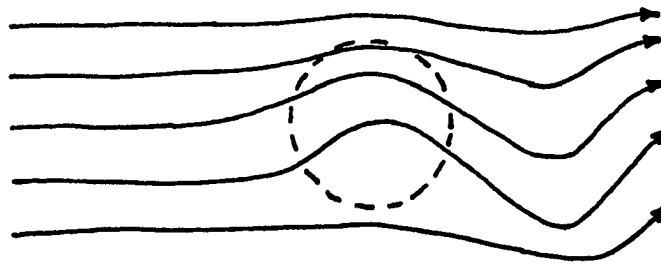


Fig. I-2. Streamlines showing a portion of the flow moving around as well as over an isolated obstacle.

the maximum terrain height. For smaller scales and surface barriers, the flow tends to ride up and over the barrier. To a large degree then, partitioning of this flow into components defining horizontal versus vertical deflections is fundamental to any diagnostic study of airflow over an isolated orographic feature. As discussed in Godske et al. (1957) airflow in the Alps is perturbed typically up to 2-3 km above the highest terrain feature. (This of course discounts short gravitational waves which are known to propagate to very high levels in the atmosphere (Morel, 1973)). This observation illustrates what we are dealing with in airflow over the Alps: a portion of the flow deviates horizontally and a portion deviates vertically (see Figure I-2).

Buzzi and Tibaldi (1977) discussed a series of steady state analytical experiments of viscous and stratified flow over a topographic feature. The results showed that an anticyclone or "high" forms over the barrier with a cyclone or "low" forming in the lee. This differed from the inviscid case where no such asymmetry was observed. (Note: for the cases discussed, the Coriolis parameter was assumed constant. With f varying with latitude, a lee type trough forms even for inviscid conditions as shown in Figure I-1.) In addition, the intensity of stable stratification of the fluid increased the amplitude of horizontal deflections and limited the vertical response of the flow. The stability introduces a new vertical scale. The more the vertical displacements are resisted by the static stability, the more the flow is forced around the obstacle rather than over it. We hope to introduce the concept of a vertical scale in the development of the analysis scheme in Chapter II.

Buzzi and Tibaldi (1978) showed qualitatively that lee cyclogenesis

in the Alps is a two-stage process. Similar conclusions have been drawn from other studies of cyclogenesis in the Rocky Mountains by Petterssen and Smebye (1971), Johnson et al.(1976), and Phillips (1979). In the first stage, a pure orographically derived system is initiated by processes discussed in the previous paragraph. This disturbance is shallow and has weak circulations. The differences between the Rockies and Alps at this initiation stage are minor. However, in the Alps region air moves either around or over the mountain (depending on the ambient stability), while in the Rockies, owing to the large extent transverse to the flow, the air must move over the mountain. This has interesting effects which will be discussed further on.

The orographic cyclone is one in which vertical circulations are shallow (and frequently downward at the center of the disturbance), inhibiting the development of clouds and precipitation. With the approach of a disturbance aloft and its associated baroclinic zone, a transition occurs where the cyclone changes from the shallow structure described to one that may extend through the entire troposphere. The approaching wave could possibly initiate a cyclone development process independent of the mountain. This would take about four days if baroclinic instability criteria were met (Holton, 1972; Eady, 1949). In the lee of the Alps, however, the same preconditions result in a cyclone that develops within one day or less. Clearly, some accelerating process is taking place in the lee region during the second stage of development. Similar rapid transitions also occur in cyclogenesis associated with the Rockies (Phillips, 1979). The transition stage is one in which the mountain enhances the baroclinic cyclogenic process by modifying the primary zone of baroclinicity and inducing a vertical motion structure

which assists in vorticity production.

To define how the mountains are forcing the intensification of the primary baroclinic zone requires that we look into the frontogenetic process. Frontogenesis theory has been advanced significantly by work done by Hoskins and Bretherton (1972), and Hoskins and West (1979). They find that frontogenesis is a natural outgrowth of baroclinic development when a jet (or an intense zone of thermal contrast) is present at the initial time. Frontal evolution depends on two factors:

1. The frontogenetic rate depends on the ambient baroclinicity.
2. The strength of the front is related to the presence of a jet current and the associated flow deformation, (essentially the way in which the axis of dilatation is oriented with respect to the local thermal gradient).

From La Seur (1974) we can add another factor:

3. Frontogenesis at middle levels is due primarily to the tilting mechanism, where gradients in vertical motion act to reorient the natural vertical temperature stratification.

The important results here indicate that the frontogenetic process is induced by secondary circulations. These are the adjustments needed to keep the atmosphere in some state of balance, e.g., quasi-geostrophic balance. These ageostrophic motions contribute most to the frontogenetic process. Diagnostically this presents some difficulty, simply because unmodified and uncoupled observations and analyses are incapable of providing realistic measurements of motion one order of magnitude less than the horizontal wind. This is especially true of motions in the vertical. For these reasons we must use care in the development of the analysis scheme.

How does frontal zone strength and frontogenesis affect the cyclogenesis problem? For baroclinic development to occur, the amount of thermal contrast in the atmosphere must exist through a significant depth. Strong shallow frontal zones are frequently observed, yet rarely lead to cyclone development. Much evidence exists (albeit most is from numerical experiments and qualitative work) that the Alps enhance the frontogenetic process. The externally forced motions associated with the airflow around the terrain produce secondary circulations which modify the baroclinicity in the local area. The tilting and deformation induced by the mountains are on scales related to the dimensions of the terrain. Intensification of the frontal zone in such a critical position with respect to an already existing circulation would obviously enhance the development potential.

As shown by Johnson (1970) and Wei (1979), it is possible to budget energy in isolated volumes containing cyclones providing that boundary fluxes can be calculated accurately. The processes described above should be reflected in the energetics of the lee cyclone, particularly as the flow modifies the available potential energy (Johnson, 1970) and kinetic energy of the disturbance. The aim here is to establish the energy cycle of the flow with respect to the developing storm. Energy budgeting over mountains has not appeared in the literature and precise quantitative results are difficult to obtain. In any case, it may provide some insight into the effect of the mountains on cyclone development in the Alps region.

To summarize let us state the goals of this research paper.

1. We want to define the structure of the lee cyclone with respect to vertical motion and vorticity, and compare its evolution to the development cycle discussed in earlier works. We expect to distinguish at least two distinct stages in this development.

2. The frontogenetic process associated with the mountain flow is quantified and related to the energy budget. Observations indicate that the frontal zone increases in strength dramatically. We intend to look at the tilting and deformation mechanisms related to the mountain range.
3. Extending the energy budgeting further, we examine quasi-Lagrangian variations of bulk energy quantities with time and attempt to evaluate the transformation of energy from potential to kinetic, and from environmental to perturbation scale. The energy budget will allow us to further explain the character of the evolution of the intensifying cyclone.
4. The basic data fields include a balanced or geostrophic component combined with a weight-dependent unbalanced component, the magnitude of which is dependent on the particular environment under study. Many of the processes which produce frontogenesis and vorticity are related to these unbalanced components. When possible, geostrophic and nongeostrophic effects are distinguished. It is hoped that the objective analysis scheme serves as a valuable research tool for this and other diagnostic studies.

CHAPTER II

THE ANALYSIS SCHEME

Background

The goal of any analysis scheme is the production of representative interpolated data fields from ensembles of discrete observations. We seek to remove non-pertinent features of the data which can originate from a variety of sources. Schemes to automate this process are termed "objective". However, we do not know the structure of the true fields and hence, lack an objective criterion on which to base the selection of the scheme and the various controlling weights which are normally a part of most objective analysis models.

The objective analyst is forced to set criteria subjectively. Should the analysis match the discrete data exactly; or should known laws of physics also play a role in coupling fields of interpolated data? In the literature many approaches have been taken. A historical review by Haltiner (1971) discussed how Panofsky used a least squares method to fit a polynomial to the observations. Cressman introduced a weighting function which allowed the data to be filtered during the analysis process. This scheme still is in wide use. An often used extension of this type of technique is by Barnes (1973), who used exponential weighting in space and time to improve definition in analysis of mesometeorological fields. Doswell (1976) extended this type of analysis to isolate particular modes.

Panofsky also discussed the possibility of coupling related fields dynamically. In a landmark work, Sasaki (1958) used the calculus of variations to do precisely that: combine a set of discrete observations of mass and momentum which match in a least squares sense the observations, and in a dynamical way couple through the pertinent physics. Sasaki's technique has been extended in other papers by Sasaki (1969, 1970), Achtemeier (1975), Wagner (1971), and others.

Even with a variational technique, the analyst is forced to decide subjectively how best to combine the data with physical relationships. How closely the observations are matched, and which physical relationships to use, are fundamental considerations.

In this chapter we present the series of steps necessary to obtain an objective analysis, and demonstrate that the subjectivity can be reduced by the foreknowledge of the meteorological problem being considered, by the limits of data, and by the consideration of scale. If we wish to employ this scheme to diagnose meteorological processes associated with weather systems, it must as a minimum provide representative fields of wind, pressure, geopotential, vertical motion, and moisture, in the region of interest.

Quality of Data

Before we discuss the analysis, it may be helpful to determine the accuracy of the individual observations. Balloon borne sensors have been used for nearly five decades with generally excellent results. The following table extracted from information compiled by Bloom (1980) and Halem *et al.* (1978), illustrated the sensing accuracy of geopotential, temperature, winds, and relative humidity. Since satellite data will be used in this study, it is included.

TABLE II-1

ACCURACY OF BALLOON BORNE (RAOB) AND SATELLITE
BORNE (SATOB) SENSORS

RMS Errors				
RAOB				
Pressure level (accuracy \pm 1.5mb)	Geopotential (gpm)	Temperature ($^{\circ}$ C)	Wind (m/sec)	Relative Humidity (%)
900	20	.2	0.7	10
500	46	.2	2.0	17
200	117	.2	3.0	25
SATOB				
900	75	2.5	-	30
500	575	4.0		(total for column)
200	1363	2.0		

Increased errors in wind measurement at high levels result from a decreasing change in azimuth and elevation angle with time as the balloon moves away from the observing station. Temperature data from RAOBs is quite good, while SATOB sensors show poorer performance. Techniques to combine and assimilate SATOB data with RAOB data are described later.

Analysis Errors

Meteorological analysis schemes contain many sources of error.

Among these are:

1. Measurement error (as tabulated above). These result from instrument problems, location biases, and human errors. These errors are generally random from station to station and are often eliminated during preliminary data checks. Errors which survive produce apparent power at wavelengths near the Nyquist data interval, L_N . Once the data is interpolated to the grid, filtering can reduce it further.

2. Interpolation errors. Interpolation error arises from the redistribution of data from its geographical location to a grid system. Gandin (1963) wrote an extensive work on optimum interpolation in which error is minimized using field structure and correlation functions. Later work by Wahba and Wendelberger (1980) introduces a technique which uses splines and cross validation to eliminate interpolation totally. This method would be ideal since it allows for application of constraints on the fields. However, it is too computationally complex for very large data sets. A method that has been used in a variety of studies (Wagner, 1971; Hylton, 1972; McGinley, 1973; Sasaki et al. 1977; Sasaki and McGinley, 1978, assigns the data directly to a grid point, and then uses splines of varying tension to interpolate the data to grid points between those initialized. The mesh selected is fine enough to provide smooth derivative fields and minimize excessive data station to gridpoint displacements (for our study the displacement RMS is 30 km).

3. Sampling error. Sampling error results from the discrete nature of the data. As shown in Jenkins and Watts (1968), waves of short spacial wavelength when sampled at an interval greater than $L/2$ (L is wavelength),

are aliased into the larger waves. That is, the power at L appears at some longer wavelength. Of course, this is undesirable and little can be done to correct this problem. However, as Stephens (1971) shows, combining two dynamically related data sets increases the resolving power of the model. The direct effect on the elimination of aliasing can be seen by sampling data from a known periodic function and comparing the results before and after filtering and dynamic coupling.

4. Truncation error. Evaluation of derivatives presents another problem. For a wavelength near the Nyquist interval no information regarding the structure can be obtained. Computing a derivative can lead to unacceptable error (here 10% is assumed acceptable) for smaller waves. The table below shows percent error in evaluating first and second centered difference derivatives of a harmonic signal of varying wavelength on a grid of spacing d .

TABLE II-2

PERCENT ERROR IN COMPUTATION OF FIELD DERIVATIVES

<u>Wavelength of Meteorological Signal (in grid space units, d)</u>	<u>First Derivative</u>	<u>Second Derivative</u>
4	46.1	109.3
6	19.3	42.0
8	10.6	22.0
10	6.6	13.8
12	4.6	9.5

The Low Pass Filter

From the previous discussion of errors we can see that much of the undesirable contamination in our data set comes from attempting to "squeeze" too much information from waves at or near the Nyquist wavelength of the discrete data. The first step in our analysis will be to apply a low pass filter. Fritsch (1971) showed that the curve with minimum curvature which connects discrete data points takes the form of a spline. The combination of this idea and variational analysis was presented by Wagner (1971) who showed that use of a "weak" constraint (Sasaki, 1970) on the second derivative of the field, and the minimization of adjusted values at data initialize gridpoints, was essentially the same as forcing a spline fit to the data. The revolutionary aspect of Wagner's scheme was the control given the analyst in manipulating the spectral response of the data through the use of weighting factors.

Sasaki et al. (1977), adapted this technique for use on a sphere. The variational formalism can be written in a latitude (ϕ), longitude (λ), log pressure (π) domain as:

$$F_1 = \iiint_{\lambda\phi\pi} \left\{ \alpha(\theta - \tilde{\theta})^2 + \beta \left(\nabla_3^2 \theta - \frac{\tan \phi}{a^2} \frac{\partial \theta}{\partial \phi} \right)^2 \right\} d\pi d\phi d\lambda \quad (\text{II-1})$$

where θ is the variable to be analyzed, $\tilde{\theta}$ is the observed variable, α is an observational weight (zero at locations where there are no reports), β the weight on the Laplacian of the field, and a is the radius of the earth. The response of the filter can be controlled by adjusting the parameter β . The response function is shown in Figure II-1. Specific details concerning the variational expansion of Equation II-1, and its solution, are given in Appendix 2. The value of β selected corresponds to a response

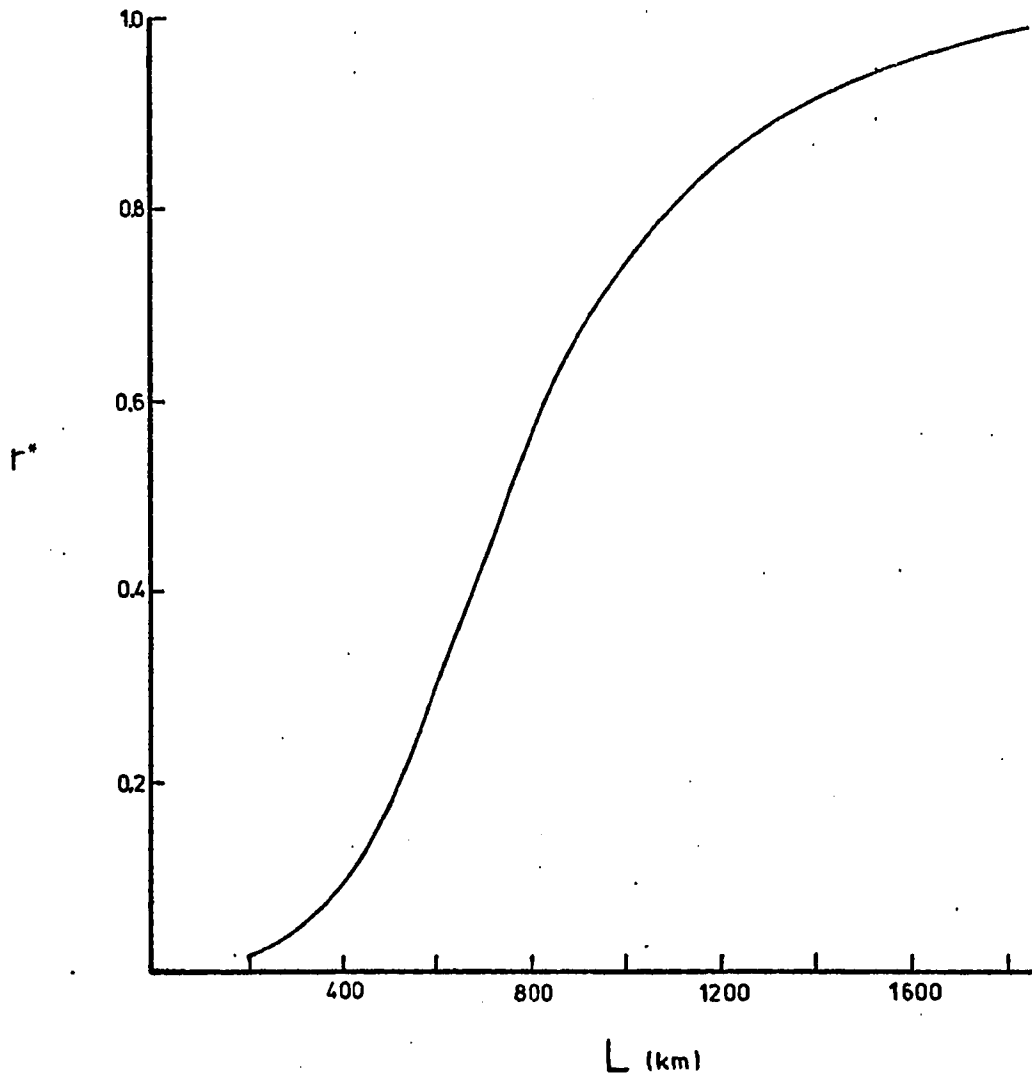


Fig. II-1. Response (r^*) of filter for $\beta/\alpha = 5.96 \times 10^7 \text{ km}^4$

near the Nyquist wavelength for European upper air data. In Europe L_N is 760 km, so we set the filter "cut off" at this wavelength. (Cut off refers to the wavelength at which the response falls to $\sim .5$). In the case studies, RMS temperature adjustments at grid points containing data, ranged from .5 to 1.0°C; for winds, .5 to 1.0 m/sec.

Satellite Data Assimilation

It may be seen from the previous section that since we let the response be as large as .5 for L_N , significant contamination could result. This would be true if data of no higher resolution were available. However, we also include temperatures retrieved from satellite radiance data (for satellites $L_N = 500$ km), (see Appendix 2) to supplement the RAOBs and surface observations ($L_N = 330$ km). These data are assimilated and coupled during the analysis process.

Many techniques have been developed to combine RAOB and SATOB data. Some of these are discussed in Halem et al.(1978). As shown in Table II-1, there is a large amount of error in the retrieved satellite temperatures. Direct insertion of these observations into a set of RAOBs normally results in complete negation of any benefit anticipated through increased data density. Hillger and Vonder Haar (1979) showed that while absolute values of the temperature was poor, the structure of the field given by either the raw radiance or retrieved temperature was good, in fact comparable to the most dense networks of RAOBs. Thus it would seem if the systematic bias error can be removed, SATOBs can make a favorable contribution to the resulting analysis.

The approach taken is to force the solution field to match gradients defined by the satellite field (McGinley, 1979). This process is introduced

during the low pass filtering/interpolation phase. Equation II-1 is modified as:

$$F_2 = \iiint_{\lambda\phi\pi} \{ \tilde{\alpha}_r (\theta - \tilde{\theta}_r)^2 + \tilde{\alpha}_s (\theta - \tilde{\theta}_s)^2 + \beta (\nabla_s^2 \theta)^2 + \gamma_1 (\nabla\theta - \nabla\hat{\theta}_s)^2 + \gamma_2 (\nabla^2\theta - \nabla^2\hat{\theta}_s)^2 \} d\pi d\phi d\lambda \quad (\text{II-2})$$

Here, the Laplacian operators ∇^2 and ∇_s^2 , are defined on a sphere, $\tilde{\theta}_r$ is the observed RAOB temperature, $\tilde{\theta}_s$ is the satellite field interpolated to the grid independently, (in this case using II-1). Terms $\tilde{\alpha}_r$ and $\tilde{\alpha}_s$ are observational weights on RAOBs and SATOBs, respectively. The term with $\tilde{\alpha}_s$ is included for completeness, (normally $\tilde{\alpha}_s$ will be very small). γ_1 is the weight on the first derivative of the interpolated satellite field, γ_2 for the second derivative. Expansion of Equation II-2 by variational methods, development of equations and solution technique is given in Appendix 3. A more complete discussion of this technique and test results is given in Appendix 1.

Dynamic Coupling

Up to this point the major accomplishment of steps in the analysis has been to: 1) assimilate various sources of data, 2) interpolate these data to a grid system, 3) spectrally delineate the gridded fields. The gridded data is now assumed to be "observed" at each grid point, and as such will represent the tilde ($\tilde{}$) terms in the second phase of the analysis, the dynamic coupling phase.

We know from the equations of motion that mass (geopotential, ϕ) and motion (u , eastward motion; v , northward motion) are linked. Ideally the "raw" observations should reflect this coupling. However, data

collection errors, interpolation errors, and unresolvable meteorological phenomena will produce imbalances or residuals when terms in the equation are evaluated. In this section we impose a constraint on the mass and momentum fields which insures complete or partial satisfaction of the geostrophic wind equation and allows for horizontal and vertical coupling of these data.

The frictionless form of the u-momentum equation is given as:

$$\frac{\partial u}{\partial t} + u \frac{\partial u}{\partial x} + v \frac{\partial u}{\partial y} + \omega \frac{\partial u}{\partial p} + \frac{\partial \Phi}{\partial y} - fv = 0 \quad (\text{II-3})$$

where x , y , and t have the usual meaning, ω is the vertical motion ($\frac{dp}{dt}$) in a pressure coordinate, p . In analysis of a sequence of data sets, Bloom (1980) showed that one could impose the time dependent equation as a strong constraint on the fields if a sufficiently short interval in time existed between observations. The task of solving a variational problem of this type is large, since the desired fields are four dimensional. In any case, the results obtained show that the solutions for mass and momentum clearly minimize the residual in the equation of motion, and as such, represent the best dynamically consistent fields for diagnostic work.

Imposition of a strong constraint using the complete equation of motion was considered for this study. However, an alternate course was selected because data availability at 12 hour intervals over Europe is too sparse to effectively employ such a technique, (Bloom, 1980).

Sasaki (1970) discussed the weak constraint. Here we impose a condition such as Equation II-3 or an approximation to II-3, and expect only partial satisfaction in a mean sense over the domain. For problems at synoptic and regional scale such a technique has been shown to be effective,

(Baxter, 1975; Sasaki and McGinley, 1978, and Phillips, 1979).

To develop our method we begin with the equation of motion (II-3). We can elect to scale this equation using typical values in our experimental region (Buzzi and Tibaldi, 1977). The length scale L is appropriate for the largest disturbances produced by the terrain. L is related to the dimensions of the terrain. In the case of the Alps this is about 500 km. Velocity U , typical of wintertime conditions is about 15 m/sec. The time scale T is given by $T=L/U$. Large scale vertical motion can be roughly estimated by evaluating the upslope component, $\Omega = \frac{U(P_{sfc}-P_{min})}{L}$, where P_{min} represents the highest terrain. If we use these values to scale the terms in Equation II-3, we get

$$\frac{U}{f_0 L} \left(\frac{\partial u^*}{\partial t^*} + u^* \frac{\partial u^*}{\partial x^*} + v^* \frac{\partial u^*}{\partial y^*} + \omega^* \frac{\partial u^*}{\partial p^*} \right) - f^* v^* + \frac{\partial \phi^*}{\partial x^*} = 0 \quad (II-4)$$

The starred terms are non-dimensional and of order 1. The ratio $\frac{U}{f_0 L}$ is known as the Rossby number, R_0 . For the Alps, $R_0 \approx .3$. Since $f^* v^*$ is $O(1)$, then the only term to balance it must be $\frac{\partial \phi^*}{\partial x^*}$. Equation II-4 can be written:

$$R_0 \left(\frac{du^*}{dt^*} \right) - f^* v^* + \frac{\partial \phi^*}{\partial x^*} = 0 \quad (II-5)$$

where the first term on the left represents the scale dependent accelerations of the air parcels, which create ageostrophic flow.

One can surmise that only small errors would be introduced if the term on the left of II-5 were ignored. As such, the term represents the residual error if we use the geostrophic wind relationship ($v = \frac{1}{f} \frac{\partial \phi}{\partial x}$) to describe the coupling between mass and momentum. As R_0 becomes very small (large scale terrain) this relationship is a good approximation. For smaller scale phenomena where R_0 may be 1, the entire equation (II-3)

must be used along with introduction of time as an independent variable, as Bloom (1980) did in his analysis of mesoscale data.

With some foreknowledge of the expected residual error in Equation II-5 over a region, we can choose our weighting factors somewhat objectively. If we are proposing to diagnose processes and imbalances related to the dimensions of the terrain, two criteria must be satisfied.

1. The data must resolve the appropriate components of mass and motion.
2. The objective analysis must allow these imbalances to pass through the adjustment process with minimal alteration.

The observed data has been interpolated and filtered; but as mentioned, the RMS departures from the original observations are small, and hence, the essence of the raw field still remains in the tilde (\sim) fields. Another consideration lies in the relative quality of the wind and temperature (geopotential) observations. As shown previously, the measurement quality and spacial density of thermal sensing is superior to that of the winds. We should exploit this by favoring adjustment of winds over temperature (or geopotential), in some systematic way. We demonstrate that by assuming a fixed statistically derived ratio of wind to geopotential data quality, we can reduce the governing parameter to a single weight which controls the amount of RMS error in the geostrophic wind equation over the domain. Further, it will be shown that the selection of this weight can be based on the features of the flow (those induced by terrain), desired for the diagnostic study.

Example of Equation Development and Weighting Factors

The nature of the analysis problem is three dimensional. Details of the actual analysis equation development are given in Appendix 4. We

gain insight into the process by looking at simplified analytical fields.

Consider a problem with one dimension of an f -plane ($f=f_0$). We have "observed" winds (which may have been derived from the previous phase) defined as U ($=\text{const}$) and $\tilde{v}(x)$, and an observed geopotential $\tilde{\phi}(x)$, which are functions of x alone. The function F_3 can now be written,

$$F_3 = \int_0^{x_0} \alpha_w (v - \tilde{v})^2 + \alpha_\phi (\phi - \tilde{\phi})^2 + \alpha_0 \left(f_0 v - \frac{\partial \phi}{\partial x} \right)^2 dx$$

The α -terms are weights on the wind, geopotential, and geostrophic error respectively. These weights are constant over the domain $[0, x_0]$. Applying the variational operator, setting the variation of F_3 equal to zero (for v and Φ which minimize F_3), and integrating by parts gives

$$\delta F_3 = \int_0^{x_0} \left[\underbrace{\left\{ v - \frac{\alpha_w \tilde{v} + f_0 \alpha_0 \frac{\partial \tilde{\phi}}{\partial x}}{\alpha_w + f_0^2 \alpha_0} \right\}}_{\text{Term a}} \delta v + \underbrace{\left\{ \frac{\partial \tilde{\phi}^2}{\partial x^2} - \frac{\alpha_\phi}{\alpha_0} \tilde{\phi} + \frac{\alpha_\phi}{\alpha_0} \tilde{\phi} - f_0 \frac{\partial v}{\partial x} \right\}}_{\text{Term b}} \delta \phi \right] dx$$

$$+ \delta \tilde{\phi} \left(f_0 v - \frac{\partial \tilde{\phi}}{\partial x} \right) \Big|_0^{x_0} = 0 \quad (\text{II-7})$$

The two terms a and b in the integral are the Euler-Lagrange equations which must vanish if the variations δv and $\delta \phi$ are arbitrary over the domain.

The last term defines the boundary condition.

To obtain an equation for geopotential, ϕ , first substitute II-7a into II-7b, we get

$$\phi'' - A\phi = -A\tilde{\phi} + f_0 \tilde{v}' \quad (\text{II-8})$$

where

$$A = \frac{\alpha_\phi}{\alpha_0} + f_0^2 \frac{\alpha_\phi}{\alpha_w}$$

Let the observed fields $(\tilde{\phi}, \tilde{v})$ be defined as

$$\tilde{\phi} = H_0 \sin kx - Ufy$$

$$\tilde{v} = v_0 \cos(kx+p)$$

where p is a shift in phase of the wind relative to the balanced state (see Figure II-2). To find the geopotential adjustment $\phi_a (= \phi - \tilde{\phi})$, we modify Equation II-8,

$$\phi_a = \frac{-B \sin kx}{A + k^2} - \frac{D \cos kx}{A + k^2}$$

Here $B = (H_0 k^2 - f_0 k v_0 \cos p)$ and $D = (-f_0 v_0 k \sin p)$. Using the variation of constants method, a particular solution for ϕ_a is found.

$$\phi_a'' + A\phi_a = B \sin kx - D \cos kx.$$

To simplify interpretation and selection of the weighting factors the full general solution and boundary conditions are ignored.

Since the goal of this phase of the analysis scheme is to control the RMS error of the geostrophic term ($fv - \frac{\partial \phi}{\partial x}$), we find after expanding B

$$(fv - \frac{\partial \phi}{\partial x}) = \frac{\alpha_\phi}{\alpha_0(A+k^2)} \left[f_0 v_0 \cos p \cos kx - f_0 v_0 \sin p \sin kx - H_0 k \cos kx \right].$$

Squaring and averaging over one wavelength yields the mean squared geostrophic error, R_G^2

$$R_G^2 = \frac{1}{L} \int_0^L (fv - \frac{\partial \phi}{\partial x})^2 dx = \frac{(\frac{\alpha_\phi}{\alpha_0})^2}{2(A+k^2)^2} \left[f_0^2 v_0^2 + k^2 H_0^2 - 2f_0 v_0 k H_0 \cos p \right] \quad (II-9)$$

At this point we reduce the three weights to two by defining 2 ratios

$$\gamma \equiv \frac{\alpha_w}{\alpha_\phi} \quad , \quad \Delta \equiv \frac{\alpha_0}{\alpha_\phi} \quad .$$

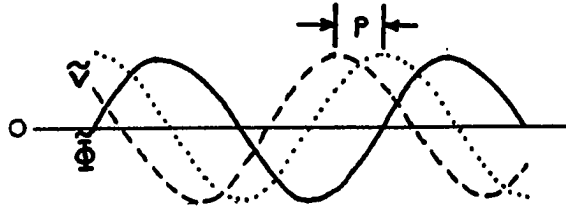


Fig. II-2. Solid line is the input signal representing the "observed" geopotential field. The dashed line is the wind. Dotted line illustrates the wind field for a fully balanced flow. The phase lag p shows the extent to which the flow is unbalanced.

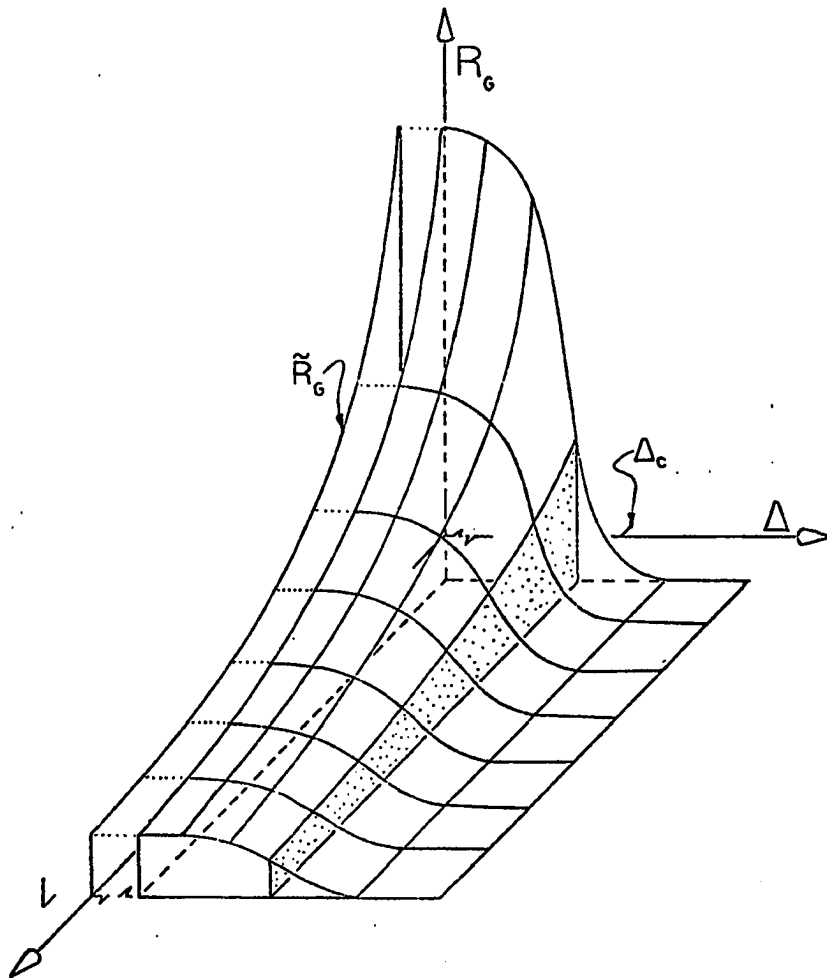


Fig. II-3. Illustration of geostrophic error as a function of wavelength (L) and the dynamic scaling parameter (Δ). Curve \tilde{R}_G is the root mean square error of the unmodified "observed" fields $\tilde{\phi}$ and \tilde{v} . Planar cross-section \tilde{R}_G represents R_G as a function of L for $\Delta = \Delta_c$, ($\log \Delta_c = 10$). This choice is consistent with flow near the Alps.

We call γ the "measurement error parameter," and Δ the "analysis scaling parameter." From Table II-1 we can statistically estimate the relative point observational accuracy of wind and geopotential. γ should represent the ratio of errors of the interpolated fields rather than single observations. However, we assume that this ratio is representative over the whole domain. With statistical data providing a value for γ ($\gamma = 1.21 \times 10^3 \text{ m}^2/\text{sec}^2$), the parameter Δ becomes the single controlling element for the adjustment.

Equation II-9 becomes

$$R_G^2 = (f_0^2 v_0^2 + k^2 H_0^2 - 2f_0 v_0 k H_0 \cos p) / 2 \left[\Delta \left(k^2 + \frac{f_0^2}{\gamma} \right) + 1 \right]^2$$

To clarify the meaning of this relation consider a special case where observational winds are out of phase with observed geopotential, $p = \frac{\pi}{4}$.

Let $v_0 = \frac{kH_0}{f_0}$. Then

$$R_G = \frac{\tilde{R}_G(k)}{\left[\Delta \left(k^2 + \frac{f_0^2}{\gamma} \right) + 1 \right]}$$

Where $\tilde{R}_G(k) = \left[(f_0 v_0 + k_0 H_0 - 2 f_0 v_0 k H_0 \cos p) / 2 \right]^{1/2}$ is the geostrophic error of the observed winds and geopotential. A three-dimensional plot of R_G is shown in Figure II-3. This graph illustrates the characteristics of the RMS error compared to values of Δ and k . Note how R_G decreases as Δ increases, particularly for short waves. There is obvious strong spectral dependence in the adjustment. Winds adjust to heights in accordance with Equation II-7a

$$v = \frac{\gamma}{\gamma + f_0^2 \Delta} \tilde{v} + \frac{f_0^2 \Delta}{\gamma + f_0^2 \Delta} v_g$$

where $v_g = \frac{1}{f_0} \frac{\partial \Phi}{\partial x}$.

The ratio of adjustments can be found by dividing the RMS Φ adjustment by $\tilde{v}_a (v_a = v - \tilde{v})$. We find this ratio is dependent on the wavelength and measurement error parameter,

$$\frac{\bar{\phi}_a^{\text{RMS}}}{v_a^{\text{RMS}}} = \frac{\gamma k}{f_0} .$$

This relation is pleasing from the perspective that for an imbalance at some wave number k , the adjustment will fall upon wind or geopotential in proportion to the square of the measurement accuracy. From a dynamic perspective, once γ is estimated, the adjustment ratio is dependent on wavelength. As Charney shows (Morel, 1973), when the atmosphere is in a state of geostrophic imbalance, it seeks to adjust geopotential to winds at small wavelengths (large k), and winds to geopotential at large wavelengths. The adjustment ratio above operates in the same sense.

For actual data, the major alteration to the discussion above is in the individual profiles of \tilde{R}_G for a given data set. In general, they do not look like the profile shown in Figure II-3. Filtering in stage 2 reduces \tilde{R}_G at large k .

Selection of Parameters

Observations show the Alps produce disturbances in the flow related to their length scale. These disturbances can be resolved by the data. They contain ageostrophic components which can be estimated. We want these unbalanced wind components to pass through the analysis scheme. Large imbalances at small scales which cannot be resolved, must be removed. The mean ageostrophic error for the mountain region can be computed roughly by evaluating the ageostrophic flow component.

The ageostrophic winds, v_a , is $v - \frac{1}{f} \frac{\partial \phi}{\partial x}$. With $\frac{du}{dt} = fv_a$, the scaled equation for Alps flow can be written

$$R_0 \left(\frac{du^*}{dt^*} \right) = R_0 (f^* v_a^*) = f^* v^* - \frac{\partial \phi^*}{\partial x^*}$$

By rescaling we get

$$R_0 f_0 \bar{U} (f^* v_a^*) = f v - \frac{\partial \phi}{\partial x}, \text{ where } \bar{U} \text{ is a representative (mean) velocity.}$$

Thus $v_a \sim R_0 \bar{U}$. This implies that for a mean flow of 15m/sec the Alps should produce ageostrophic flow components of 4 to 5m/sec. We can now adjust v_a to the proper level by finding the appropriate value of Δ .

The following table shows R_g , v_a , and implied R_0 for both the analytical function described by Equation II-9 in the previous section and data from the case studies.

The table shows that the atmosphere is in a better state of balance than the wave shown in Figure II-2. The most appropriate choice of Δ is about 10^{10} m^2 for the range of error desired and the scale of the Alps.

Vertical Motion

In general the wind field derived from F_3 does not satisfy mass continuity. This final phase will allow small adjustments in the vertical and horizontal components of motion to insure that mass continuity is satisfied. The unbalanced or ageostrophic horizontal components of motion contribute directly to vertical motion. The selection of Δ in the previous phase has an impact on the magnitude of vertical motion computed kinematically (by integrating horizontal divergence) from the wind field. For Δ greater than 10^{12} m^2 the mass and momentum are nearly in balance and thus should lead to very small estimates of divergence, and in turn, vertical motion.

The kinematic method for calculation of vertical motion is good in regions where wind data is dense. This is the case over Europe, but not over the Mediterranean. The kinematic fields are thus areally biased. A

TABLE II-3

Error in Geostrophic Equation of Motion						
Analytical Function ($\bar{U}=20$)				Case Studies (12 cases) ($\bar{U}=15$)		
$\frac{\text{Log } \Delta}{(\Delta \text{ in } m^2)}$	$\frac{\text{RMS Error}}{(\times 10^5 m/sec^2)}$	$\frac{V_a}{(m/sec)}$	$\frac{\text{Implied } R_o}{}$	$\frac{\text{RMS Error}}{}$	$\frac{V_a}{}$	$\frac{\text{Implied } R_o}{}$
8	153.1	15.3	.8	126.3	12.6	.8
9	129.4	12.9	.6	107.7	10.8	.7
10	65.2	6.5	.3	20.3	2.0	.2
11	11.2	1.1	.05	9.8	1.0	.06
12	.4	.04	.02	1.8	.2	.01

new approach considers the availability of thermal data from satellites and the consequent improved definition of thermal structure relative to wind structure. The kinematic and dynamic estimates of vertical motion are combined variationally. Here we define the dynamic estimate as that obtained from an appropriate version of the omega equation. Smith and Ping Lin (1978) showed that over data rich regions the kinematic estimate was better than the dynamic estimate, but both correlated well with independently observed clouds and precipitation.

We begin with Haltiner's (1971) version of the steady state balance form of the omega equation,

$$\frac{S}{f^2} \nabla^2 \omega_E + \frac{\partial^2 \omega_E}{\partial p^2} = \frac{1}{f} \frac{\partial}{\partial p} (\hat{\vec{v}} \cdot \nabla (\hat{\zeta} + f)) - \frac{\nabla^2}{f^2} (\hat{\vec{v}} \cdot \nabla \frac{\partial \Phi}{\partial p}) \quad \text{II-10}$$

where $(\hat{\quad})$ defines the adjusted fields from F_3 , $\omega = \frac{dp}{dt}$, ζ is vorticity, \vec{v} vector velocity, T is temperature, and $S (= -\frac{\alpha}{\theta} \frac{\partial \theta}{\partial p})$ is a stability parameter. The dynamic estimate of omega from this equation is the amount of vertical motion necessary to maintain the atmosphere in a quasi-balanced state relative to the thermal advection and differential vorticity advection.

The terrain induces an externally forced component of vertical motion which enters the kinematic estimate through the lower boundary condition. This is the flow forced upward or downward over the terrain surface. (We are considering the surface to be frictionless, and thus eliminating the effects of the Ekman layer). To simplify application of the continuity equation as a strong constraint, we transform the vertical coordinate to the sigma system, where $\sigma = \frac{p}{p_s}$. Here p_s is the pressure on the terrain surface. Such a coordinate is useful in rough terrain since the surface is always $\sigma = 1$.

A technique applied in previous studies (Sasaki, et al. 1977, 1978) and similar to the method applied in an (x, y, z) frame by Dickerson (1978) and Sherman (1978), forces the continuity equation to be satisfied point to point rather than as an integral constraint. This is subject to the minimization of the variance of wind adjustment and vertical motion. In functional form this is

$$F_4 = \iiint_{\lambda \phi \sigma} \left[(u-\hat{u})^2 + (v-\hat{v})^2 + \tau(\dot{\sigma}-\hat{\sigma}_E)^2 + \Omega(p_s \left(\frac{\partial u}{\partial x} + \frac{\partial v}{\partial y} + \frac{\partial \dot{\sigma}}{\partial \sigma} \right) + u \frac{\partial p_s}{\partial x} + v \frac{\partial p_s}{\partial y} + \frac{\partial p_s}{\partial t} - p_s v \frac{\tan \phi}{a}) \right] d\sigma d\phi d\lambda \quad \text{II-11}$$

where $\partial x, \partial y$ are $a \cos \phi \partial \lambda, a \partial \phi$ respectively; a is radius of the earth; $\dot{\sigma}$ is the vertical motion relative to the σ system, $\frac{d\sigma}{dt}$; p_s is surface pressure; u and v are horizontal winds from F_3 interpolated to (x, y, σ) ; $\hat{\sigma}_E$ is ω_E (computed from Equation II-10) transformed to the σ system; Ω is a Lagrange multiplier.

By taking the variation, integrating by parts and assuming the appropriate boundary conditions, four equations are obtained (see Appendix 5)

$$u = \hat{u} + p_s \frac{\partial \Omega}{\partial x}, \quad \text{II-12}$$

$$v = \hat{v} + p_s \frac{\partial \Omega}{\partial y}, \quad \text{II-13}$$

$$\dot{\sigma} = \hat{\sigma}_E + \frac{p_s}{\tau} \frac{\partial \Omega}{\partial \sigma}, \quad \text{II-14}$$

$$p_s \left(\frac{\partial u}{\partial x} + \frac{\partial v}{\partial y} + \frac{\partial \dot{\sigma}}{\partial \sigma} \right) + u \frac{\partial p_s}{\partial x} + v \frac{\partial p_s}{\partial y} + \frac{\partial p_s}{\partial t} - p_s v \frac{\tan \phi}{a} = 0 \quad \text{II-15}$$

Substituting equations II-12 through II-14 into II-15 results in an elliptical equation for Ω which is solved numerically, with boundary conditions which force "vertical" motion (ω) to vanish on the upper, and $\dot{\sigma}$ to vanish at the lower boundaries, and adjustments to be zero on the side boundaries.

The critical parameter in the adjustment is the weight τ . By allowing τ to vary from small to very large, one can see that the vertical motion in II-14 will go from the kinematic estimate to the dynamic estimate. Superimposed on the solution for vertical motion is the externally forced vertical motion due to terrain. By allowing τ to be large the solution vertical motion attempts to match the dynamical estimate. This results in very rapid fall-off of vertical motion with height (assuming the usual case in which the terrain produces motions larger than the dynamics of the flow). Owing to the requirements of mass continuity the adjustment falls on the horizontal wind and flow will be forced around the obstacle rather than over it. We can relate this to vertical static stability of the air and the implied vertical scale of the adjustment process. The depth of atmosphere ultimately effected by the externally forced motion may be termed a scale height. Buzzi and Tibaldi (1977) from analytical experiments deduced a scale height as,

$$H_0 = f L_T (1-R_0^2)^{\frac{1}{2}} \left(\frac{g}{\theta} \frac{\partial \theta}{\partial z}\right)^{-\frac{1}{2}} \sim 3\text{km} \quad \text{II-16}$$

where L_T is the characteristic length of the terrain, R_0 the Rossby number and $\left(\frac{g}{\theta} \frac{\partial \theta}{\partial z}\right)^{\frac{1}{2}}$ the Brunt-Vaisala frequency, a stability parameter. They discussed other experimental works in which modifications of stability led to similarity of solutions when normalized by a parameter like Equation II-16.

In our analysis we wish to duplicate the effect of an implied

vertical scale derived from the terrain scale and static stability. Let weight τ be a function of this vertical scale, and as shown in Appendix 5 (Figure A-5-1), increasing τ forces more flow progressively around the barrier rather than over it. The depth of the mountain induced circulation is significantly reduced as τ increases. Based on the above vertical scale defined by the ambient stability and scale of the Alps, the value of τ selected was 10^{11} m^2 .

Conservation of Potential Vorticity in the Analysis

We have assumed that modifications of the flow induced by the mountains are resolved to some extent by the data. As shown in Chapter IV, the data does a passable job in placing the anticyclonic vorticity over the mountain, and the troughs or cyclonic vorticity in the lee. However, in the Pyrenees, owing to the lack of data over Spain, the anticyclone and lee cyclone are not well defined. To correct this, a simplified potential vorticity constraint was developed and is discussed in Appendix 6. This technique was not included in the analysis of the case study data. As is shown in the aforementioned appendix, this does not have too serious an impact on the results. However, for future studies, the potential vorticity constraint will be included during the geostrophic adjustment phase, F_3 .

Summary of Data Analysis

Our goal has been to obtain three dimensional fields of atmospheric conditions over mountainous terrain, detailed enough to resolve the processes of lee cyclone development. This chapter can be summarized by reviewing the three phases of the analysis and weighting terms which play a role in

the definition of these fields. Figure II-4 schematically describes the data analysis.

1. Interpolation and filtering. Insuring that the data source can resolve features under study, weight β is selected to spectrally define three dimensional fields derived from raw RAOB's and SATOB's. The fields that result are assumed to be "observed" for the next phase.

2. Geostrophic Adjustment. Once a parameter of relative data accuracy, γ , is defined from statistics based on wind and geopotential observations (Table II-1), the problem reduces to defining how much mean error remains in the geostrophic wind relationship over the domain. We know that this error is related to the scale of meteorological phenomena through the Rossby number. Since we want to retain or pass the ageostrophic flow components induced by the terrain, we roughly estimate the amount of geostrophic error in waves of this scale and use this to define weight Δ .

3. Vertical Motion and Vertical Scaling. The ageostrophic flow remaining from phase 2 can allow an estimate of kinematic vertical motion to be computed. However, the horizontal winds do not satisfy mass continuity, particularly when terrain induced vertical motion is taken into account. A second estimate of vertical motion may be derived from the omega equation. These two estimates are combined variationally and linked through weight τ . This parameter also subjectively assigns a vertical scale to the adjustment process. This allows for a logical partitioning of flow into components over and around the terrain. (Note: The magnitudes of adjustments in this phase are about one order of magnitude less than the wind adjustments in phase 2.)

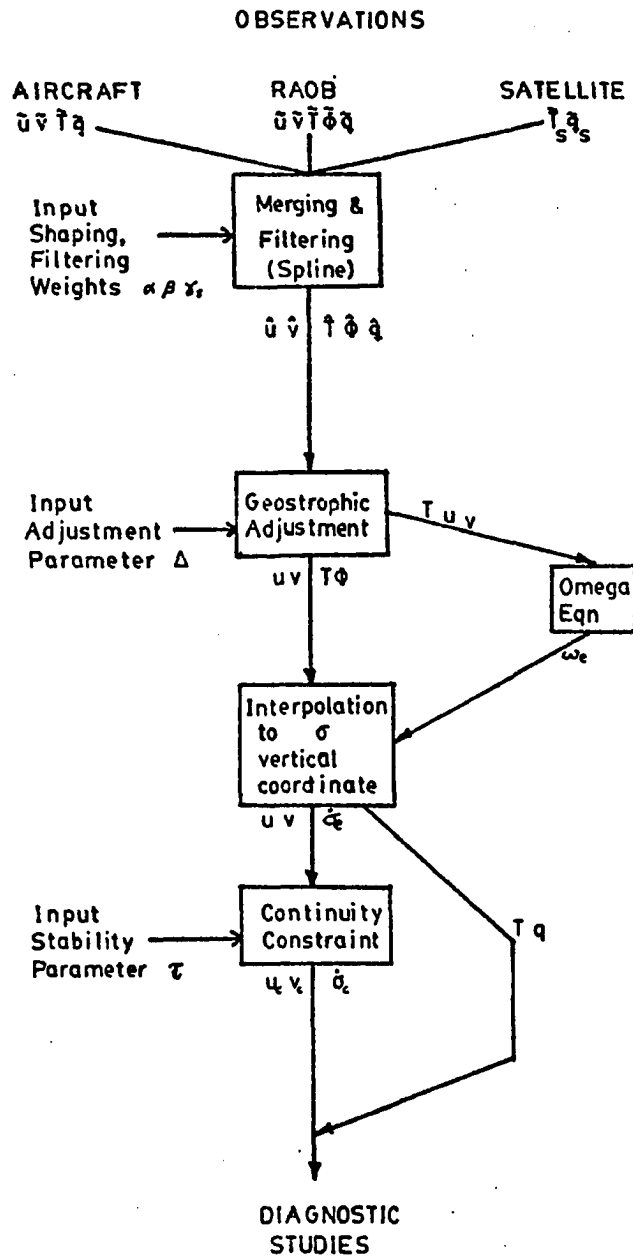


Fig. II-4. Schematic diagram showing flow of data through analysis scheme.

KEY: u, v - horz. winds	$\hat{\sigma}$ - vert. motion in sigma coor.
T - temperature	(\sim) - raw data at observing site.
ϕ - geopotential	(\wedge) - splined smoothed data at grid points.
q - mixing ratio	$(\)_e$ - equation derived est. (omega eqn.)
ω - vertical motion in p coor.	
$(\)_c$ - fields satisfying mass continuity.	

CHAPTER III

FRONTOGENESIS, ENERGETICS, AND VORTICITY

Frontal Zones

The density of data in the region of study does not resolve a true front which has a transverse scale of about 100 km. What can be resolved are zones of baroclinicity where isotherms become strongly packed and influence the development of atmospheric cyclones. In this chapter we explore the relationship of frontogenesis and observed strengthening of these zones, and the role played by terrain in this process and in energetics of the flow. The terminology, frontal zone, is used interchangeably with baroclinic zone.

The Frontogenesis Equation

Within the literature frontogenesis is generally refers to any process which strengthens the horizontal gradient of temperature within an air parcel. Petterssen (1956) defines frontogenesis as

$$\mathcal{F} = \frac{d|\nabla\theta|}{dt} .$$

Expanding in an (x,y,p) frame

$$\begin{aligned} \mathcal{F} &= \frac{1}{2|\nabla\theta|} \frac{d(\nabla\theta \cdot \nabla\theta)}{dt} \\ &= \frac{\nabla\theta}{|\nabla\theta|} \cdot \left[\nabla \frac{d\theta}{dt} - \left(\frac{\partial\theta}{\partial x} \nabla u + \frac{\partial\theta}{\partial y} \nabla v + \frac{\partial\theta}{\partial p} \nabla \omega \right) \right] \end{aligned}$$

where θ is potential temperature; u , v , and w are the components of motion. This form of the frontogenesis equation was used by Miller (1948). By expanding the parcel derivatives further we obtain

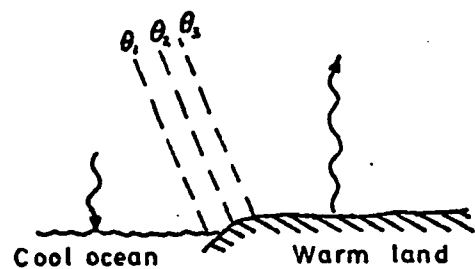
$$\mathcal{F} = \frac{1}{|\nabla\theta|} \left[\underbrace{\nabla\theta \cdot \nabla \frac{d\theta}{dt}}_{\text{diabatic}} - \underbrace{\frac{(|\nabla\theta|^2 \delta)}{2}}_{\text{divergence}} + \underbrace{\frac{(\theta_x^2 - \theta_y^2) S}{2}}_{\text{stretching deformation}} + \underbrace{\theta_x \theta_y R}_{\text{shearing deformation}} + \underbrace{\theta_p (\theta_x \omega_x + \theta_y \omega_y)}_{\text{tilting}} \right] \quad \text{III-1}$$

where subscripts x, y, p refer to partial derivatives; δ is horizontal divergence; S and R are the stretching and shearing deformation, respectively ($S = u_x - v_y$; $R = u_y + v_x$).

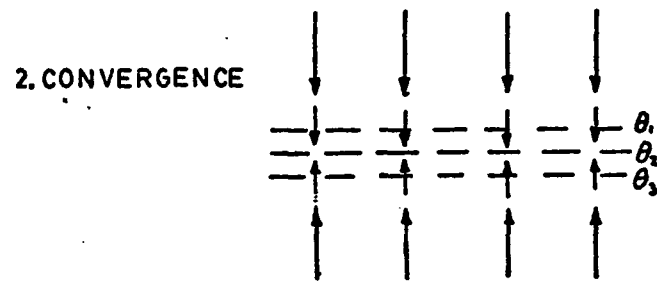
In this form we can evaluate the important components of frontogenesis from terms representing easily calculable quantities related to the flow field. Figure III-1 illustrates schematically the components of frontogenesis. The diabatic term includes processes of latent heat release, convection, or radiation which serve to increase the local horizontal gradient of temperature. The divergence term increases thermal gradients by converging air with different thermal properties. Deformation, can rapidly increase thermal gradients typically near the ground. As Kessinger and Bluestein (1979) discuss, the increase of the thermal gradient by the deformation mechanism may eventually produce secondary direct circulations, which will then induce frontogenesis from the divergence process as well.

As shown by La Suer (1974) the tilting term plays the most important role in middle and upper levels. Gradients in vertical motion rapidly increase frontal zone strength particularly where atmospheric stability is large. In the absence of horizontal thermal gradients, the tilting and diabatic terms are the only mechanisms which can initiate a front. This has important consequences where vertical motion is forced externally by irregular terrain.

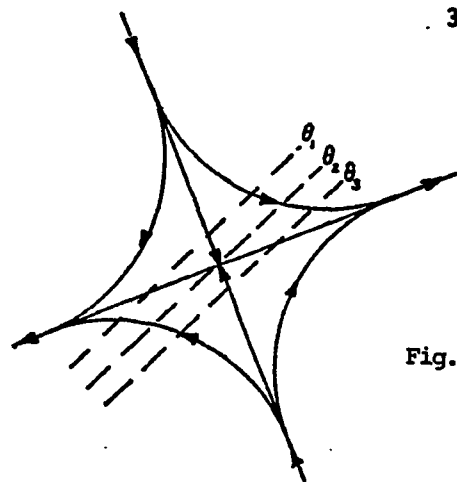
$$F = \frac{1}{|\nabla\theta|} \left[\underbrace{\nabla\theta \cdot \nabla \frac{d\theta}{dt}}_1 - \underbrace{(|\nabla\theta|^2 \frac{\delta}{2} + \frac{S}{2}(\theta_x^2 - \theta_y^2))}_{2.} + \underbrace{R(\theta_x \theta_y)}_3 + \underbrace{\theta_p(\theta_x \omega_x + \theta_y \omega_y)}_4 \right]$$



1. DIABATIC



2. CONVERGENCE



3. DEFORMATION

4. TILTING

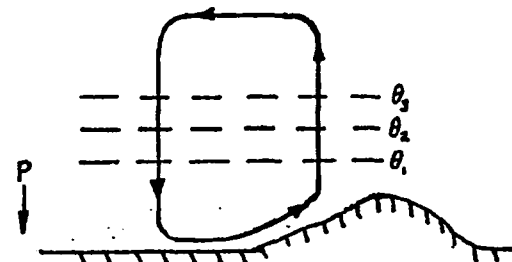


Fig. III-1. Frontogenetic components.

Frontal Strength and Available Potential Energy

The energy of the atmosphere takes a variety of forms. A volume of air with rigid side boundaries and extending through the depth of the atmosphere contains kinetic (KE), potential (PE), and internal energy (IE). These are defined for a unit area as

$$KE = \int_0^{\infty} \frac{\rho}{2} (u^2 + v^2) dz, \quad PE = \int_0^{\infty} \rho \Phi dz, \quad IE = \int_0^{\infty} \rho c_v T dz$$

where Φ is the geopotential, c_v the specific heat of air at constant volume, and T is temperature.

In the volume the total of these quantities must be constant for adiabatic, hydrostatic, and frictionless processes. Using Holton's (1972) simple example (Figure III-2), assume that two juxtaposed air masses of different potential temperature, θ_1 and θ_2 , ($\theta_2 > \theta_1$) are contained in such a volume, and separated by a partition. If the air is initially at rest, the total energy, TE is

$$TE = (PE + IE)_1 + (PE + IE)_2.$$

Since we know that PE and IE are related by a constant ($IE = \frac{c_v}{R} PE = \frac{5}{2} PE$) then $TE = \frac{7}{2}(PE_1 + PE_2)$. When the partition is removed the air adjusts in response to pressure forces and kinetic energy is generated. The total energy must be conserved so the KE produced must be

$$KE = \frac{7}{2} (PE_1 + PE_2) - PE_r = APE .$$

PE_r , the reference potential energy is the minimum possible potential energy assuming an adiabatic redistribution of mass, so that θ_2 is everywhere above θ_1 . The term APE is called the available potential energy (hereafter called

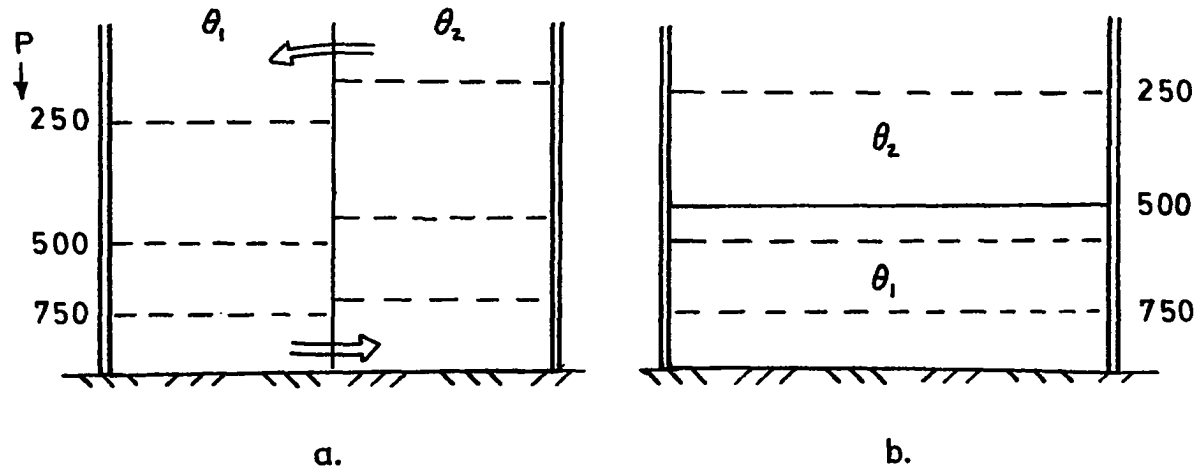


Fig. III-2. Conversion of potential energy into kinetic energy, for $\theta_2 > \theta_1$

- a. Available Potential Energy at maximum; strong pressure accelerations; Kinetic energy is zero.
- b. All APE converted to KE; air is in motion.

APE), since it allows us to estimate the amount of energy in the volume able to generate motion (or storms). In a very crude way the partition represents a baroclinic zone, and its removal represents the development of a weather system. Later we will show that the amount of KE derived from this process is a function of the temperature contrast across a "front". The means by which parcels 1 and 2 obtained their differing character and positioning can be related to the frontogenesis process, Gutman (1969).

Using more sophisticated techniques of Johnson (1970), Wei (1979), and Haltiner (1971), we will calculate APE and KE of volume systems and relate these to the terrain induced frontogenesis. The final illustration in Figure III-2 showed the "minimum" total potential energy condition; that is, hydrostatically stratified with no horizontal gradients of θ . Within any selected volume in the real atmosphere a similar energy state can be defined.

We can derive Johnson's (1970) expression for available potential energy from the relation $APE = TPE - TPE_r$, where TPE is the total potential energy. We know that for a hydrostatic atmosphere

$$\begin{aligned} PE + IE &= \int_0^{\infty} \rho \Phi dz + \int_0^{\infty} \rho c_v T dz, \\ &= \int_0^{\infty} \rho g z dz + \int_0^{\infty} \rho c_v T dz, \\ &= \int_0^{\infty} p dz + \int_0^{\infty} \rho c_v T dz. \end{aligned}$$

Using the equation of state,

$$\begin{aligned} &= \int_0^{\infty} \rho (c_v + R) T dz, \\ &= \frac{1}{g} \int_0^{p_s} c_p T dp. \end{aligned}$$

where the total potential energy is (IE + PE). Thus, for a unit cross section of area A,

$$\text{TPE} = \frac{c_p}{gA} \int_0^A \int_0^{p_s} T \, dp \, dA ,$$

and

$$\text{TPE}_r = \frac{c_p}{gA} \int_A \int_0^{p_s} T_r \, dp \, dA .$$

From Poisson's equation, $T = \Theta \left(\frac{p}{1000} \right)^K$ and $T_r = \Theta \left(\frac{p_r}{1000} \right)^K$, we get

$$\begin{aligned} \text{APE} = \text{TPE} - \text{TPE}_r &= \frac{c_p}{gA} \int_A \int_0^{p_s} \left[\Theta \left(\frac{p}{1000} \right)^K - \left(\frac{p_r}{1000} \right)^K \right] dp \, dA \\ &= \frac{c_p}{gA} \int_A \int_0^{p_s} \left[1 - \left(\frac{p_r}{p} \right)^K \right] T \, dp \, dA = \frac{c_p}{gA} \int_0^{p_s} \int_A \epsilon \, T \, dp \, dA \end{aligned} \quad \text{III-2}$$

This expression has been used by Johnson (1970), Edmon (1970) and Wei (1979) to compute APE. The term ϵ is the efficiency factor. This has the definition $\epsilon = 1 - \left(\frac{p_r}{p} \right)^K$ where p is the pressure and subscript r refers to the reference position of an isentropic surface. The term "efficiency" refers to the effect of diabatic heating if applied at a particular location in the volume. If ϵ is positive then the diabatic contribution will increase the APE, and vice versa. The reference pressure requires a further definition

$$p_r(\Theta) = \frac{1}{A} \int_0^A p(x,y,\Theta) \, dA$$

p_r is the areally averaged pressure on a Θ surface. It represents the hypothetical equilibrium level a given Θ surface would reach if redistributed adiabatically and hydrostatically within the volume. Using Van Mieghem's formulation, Wei (1979) shows that this state represents at least a regional minimum in the total potential energy.

The time rate of change for APE (Equation III-2) is derived by Edmon (1978). The difficulties in applying a physical interpretation to the various terms render this approach somewhat futile from a diagnostic standpoint. The method we use to describe the changes in energy will be discussed further on.

To explore the link between APE and frontal strength, F , consider a simple case where potential temperature in a volume is defined as

$$\theta(x,p) = Fx + S(p-p_0) + \theta_0$$

with $|\nabla_x \theta| = F$; $\theta(0,p_0) = \theta_0$, S is a mean stability parameter, $\frac{\partial \theta}{\partial p}$.

We want p_r and ϵ so

$$p(x,\theta) = \frac{-F}{S} x + \frac{(\theta - \theta_0)}{S} + p_0,$$

$$p_r(\theta) = \frac{1}{L} \int_{-L/2}^{L/2} p(x,\theta) dx,$$

$$= \frac{(\theta - \theta_0)}{S} + p_0,$$

$$p_r(x,p) = \frac{F}{S} x + p,$$

and,

$$\epsilon = 1 - \left(\frac{Fx}{Sp} + 1 \right)^{\kappa}.$$

One can see immediately that the reference pressure is a function of F . If $F = 0$, $p_r = p$ and $\epsilon = 0$. Thus no APE exists in a region without frontal strength. We can use Equation III-2, and formulas for ϵ , and $T(\theta)$ to find

$$APE = \frac{c_p}{Lg} \int_L \int_0^{p_0} \left(1 - \left(\frac{Fx}{Sp} + 1 \right)^{\kappa} \right) \left(\frac{p}{p_0} \right)^{\kappa} (Fx + S(p-p_0) + \theta_0) dp dL$$

This integral is evaluated and the plot illustrated in Figure III-3, which shows APE in a volume versus F . APE increases rapidly for the range of commonly observed frontal zone intensities and standard stability.

Partitioning of Energy Quantities

As discussed, the release of APE allows the development of kinetic energy which moves the system towards the minimum potential energy state.

This motion is in the form of developing disturbances or cyclones. For the open type volumes being considered in our case studies, the generally large magnitude of energy flux through the sides of the volume make it difficult to obtain an explicit relation between decreases in APE and increases in KE (Edmon, 1978; Wei, 1979). For completeness we look at the continuity of kinetic energy and computations describing the transition of the various energy components, even though we may only obtain qualitative relationships.

Haltiner (1971) and Holton (1972) show methods to evaluate APE in a simpler, more approximate way than the Johnson method. While these techniques are more appropriate for evaluation of global energy budgets in a closed framework, they can be applied to open systems if the volume extends over one wavelength of interest, and boundary effects can be eliminated or evaluated. The energy components are divided into mean and perturbation quantities. The volume mean describes the ambient or background conditions, while the perturbations pertain to the cyclone system. We have

$$\begin{aligned}\overline{KE} &= \frac{1}{2gA} \int_A \int_p (\overline{u}^2 + \overline{v}^2) dp dA \\ KE' &= \frac{1}{2gA} \int_A \int_p \{(u-\overline{u})^2 + (v-\overline{v})^2\} dp dA \\ \overline{APE} &= \frac{1}{2gA} \int_A \int_p \frac{(\overline{\alpha} - \alpha_0)^2}{\sigma} dp dA \\ APE' &= \frac{1}{2gA} \int_A \int_p \frac{\alpha'^2}{\sigma} dp dA\end{aligned}$$

where $\overline{\alpha}$ is the specific volume, α_0 the reference specific volume and $\alpha' = \alpha - \overline{\alpha}$. σ is the stability parameter. With the inclusion of frictional effects, F_0 , and diabatic source-sink term, S we must have, for a closed system

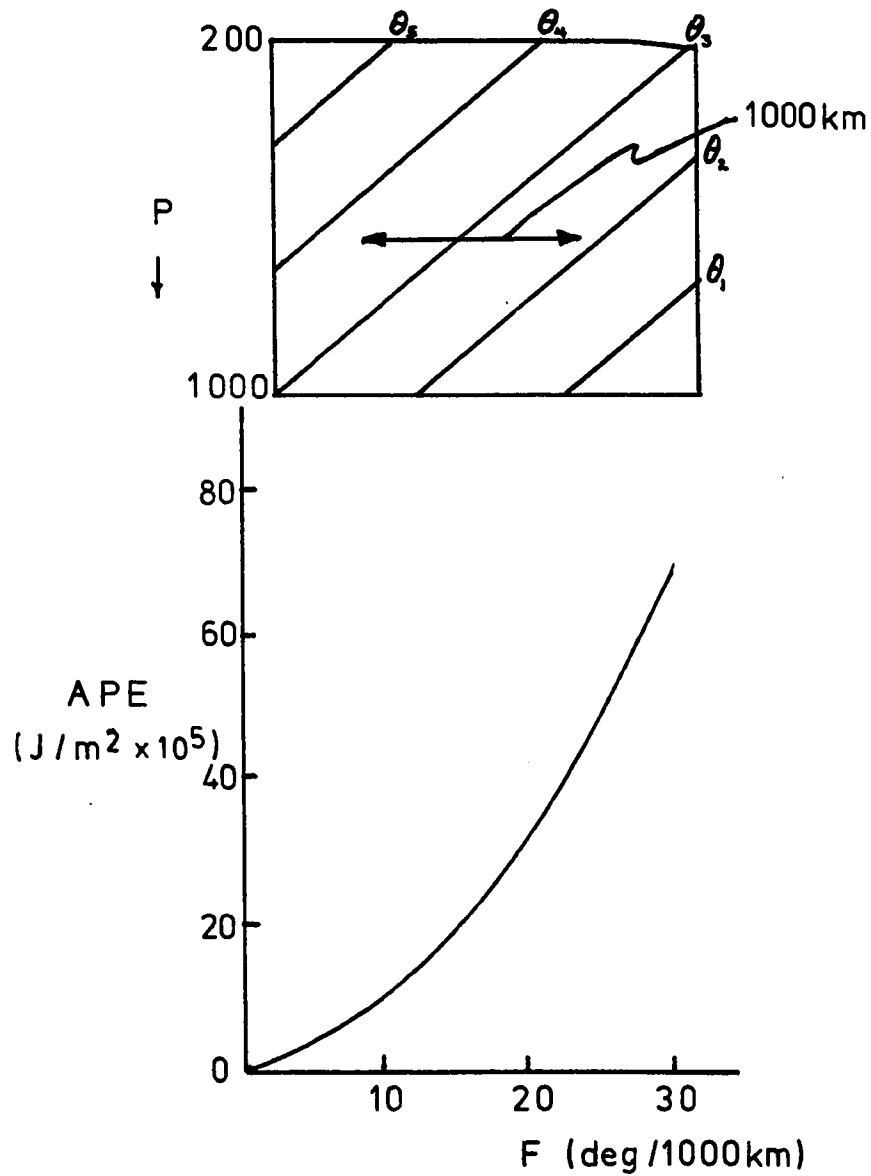


Fig. III-3. Available potential energy versus mean frontal strength in a volume element. Inset shows potential temperature distribution in volume cross-section. S is $.05^\circ \text{K}/\text{mb}$, a representative lapse rate for the troposphere over Europe.

To describe the transformation of these quantities, other integral relations are adapted for use in an open volume. The changes in a volume for which boundary fluxes vanish are

$$\frac{D\overline{KE}}{Dt} = [\overline{KE'} \rightarrow \overline{KE}] + [\overline{APE} \rightarrow \overline{KE}] - [\overline{KE} \rightarrow \overline{F_0}]$$

$$\frac{D\overline{KE'}}{Dt} = [\overline{KE} \rightarrow \overline{KE'}] + [\overline{APE'} \rightarrow \overline{KE'}] - [\overline{KE'} \rightarrow \overline{F_0'}]$$

$$\frac{D\overline{APE}}{Dt} = [\overline{APE'} \rightarrow \overline{APE}] + [\overline{KE} \rightarrow \overline{APE}] + [S \rightarrow \overline{APE}]$$

$$\frac{D\overline{APE'}}{Dt} = [\overline{APE} \rightarrow \overline{APE'}] + [\overline{KE'} \rightarrow \overline{APE'}] + [S \rightarrow \overline{APE'}]$$

where (\rightarrow) refers to the transition process; and $\frac{D}{Dt}$ are the volume changes. The six transition processes can be evaluated for a quasi-geostrophic system integrated over one wave length in a volume moving in a quasi-Lagrangian sense. From Holton (1972) and Appendix 7:

$$1. \quad [\overline{KE'} \rightarrow \overline{KE}] \approx -\frac{1}{g} \int_A \int_0^{p_0} \frac{\overline{\phi}}{\overline{f_0}} \nabla \cdot (\vec{V}' \zeta' g) dp dA$$

$$2. \quad [\overline{APE} \rightarrow \overline{KE}] \approx \frac{1}{g} \int_A \int_0^{p_0} \overline{\alpha} \overline{\omega} dp dA$$

$$3. \quad [\overline{APE'} \rightarrow \overline{KE'}] \approx -\frac{1}{g} \int_A \int_0^{p_0} \overline{\alpha'} \overline{\omega'} dp dA$$

$$4. \quad [\overline{APE} \rightarrow \overline{APE'}] \approx -\frac{1}{g} \int_A \int_0^{p_0} \frac{1}{\sigma} \frac{R^2}{p^2} \overline{\nabla T} \cdot (\vec{V}' T') dp dA$$

$$5. \quad \overline{KE} \rightarrow \overline{F_0} = 6\rho c^{3/2} \overline{V_s}^3$$

$$6. \quad \overline{KE'} \rightarrow \overline{F_0'} = 6\rho c^{3/2} \overline{V_s'}^3$$

III-3

where ζ_g is the geostrophic vorticity, and other symbols have been specified. The last two terms are parameterizations of frictional effects as used by Petterssen and Sembye (1971). V_s is the velocity at the ground; ρ is density; and c is the eddy viscosity which ranges from .0010 to .0045 (mks) from flat terrain to mountains. By evaluating these quantities we may gain some insight into the energy transfer processes within the volume, and can use these instantaneous energy transitions to explain the observed changes in the bulk quantities. However, the formulated conversions and transfers are approximate and rule out smaller scale processes (i.e. inertia-gravity wave proposed by Buzzi and Tibaldi, 1978). Also, the assumption about fluxes vanishing on the boundaries of quasi-Lagrangian volume can introduce errors. The important processes related to radiation, latent heat and dissipation in subgrid systems are not explicitly evaluated or parameterized. (They can, however, be defined through residuals). In any case, we can see if the energetics of lee cyclogenesis are partially explained by quasi-geostrophic formulation. See Appendix 7 for further comments.

The motivations for including energy in this study of lee cyclones are twofold. One is to provide a link between the obvious frontogenetic features of flow over and around the Alps and the impact on the energy available for cyclone development. The second reason is to provide a basis of comparison to other works in which an energy cycle was derived (Oort, 1964; Dutton and Johnson, 1967; and Wei, 1979). The Oort study is illustrated in Figure III-4 for a hemispherical region. The mean quantities of each energy type and the transition rates are given as shown.

The energy transfers for a classical developing cyclone are well documented. Beginning with a background thermal gradient and a mean flow, a perturbation will grow if it has the proper scale for the given amount of

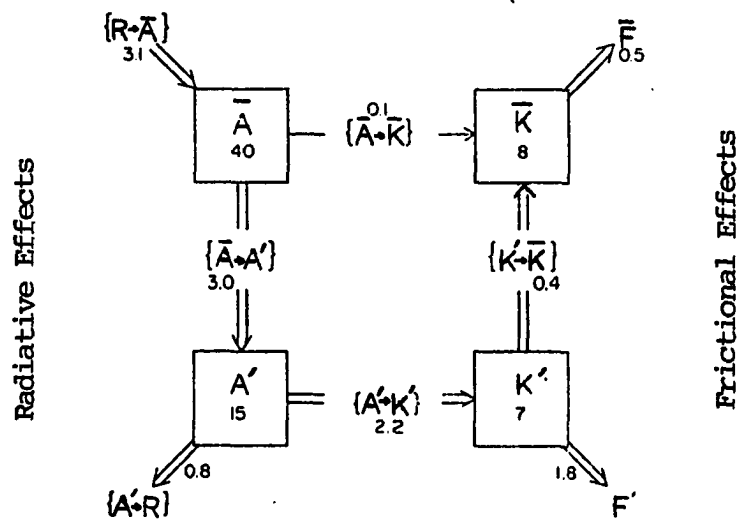


Fig. III-4. Energy cycle for the Northern Hemisphere. Bulk energy quantities are given in $\text{Joules/m}^2 \times 10^5$. Energy transformation figure are in Watts/m^2 . Symbols used are explained in the text or are labeled above. After Oort (1964).

baroclinicity. Once advection processes begin, the local thermal gradient intensifies in the vicinity of the cyclone. This is the process that generates the perturbation APE. In the next stage the rapidly intensifying circulation increases the thermal advection and hence the vertical circulations which convert APE' to KE'. Low level convergence increases the strength of the surface circulation. Friction now plays an important role in dissipating KE' and converting KE' to \overline{KE} through Ekman induced "spin down" processes. (vorticity flux divergence). The main flow of energy in this classical quasi-geostrophic case is from \overline{APE} to APE', to KE', to \overline{KE} and F_0 . The structure of the lee cyclogenesis energy cycle is shown in the next chapter.

Vorticity

The development of a lee cyclone can be traced through the changes in the relative vorticity. The vertical component of relative vorticity is

$$\zeta = \frac{\partial v}{\partial x} - \frac{\partial u}{\partial y}$$

The vorticity equation for frictionless flow is

$$\frac{\partial \zeta}{\partial t} + \underbrace{\vec{V} \cdot \nabla \zeta}_{\text{horizontal advection}} + \underbrace{\omega \frac{\partial \zeta}{\partial p}}_{\text{vertical advection}} + \underbrace{(\zeta + f) \nabla \cdot \vec{V}}_{\text{convergence}} + \underbrace{\vec{k} \cdot \nabla \omega \times \frac{\partial \vec{V}}{\partial p}}_{\text{tilting}} = 0$$

From the perspectives of our study, we would like to evaluate the terms in the vorticity equation based on the derived flow structure. With pressure as the vertical coordinate the effects of intensification of the frontal zone in the vicinity of the developing cyclone are implicit within the convergence term. From a quasi-geostrophic view, thermal and differential

vorticity advection will lead to upward (or downward) motion, and through mass continuity to strengthening (or weakening) of the cyclone at low levels through convergence. The effects here also appear through the tilting term, although at a smaller magnitude. The upward/downward motion couplet interacts with vertical windshear (a function of frontal strength) and tilts associated horizontal vorticity into the vertical.

Flow over a mountain also produces couplets of vertical motion as described above. Owing to the strength of the vertical motion, and the scale of the vertical circulation, this term may play a much larger role than for a case with smooth terrain. Another effect occurs as an air column moves downslope (as shown in Chapter 1). Stretching produces horizontal convergence which increases the relative vorticity through the convergence term.

As discussed by Petterssen and Smebye (1971), superposition of dynamic and externally derived vertical motion processes can produce rapid cyclone development. These cyclones have a structure different from the classical cyclone in that the circulation axis is nearly vertical. Development is most intense at middle levels and occurs very rapidly through the column (~1 Day). Phillips (1979) showed a cyclone in the lee of the Rockies which had a structure and evolution similar to the Petterssen model. The question of the role played by the Alps in cyclone development is explored in the next chapter.

CHAPTER IV

CASE STUDIES AND RESULTS

Using the analyzed fields we will show how the mountains influence the modification of the frontal zone and consequent cyclone development.

Synoptic Situation

The cases selected are taken from data provided by the Data Set Test program supervised by the National Aeronautics and Space Administration (Halem, et al. 1978). These data consist of rawinsonde, satellite radiance, surface, ship and aircraft reports. The data have been subjected to checking both before dissemination and within the present analysis scheme. Figure IV-1 shows the region of study, terrain, and the data available for a representative time. This data was collected at 00 and 12 GMT, which for the central part of our experimental region is about local midnight and noon, respectively. The Alps and Pyrenees are represented as shown.

The synoptic situation during 9 to 16 February 1976 had two periods of lee cyclone development. The first (hereafter referred to as LCD I) occurred from the 11th to the 12th, while the second (LCD II) occurred from the 13th to the 15th. In the first case the cyclone develops rapidly and dissipates similarly. In the second case the cyclone persists for three days.

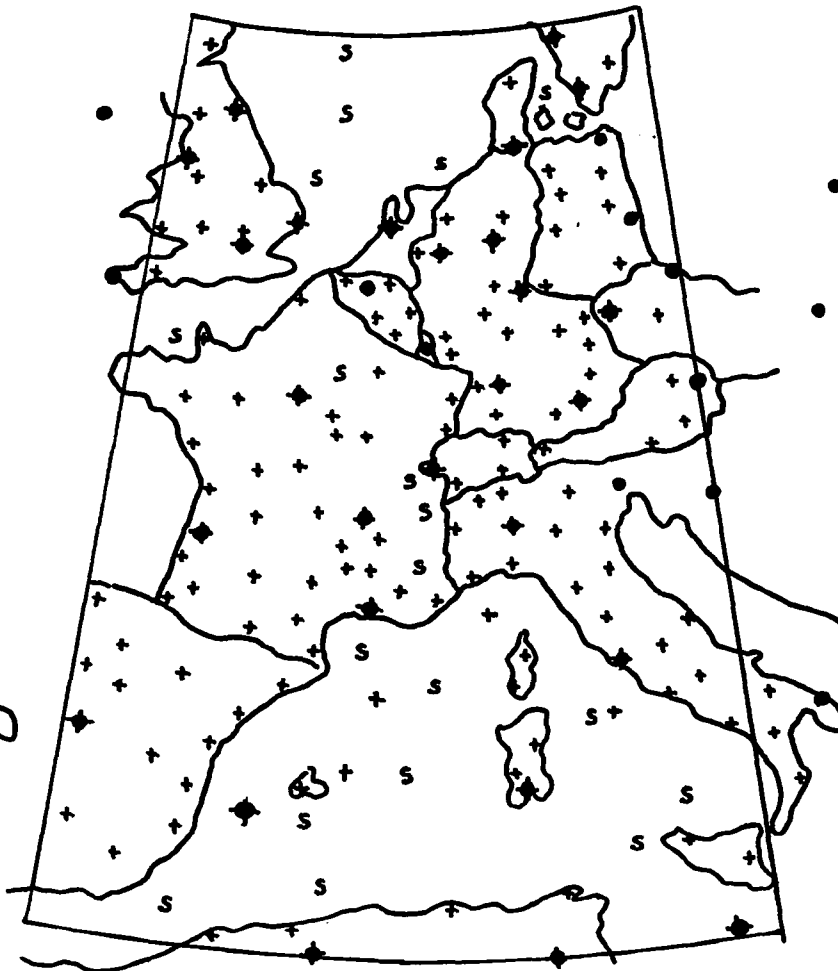
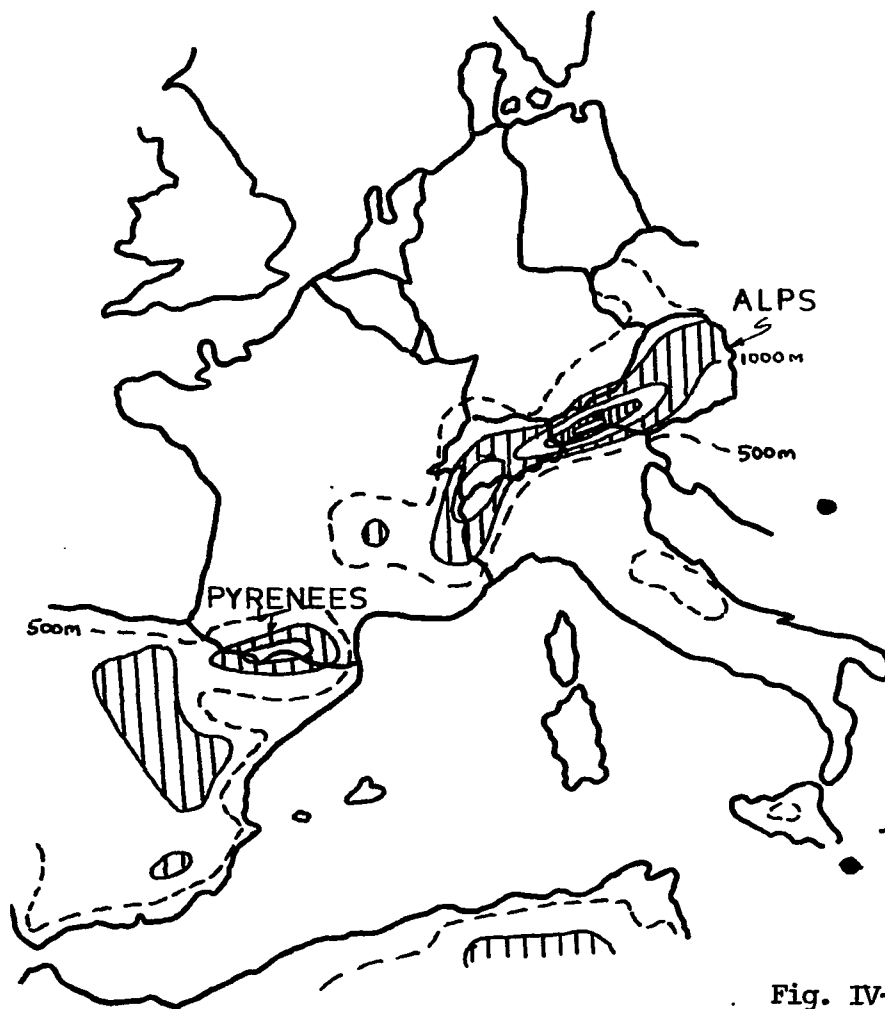


Fig. IV-1.

a. European terrain (contour interval 500 m).









b. Region of analysis (working grid), with RAOB (●), satellite (s), and surface observations (+), indicated.

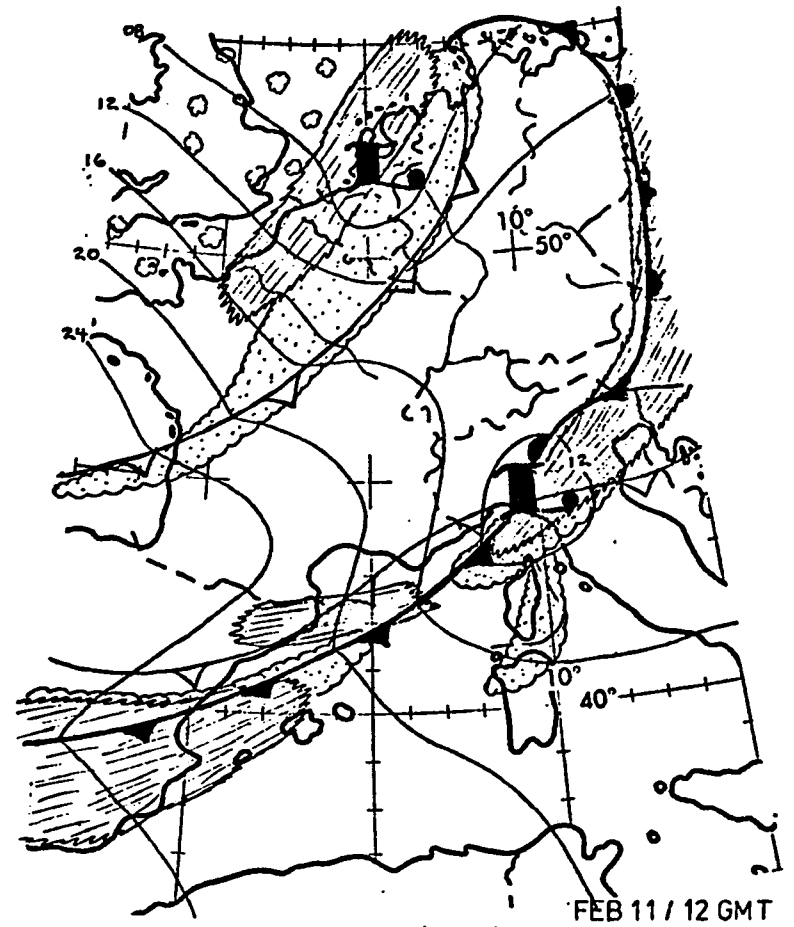
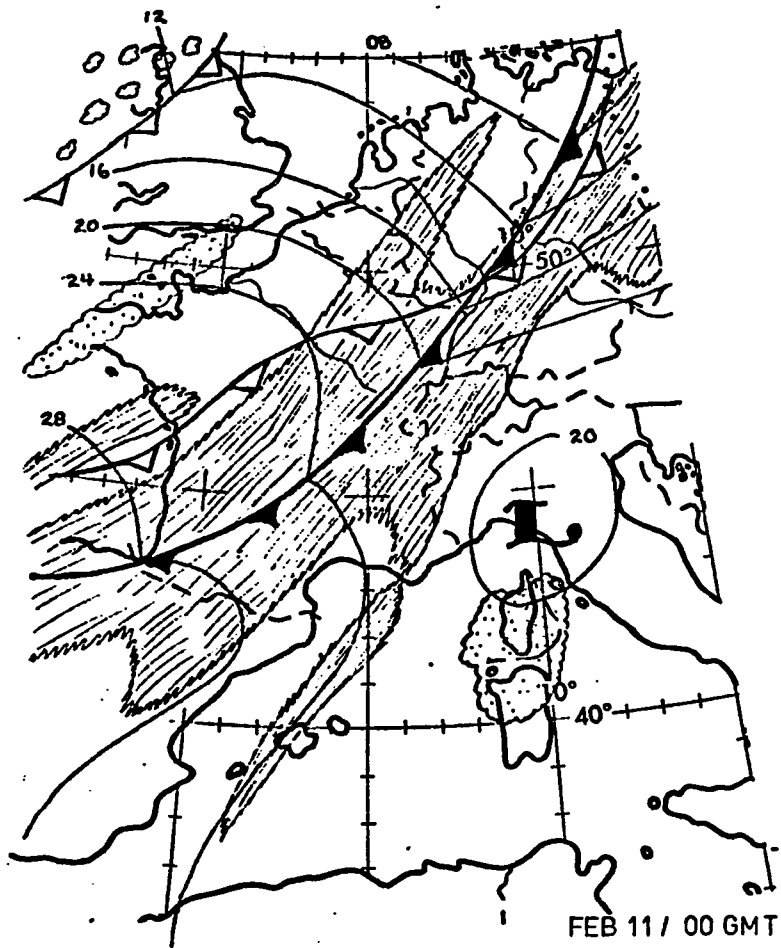
Figures IV-2 and 3 show surface and 500 mb charts for the region. Significant clouds obtained from visual satellite imagery are keyed on the figures as to their relative heights (low, middle, or high). Upper level flow to the west over the Atlantic showed an amplifying ridge and development of northwesterly flow over Europe. The upper disturbances associated with the surface cyclone development both moved southeastward and interacted strongly with the Alps. The frontal zones associated with these waves both underwent significant strengthening as shown in cross-sectional analyses (normal to the front) in Figures IV-4 and 5. These frontal intensifications were followed immediately by very rapid cyclogenesis. The initial conditions for both cases, with respect to winds, vorticity, and thermal gradients, were not extraordinarily strong. As such, these cases most likely represent the typical lee cyclogenesis, and should better reveal the influence of the mountains in the development process.

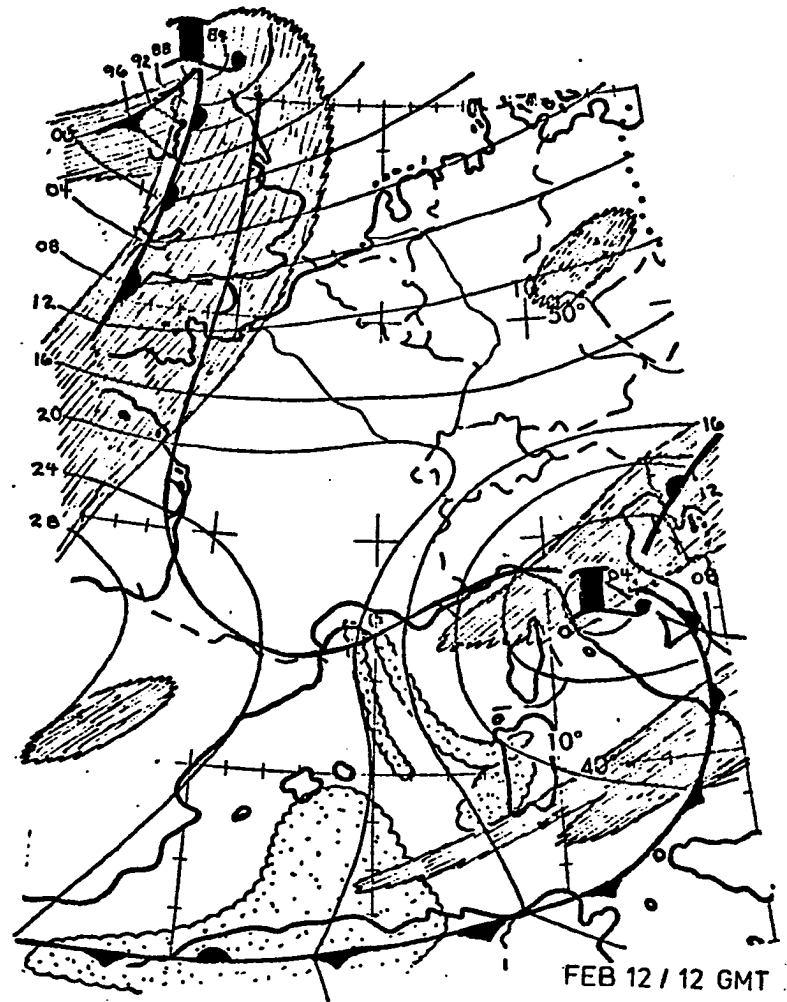
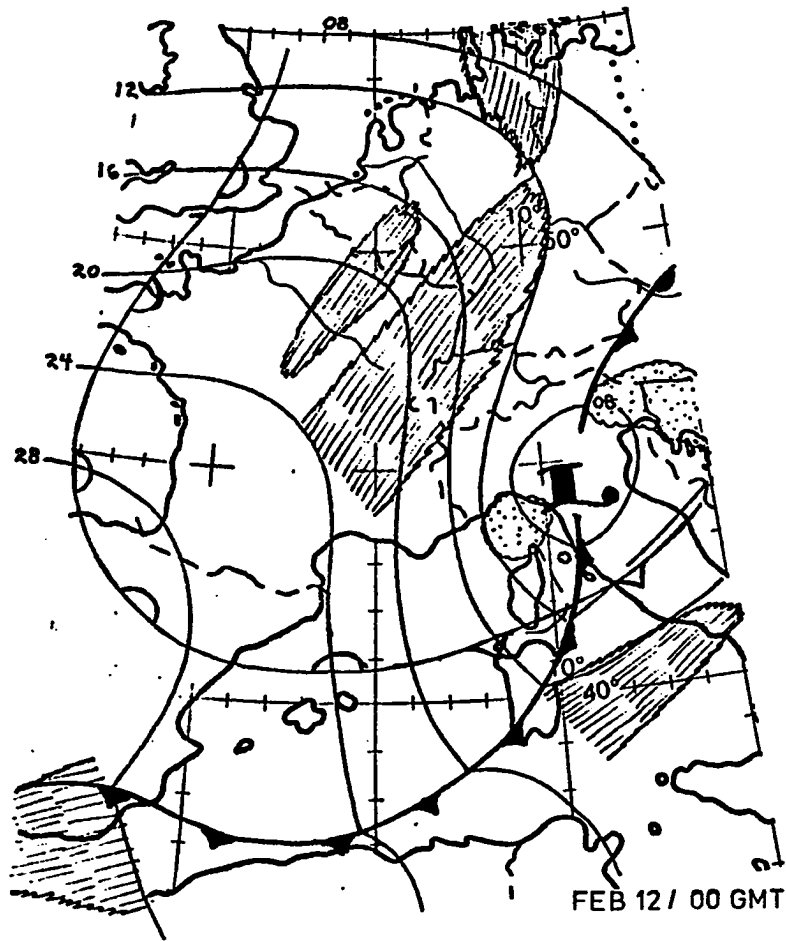
Quasi-Lagrangian Volumes

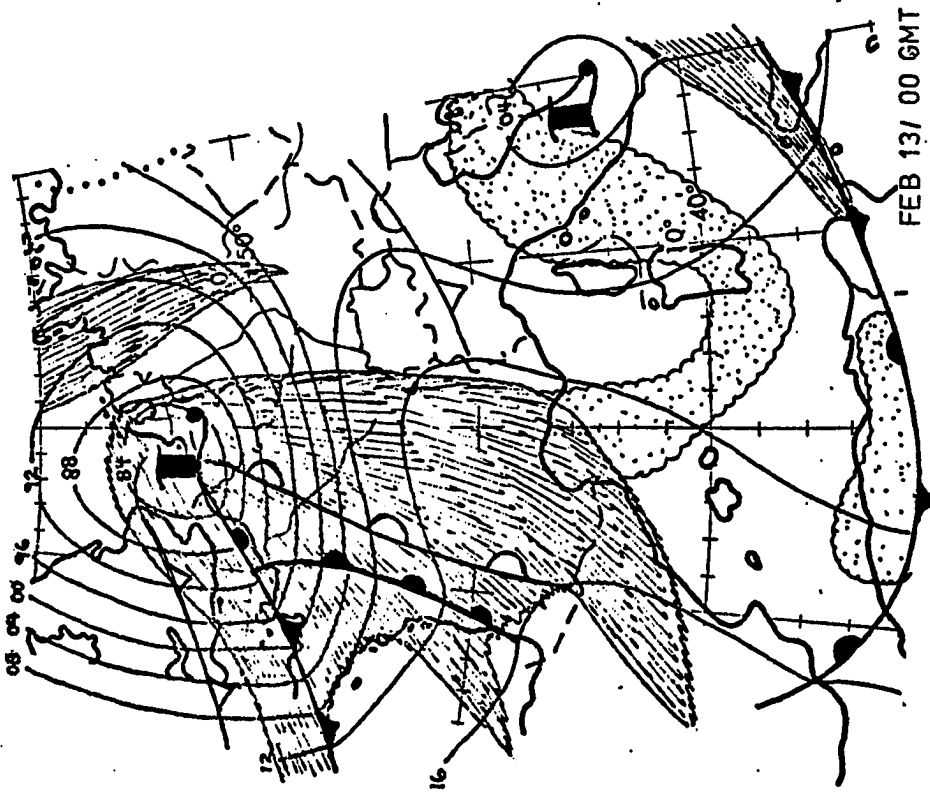
To facilitate the analysis of bulk quantities, the region is divided into sets of moving volumes designed so that the entire cyclone and upper wave is contained therein. This has been done in other studies by Wei (1979), and Sasaki and McGinley (1978). In addition, another volume element remains fixed to the lee region so that processes associated with the mountains may be more clearly seen. This is similar to techniques applied by Petterssen and Smebye (1971) and Tibaldi et al. (1980). Figure IV-6 illustrates the placement of a volume over a cyclone and frontal system. Some qualitative judgement is needed to decide where the volume should be. An effort is made to make a volume large enough to contain one wavelength of the upper initiating wave. As an example, Figure IV-7 shows placement of

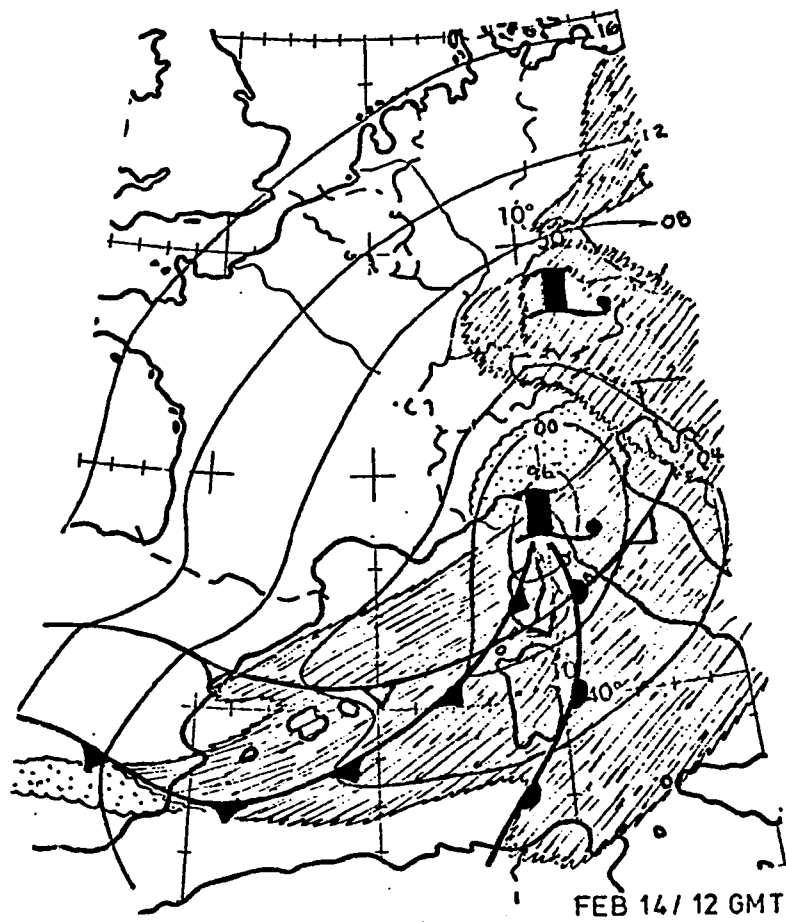
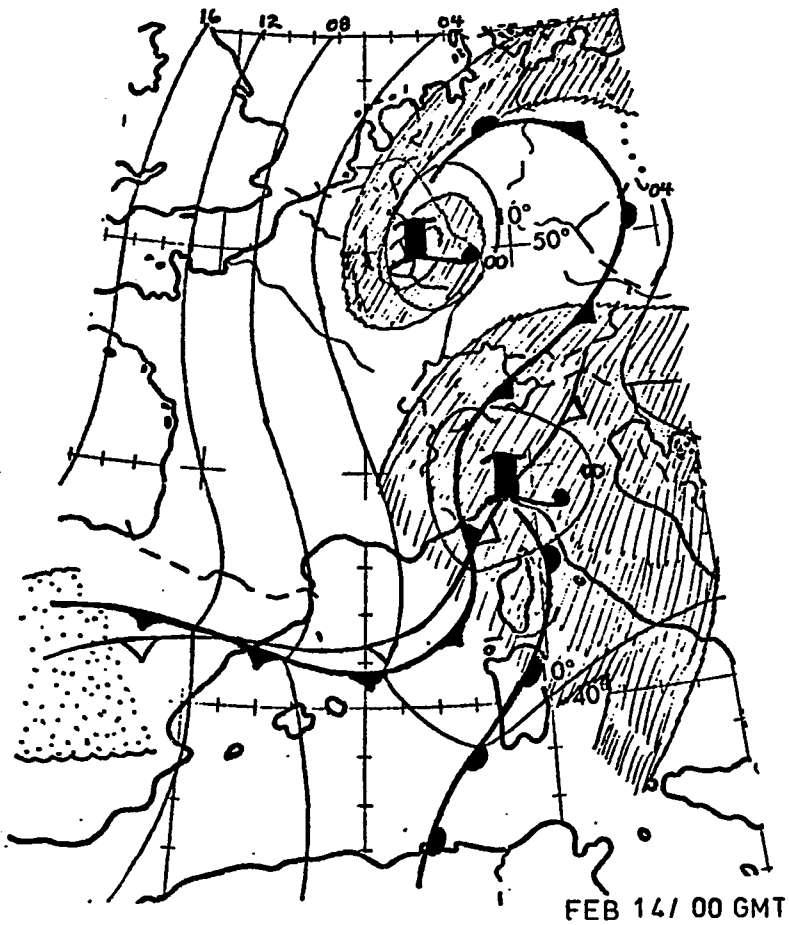
Fig. IV-2. Surface weather charts at 12 hour intervals from 11 Feb. 00 GMT to 15 Feb. 12 GMT. KEY:

	isobars (mb)		low pressure centers
	surface frontal position		high pressure centers
	700 mb frontal position		
	low to middle clouds		middle to high clouds
	precipitation		









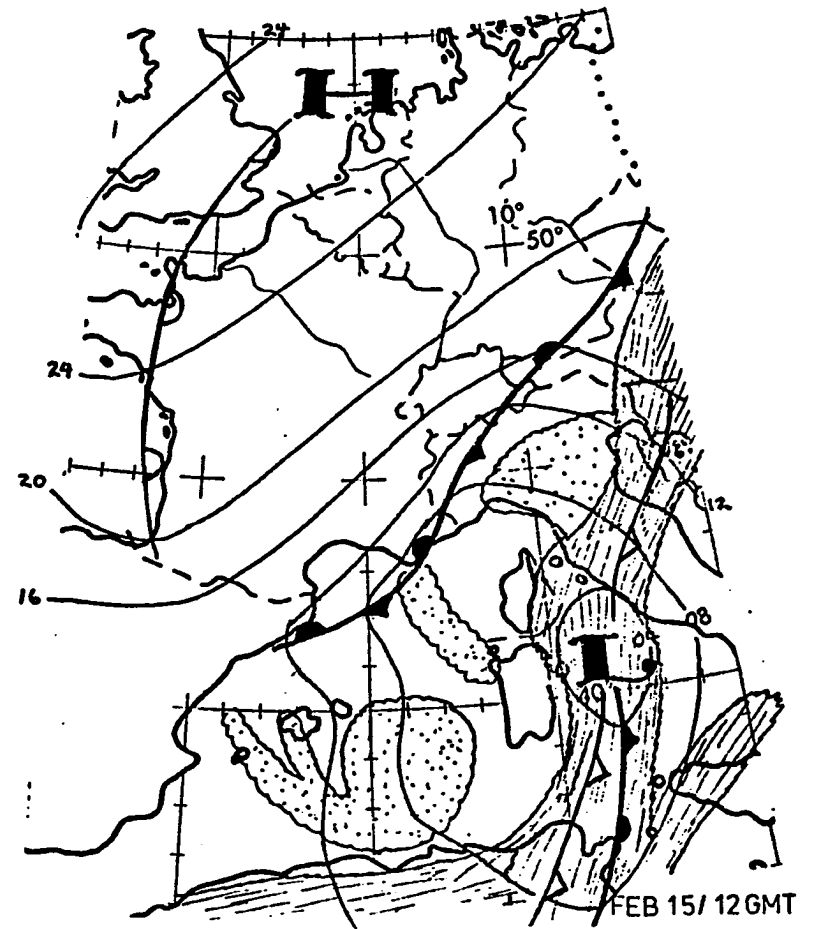
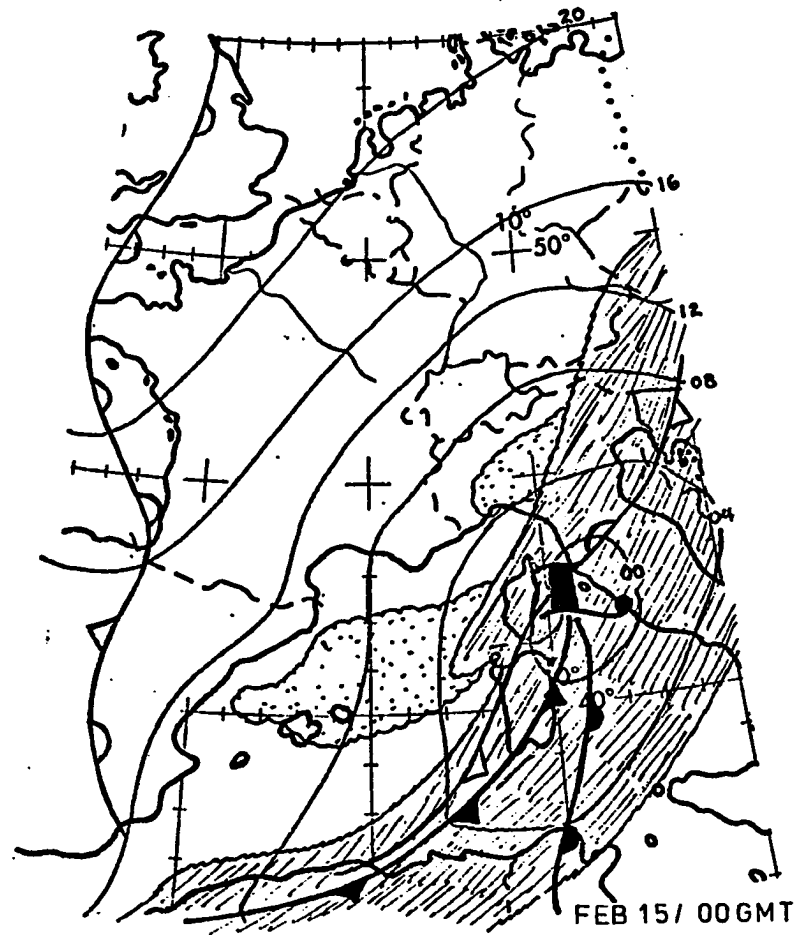
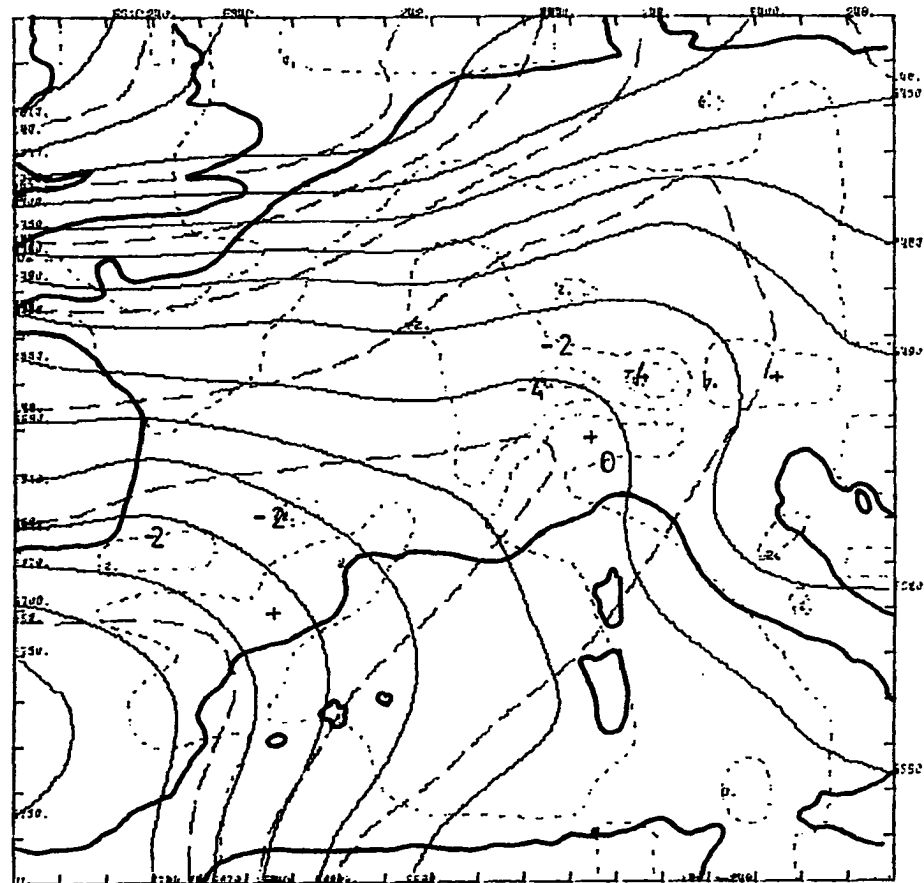


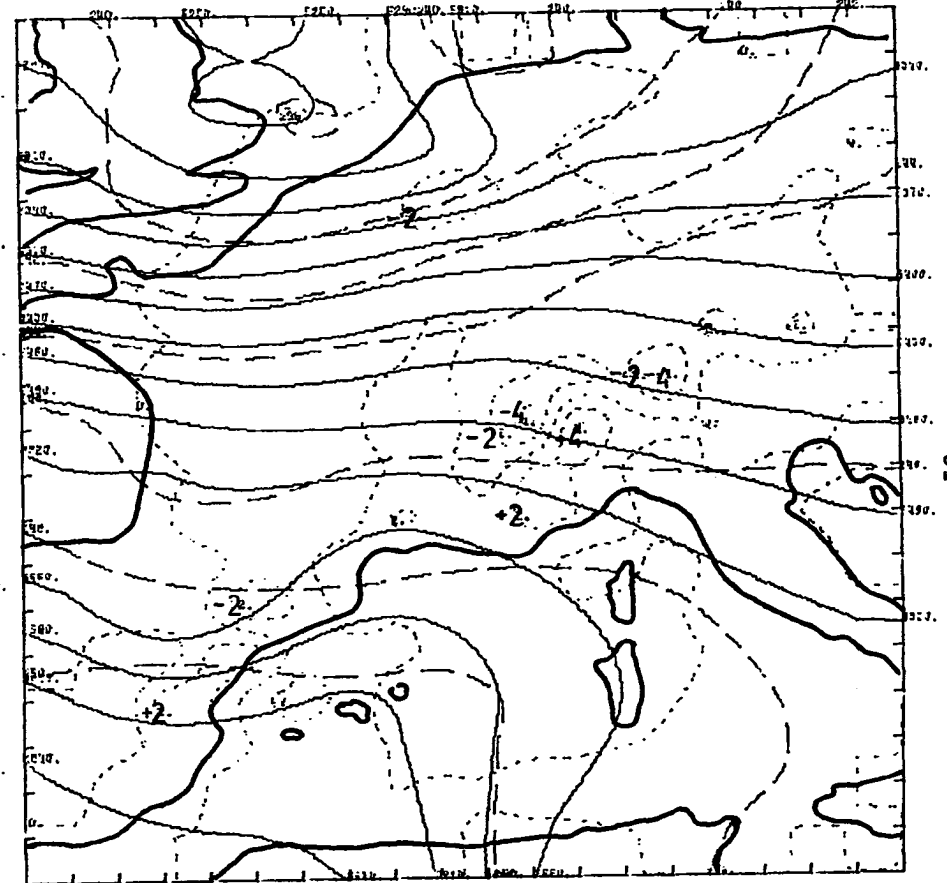
Fig. IV-3. 500 Millibar Charts at 12 hour intervals corresponding to surface charts in IV-2. Major geographic features are outlined.

KEY:

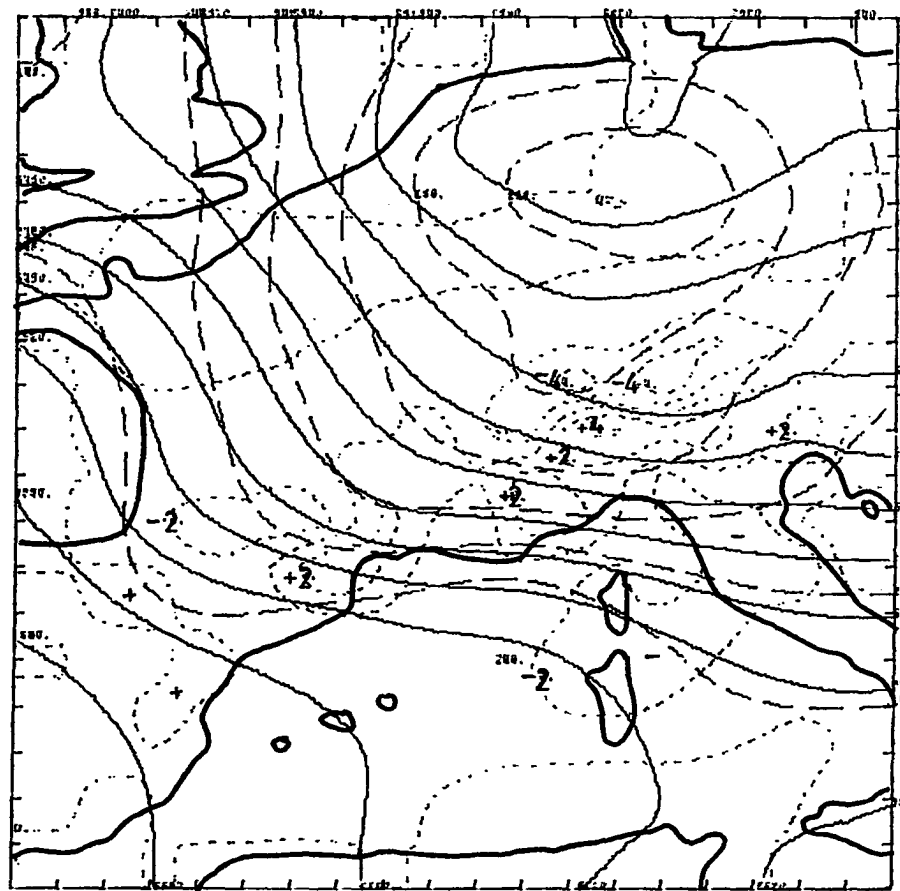
- geopotential/g (m)
- - - temperature ($^{\circ}$ K)
- vertical motion (omega, mb/sec x 10^{-3})



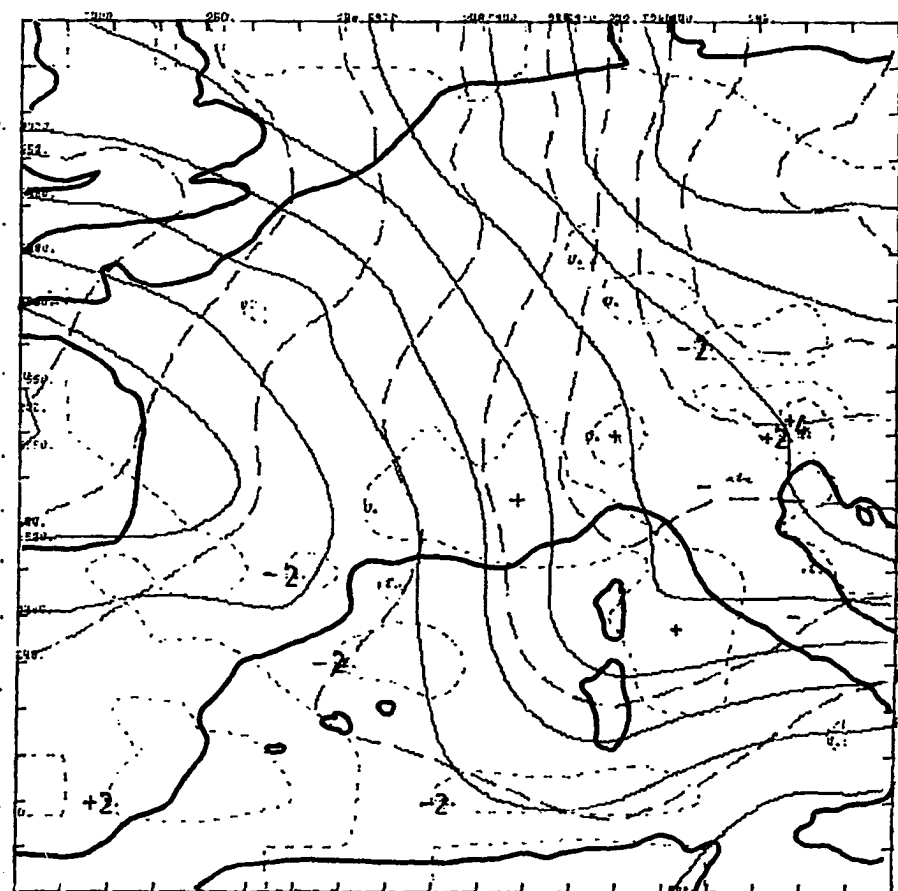
FEB 11, 1976 00 GMT LVL 500 MB



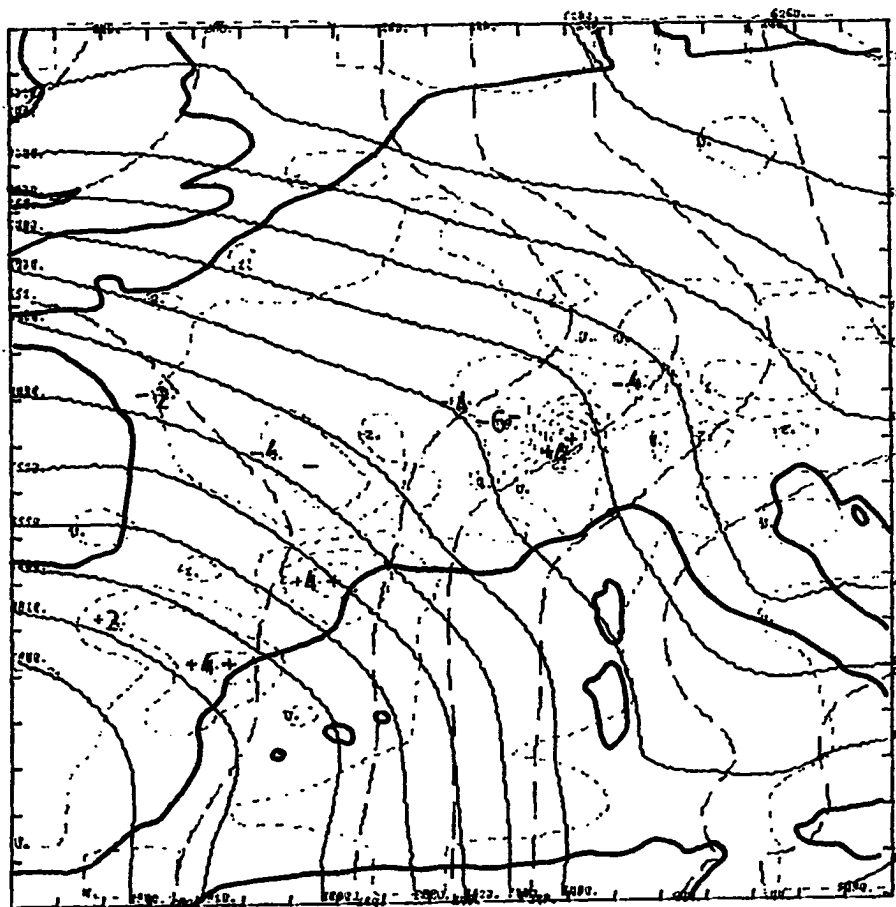
FEB 11, 1976 12 GMT LVL 500 MB



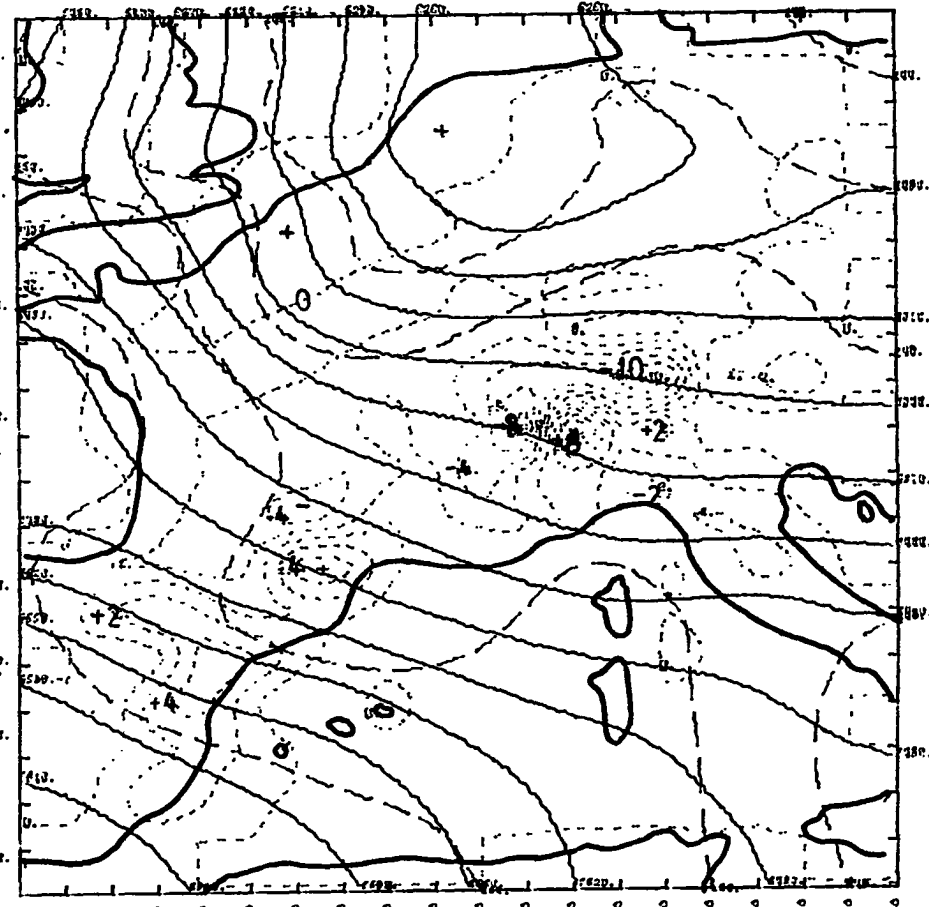
FEB 12, 1976 00 GMT LVL 500 MB



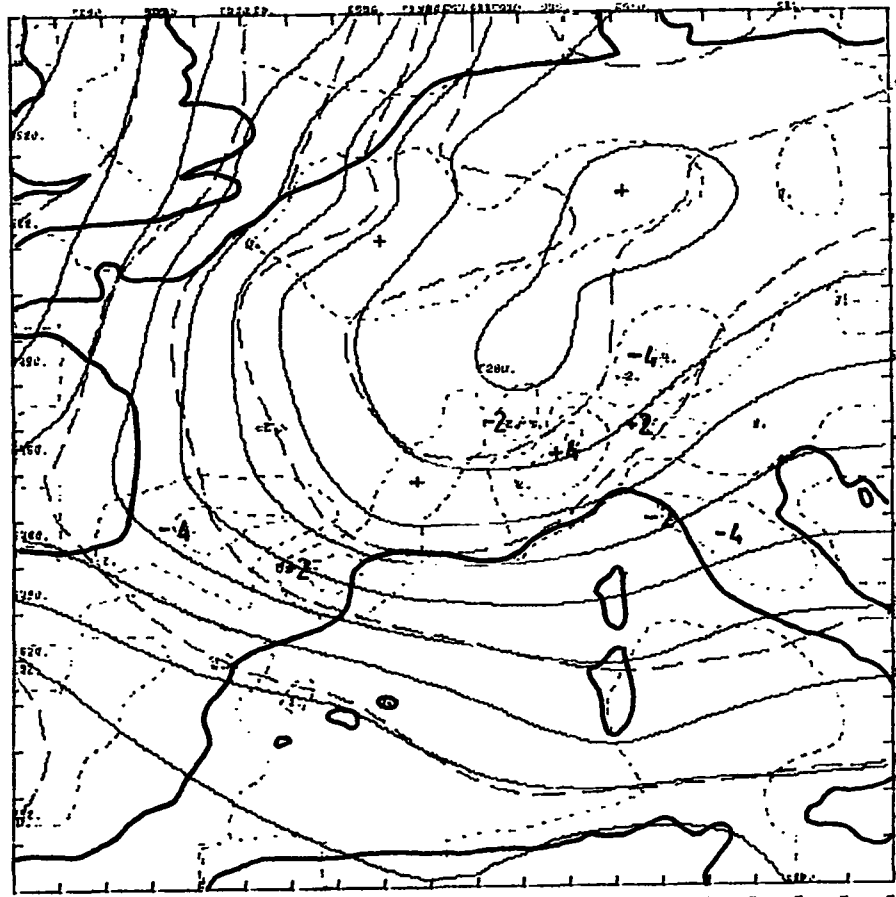
FEB 12, 1976 12 GMT LVL 500 MB



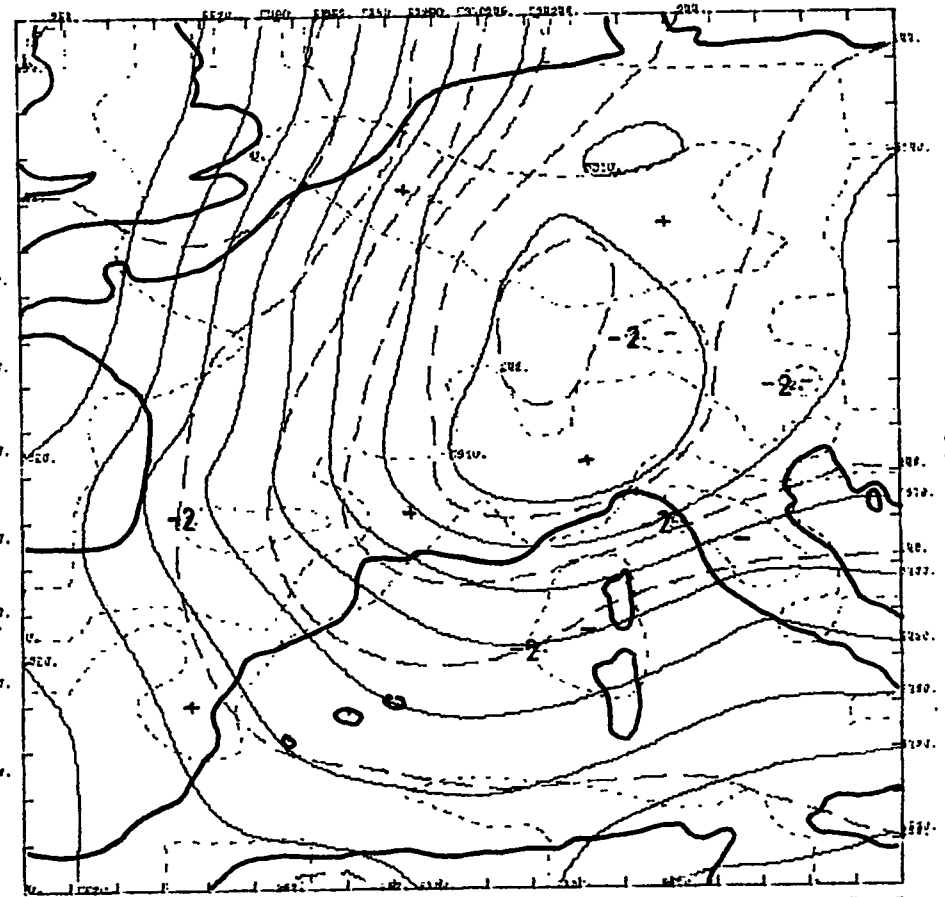
FEB 13, 1976 00 GMT LVL 500 MB



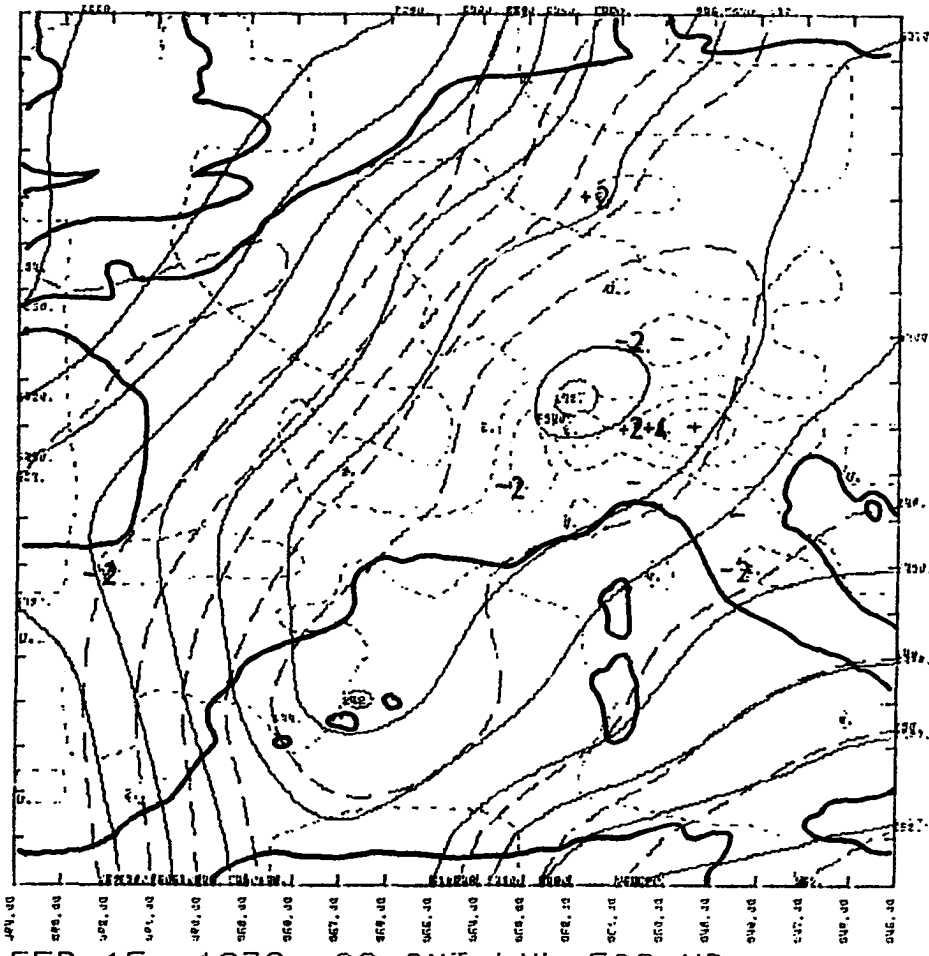
FEB 13, 1976 12 GMT LVL 500 MB



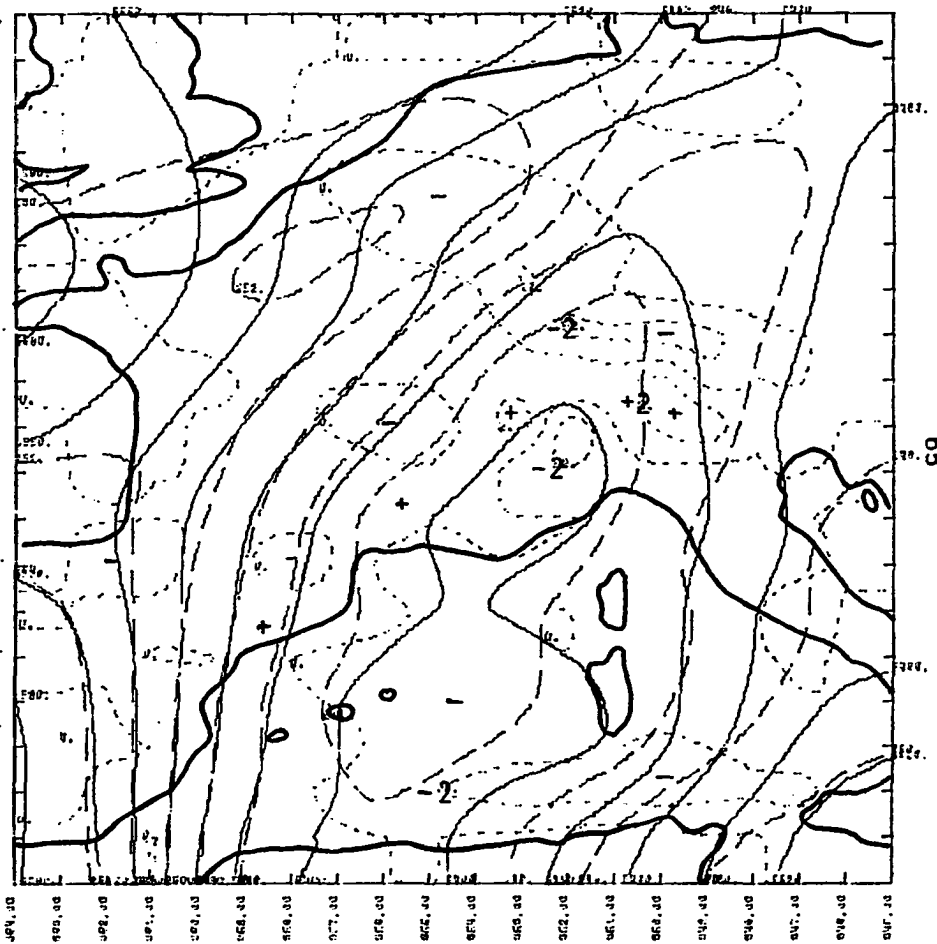
FEB 14, 1976 00 GMT LVL 500 MB



FEB 14, 1976 12 GMT LVL 500 MB



FEB 15, 1976 00 GMT LVL 500 MB



FEB 15, 1976 12 GMT LVL 500 MB

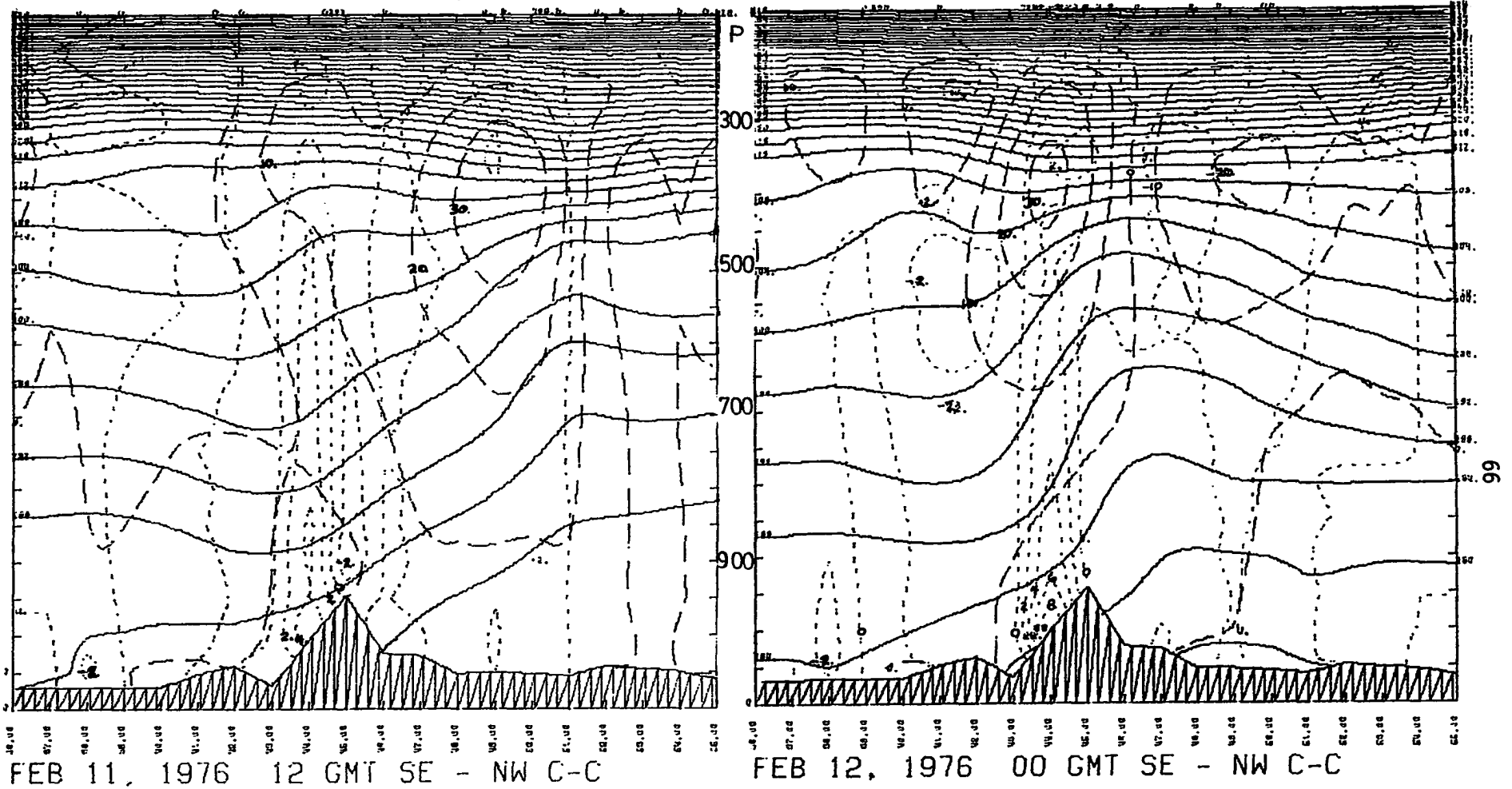


Fig. IV-4. Southeast to northwest cross section through frontal zone for 11 Feb. 12 GMT and 12 Feb. 00 GMT. Solid lines are isentropes (deg); dashed lines are winds normal to cross section (m/sec); and dotted lines are omega values (mb/sec x 10⁻³). Peak at 46 N is a portion of the Alpine-Pyrenees chain. Note how strengthening of baroclinic zone occurs (increased net slope of isentropes) during period.

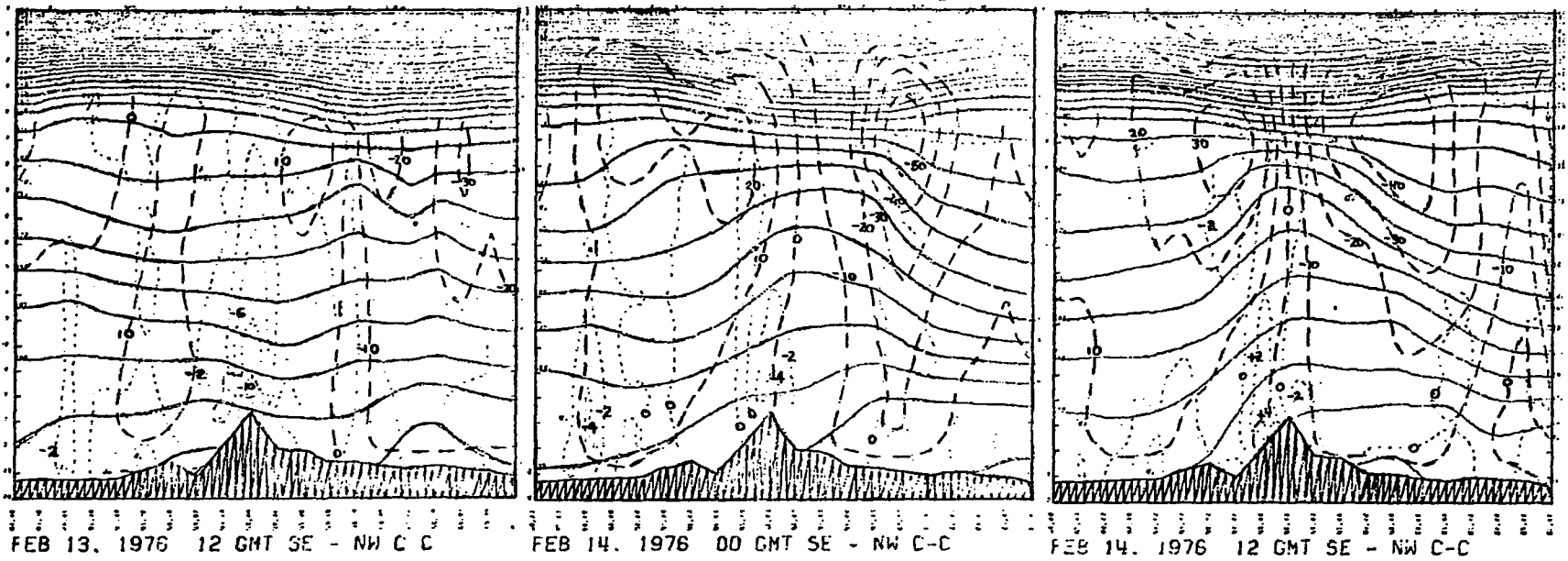


Fig IV-5. Southeast to northwest cross section for 13 Feb. 12 GMT through 14 Feb. 12 GMT. Symbols are described in caption for IV-4. Similar frontal zone strengthening is seen here as well.

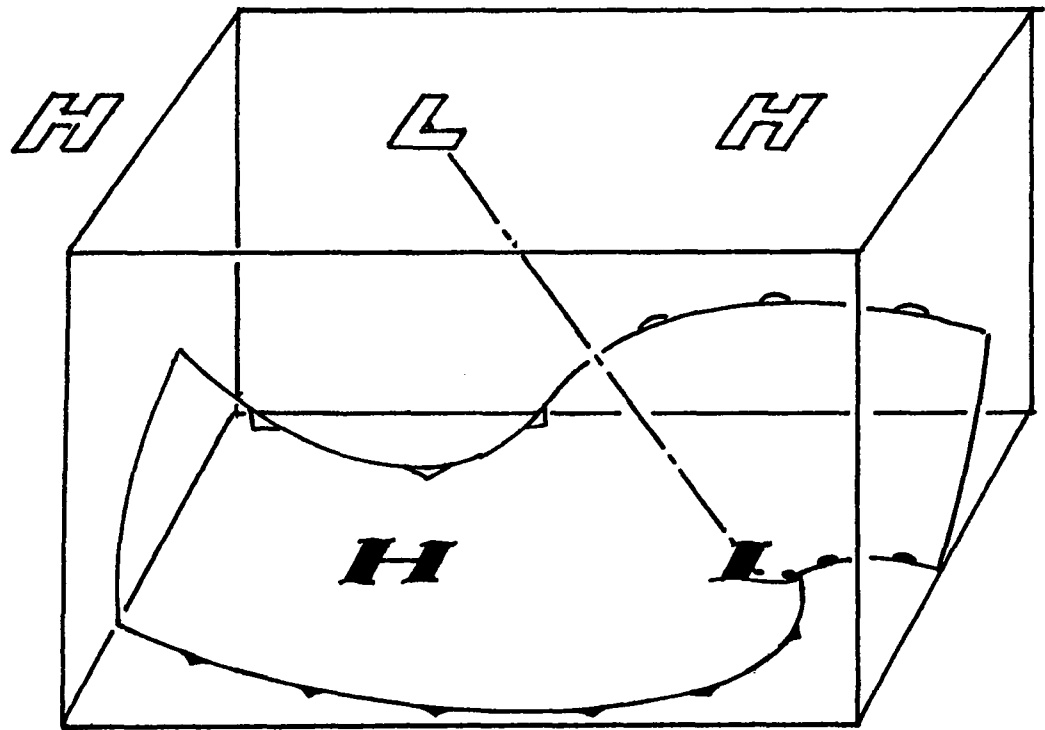


Fig. IV-6. Schematic illustration showing placement of a volume over a cyclone/frontal zone system. Solid symbols show surface positions, while open symbols indicate upper air. Top of volume was 200 mb level. Boundaries of volume are selected to minimize energy flux as shown in Appendix 7.

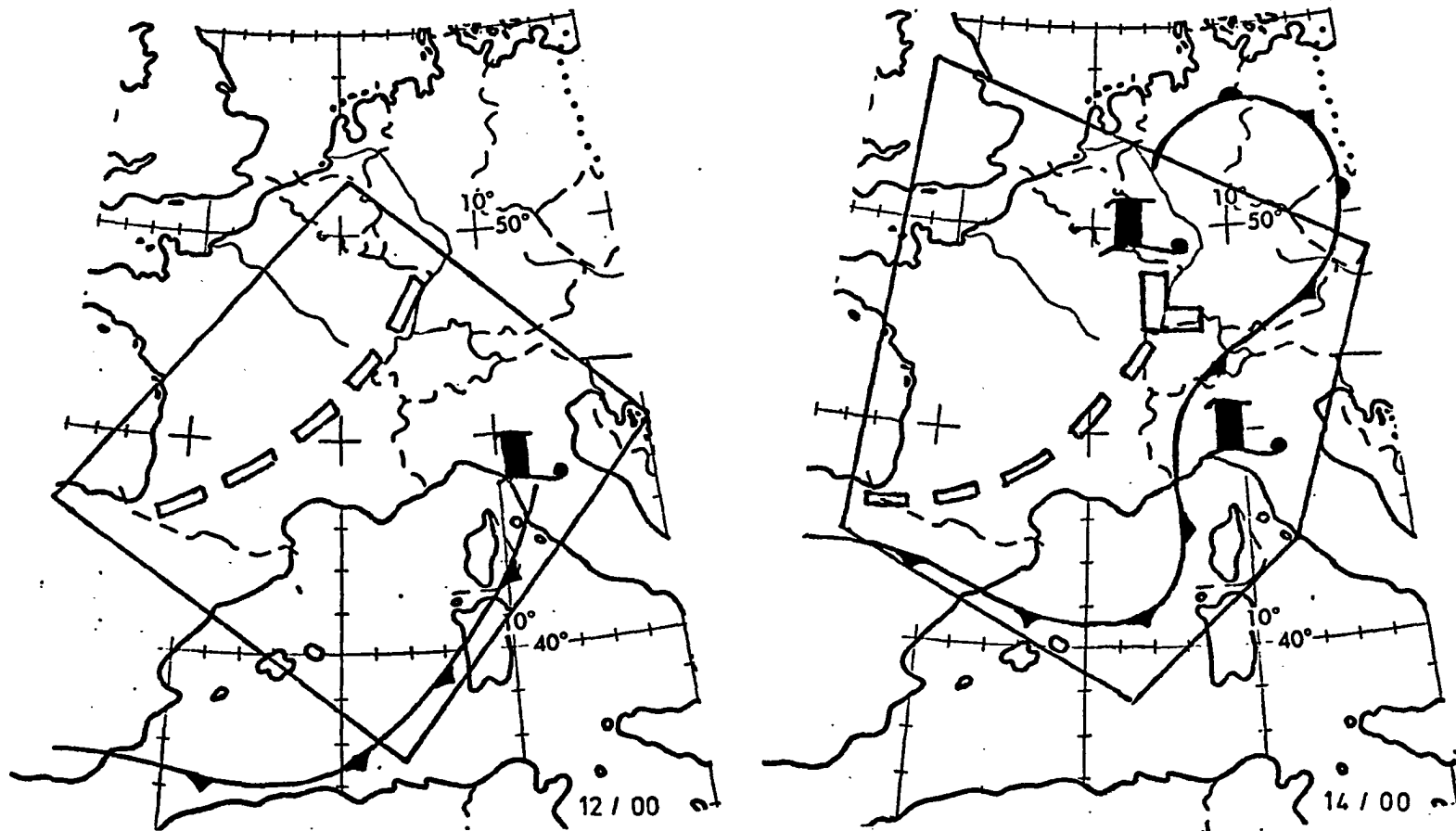


Fig. IV-7. Actual placement of volume over systems on 12 Feb. 00 GMT and 14 Feb. 00 GMT during LCD I and LCD II, respectively. Solid symbols indicate surface positions, while open symbols are upper air (500 mb) positions. The broken line indicates the 500 mb trough axis.

volumes over features at 00 GMT Feb. 12 and 12 GMT Feb. 14.

As the frontal zones interacted with the mountains there was an increase in the horizontal temperature gradient. This has been seen previously in other cases (Sasaki and McGinley, 1978), and served as the prime motivation for this study. Figure IV-8 shows the mean frontal strength in the volume as a function of time for both LCD I and II. Symbols indicate when the leading edge of the 700 mb frontal zone was positioned over the Alps-Pyrenees axis. Clearly the frontal strength increased significantly as it interacted with the mountains. In addition to previously mentioned studies, numerical work by Merkin (1975), and Trevisan (1976) showed similar frontal zone evolution.

It seems clear that the mountain range played some role in the frontogenetic process. Figure IV-9 presents the wind deformation and vertical motion field at 600 mb for LCD I (12 GMT Feb. 11). This level is just above the highest peaks in the Alps. The axis of dilatation associated with the deformation field reveals that a portion of the flow split and moved around the Alps. The vertical motion field shows the up/down couplets which create frontogenesis through the tilting term. The frontogenetical rate is shown on Figure IV-9c, which illustrates the combined effect of both processes. Near the mountain the frontal zone increased by a factor of 2 every 12 hours. The influence of the frontal strengthening can extend to levels above the terrain because of the coupling of the thermal fields and wind shear. Figure IV-9d shows the flow deflection at 500 mb owing to the frontal strengthening and retardation of the cold air by the mountains.

A good share of the mean flow impinging on the northwest face of the Alps is forced up and over the barrier. This is shown in the following

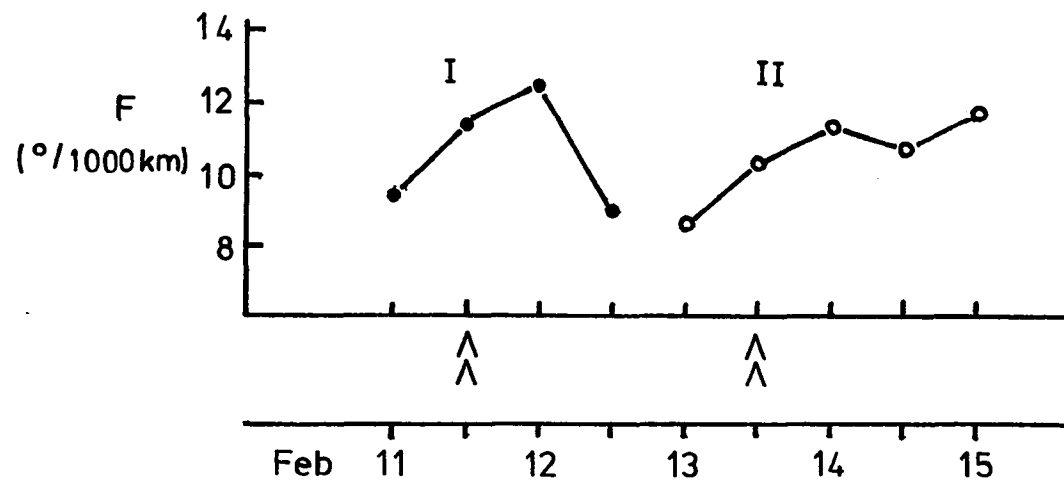
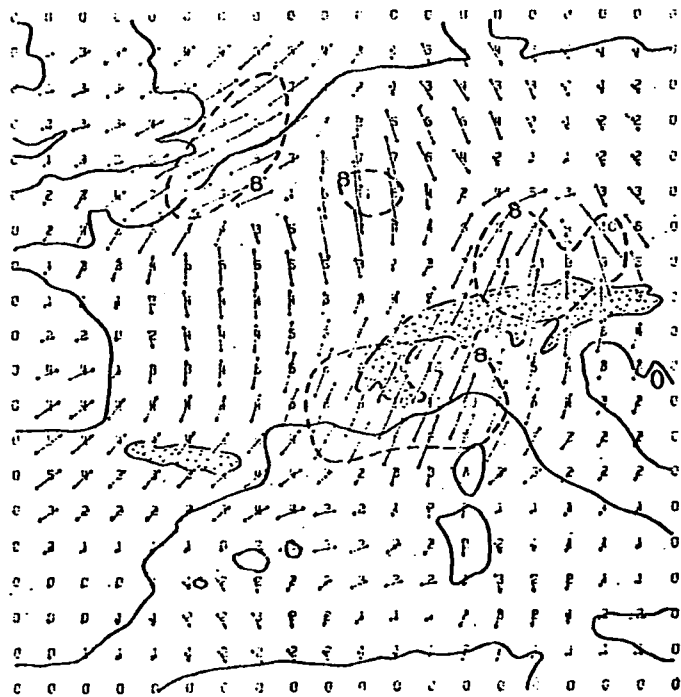
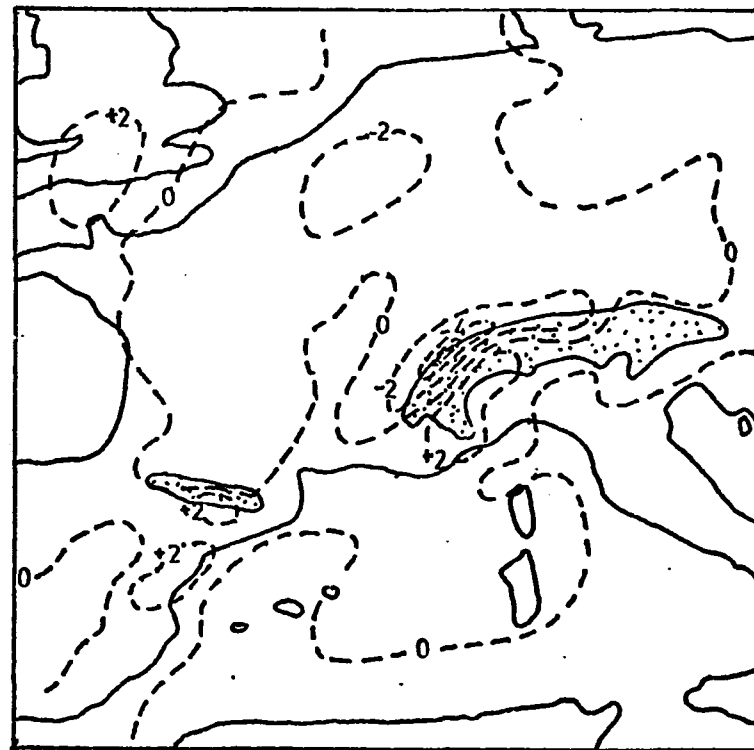


Fig. IV-8. Mean frontal zone strength within volume versus time for both cases. Mountain symbol indicates time when southern edge of 700 mb baroclinic zone was over the Alps-Pyrenees axis.



a.



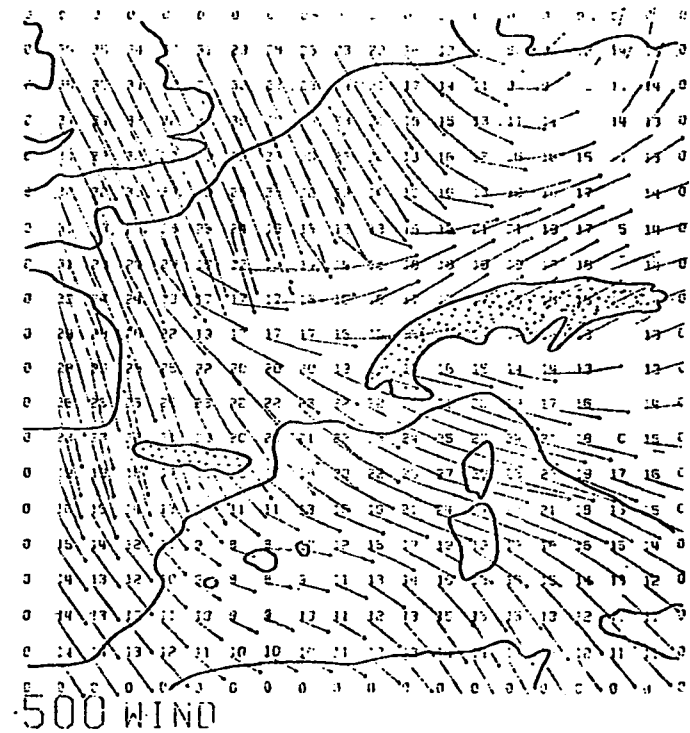
b.

Fig. IV-9. Frontogenetic components over region at 700 mb on 11 Feb. 12 GMT.

- a. Flow deformation with axis of dilatation indicated, ($\text{sec}^{-1} \times 10^{-5}$).
- b. Vertical motion (ω) in $\text{mb}/\text{sec} \times 10^{-3}$.



c.



d.

Fig. IV-9. Frontogenetic components over region at 700 mb on 11 Feb. 12 GMT.

- c. Frontogenesis rate, (deg K/1000km-sec x 10^{-4})
- d. Wind flow at 500 mb, (m/sec)

table which decomposes the frontogenetical rate into the component terms. Owing to a lack of rainfall and radiation data, the effects of diabatic processes could not be explicitly evaluated.

Table IV-1

Components of Frontogenesis for a Region Within 100km of the Alps (deg/1000km/24hr)				
Period	Total	Deformation/ Convergence	Tilting	Observed Change in Frontal Strength for Portion Crossing the Alps
11/00 to 12/00 GMT	22.5	2.0	20.5	21.2
13/00 to 14/00 GMT	37.6	3.8	33.8	27.5

The table shows that tilting is the most important mechanism for the frontal intensification. The observed frontal strength is computed for a small volume which follows the front and interacts directly with the Alps.

Figure IV-10 illustrates the change in low level baroclinicity for the two cases. The blocking by the Alps and surging of the air down the Rhone Valley has been shown to alter the shape of the front as well. This is seen here to some extent, but better examples can be seen in the other cited studies.

Vorticity

Figures IV-11, 12 show vorticity at 850 mb for the two lee cyclone periods. Weak cyclones formed 12 to 24 hours prior to the rapid cyclogenesis. The major developments occurred between 00 and 12 GMT on 12 Feb and from 12

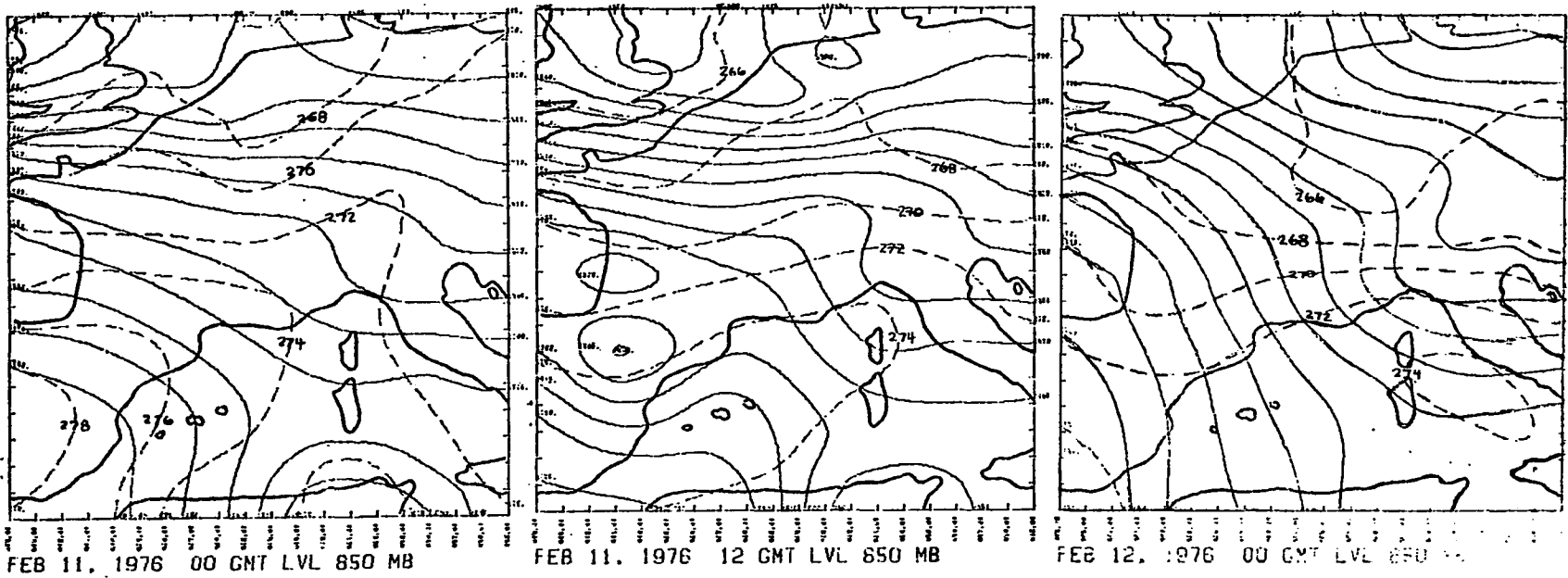


Fig. IV-10a. Geopotential (—), and temperature (---) fields at 850 mb, showing increase in horizontal temperature gradient as frontal zone interacts with mountain range on Feb. 11 and 12.

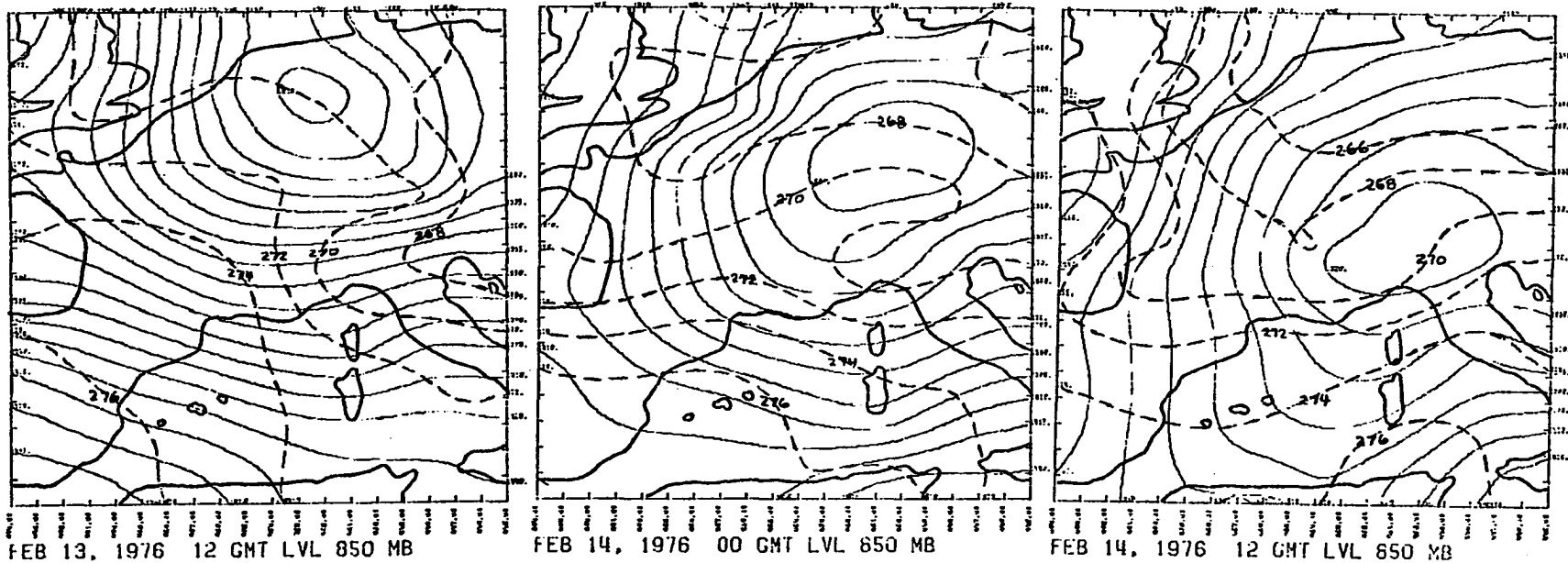
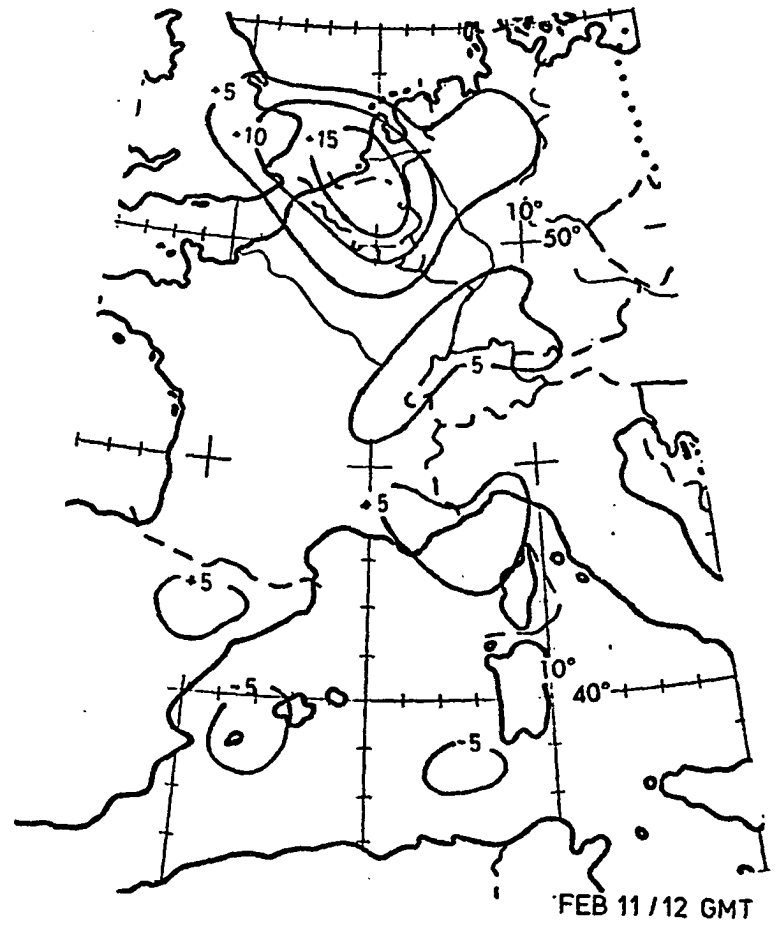
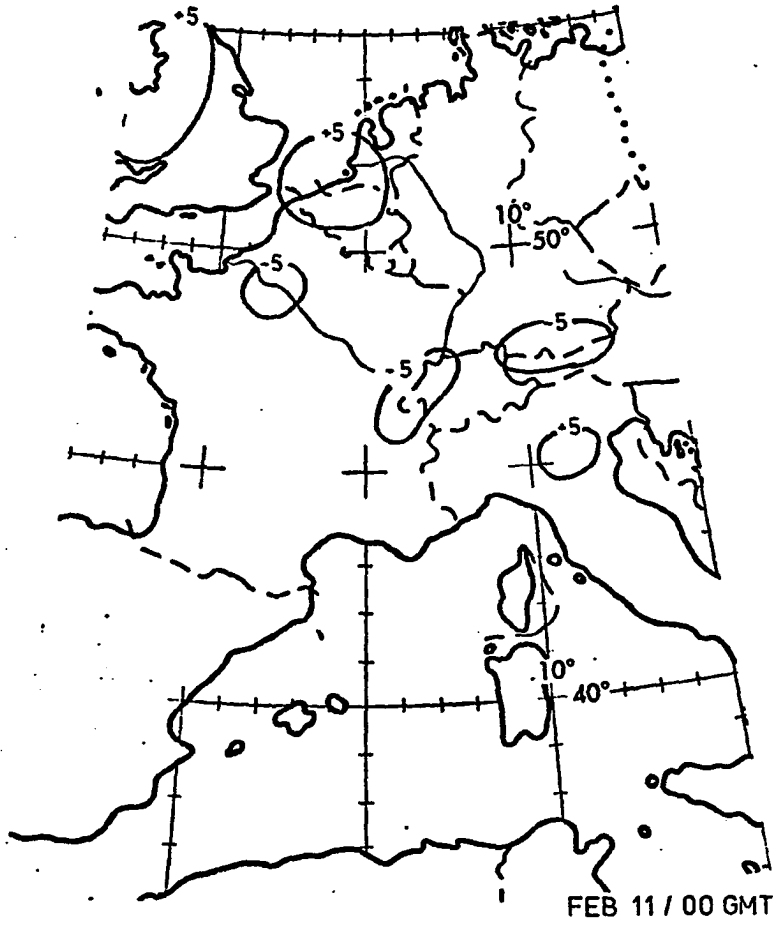


Fig IV-10b. Geopotential (—) and temperature (---) fields at 850 mb, showing increase in horizontal temperature gradient as frontal zone interacts with mountain range on Feb. 13 and 14.

Fig. IV-11. Relative vorticity for 850 mb during period 11 to 12 Feb. for
LCD I. Vorticity is in units ($\text{sec}^{-1} \times 10^{-5}$).



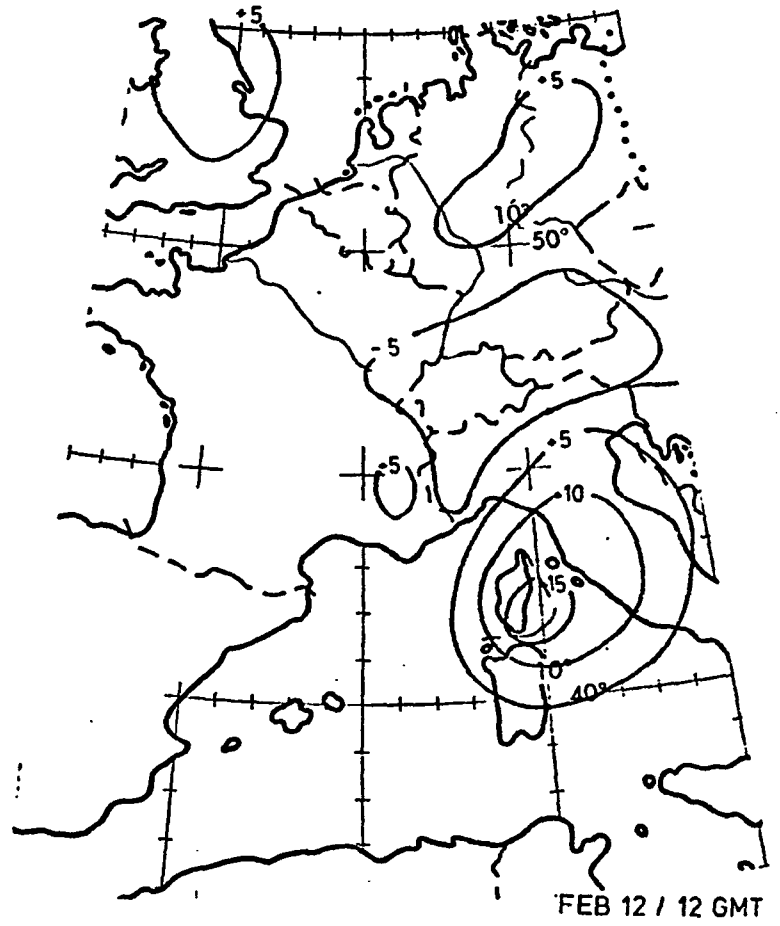
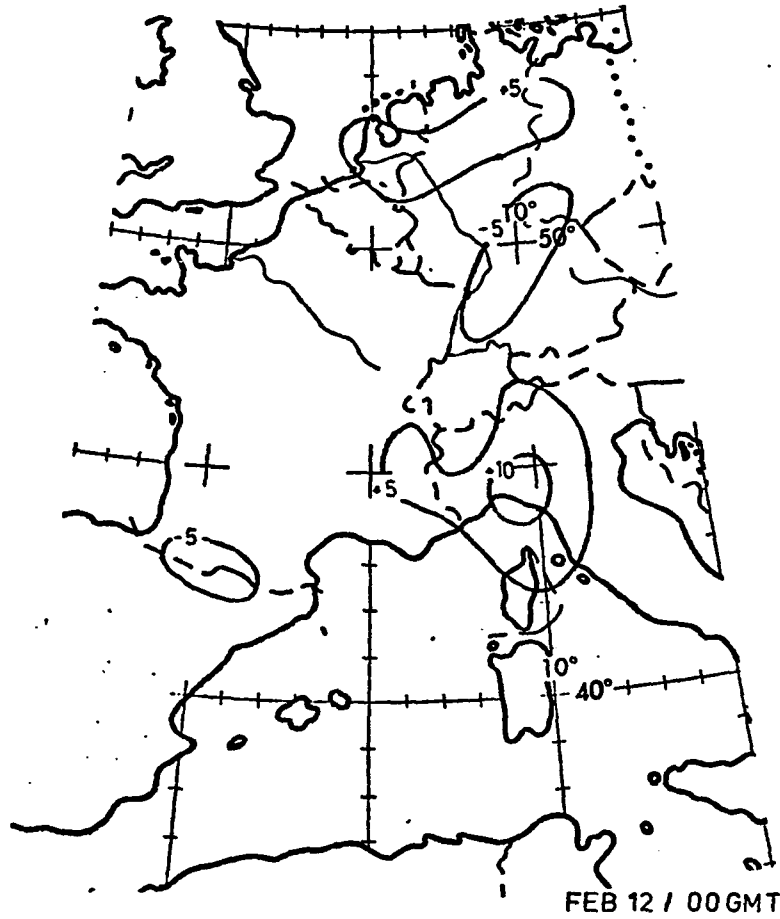
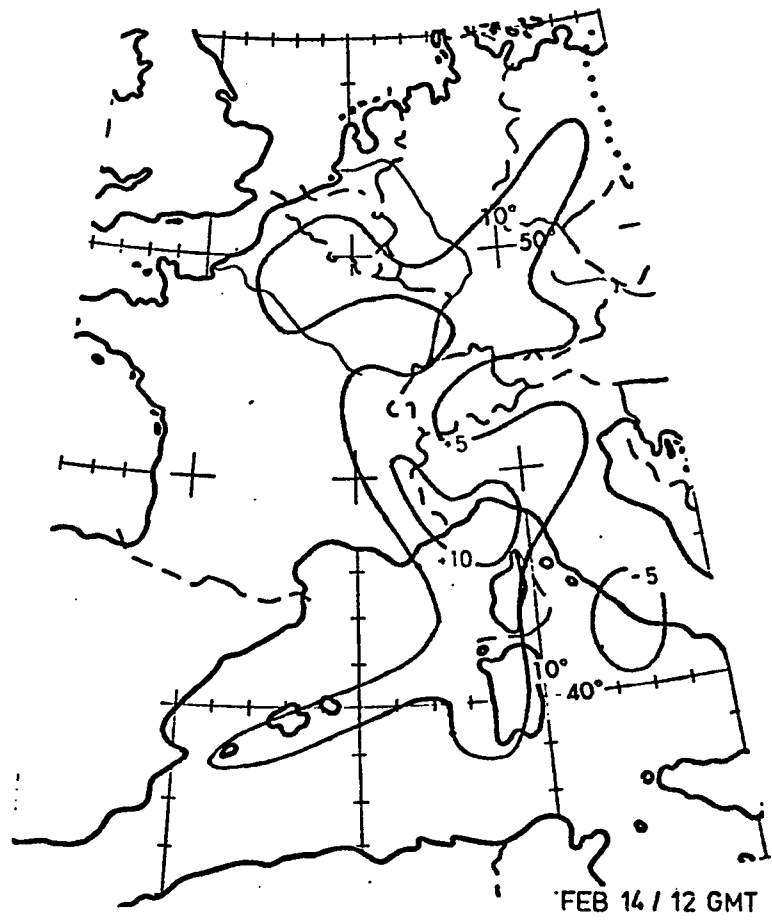
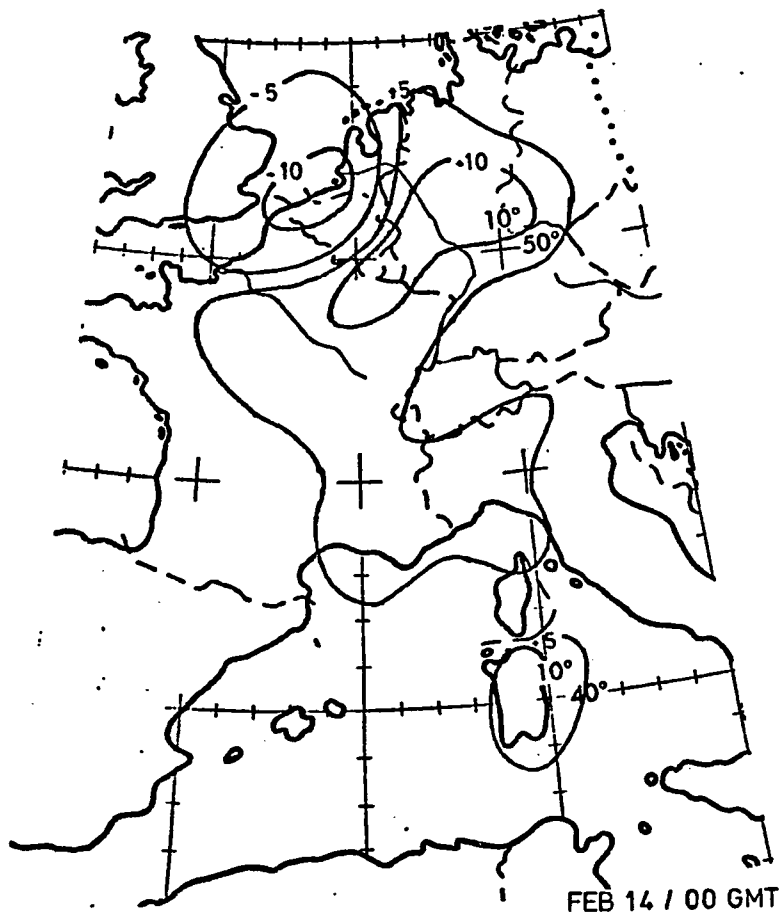
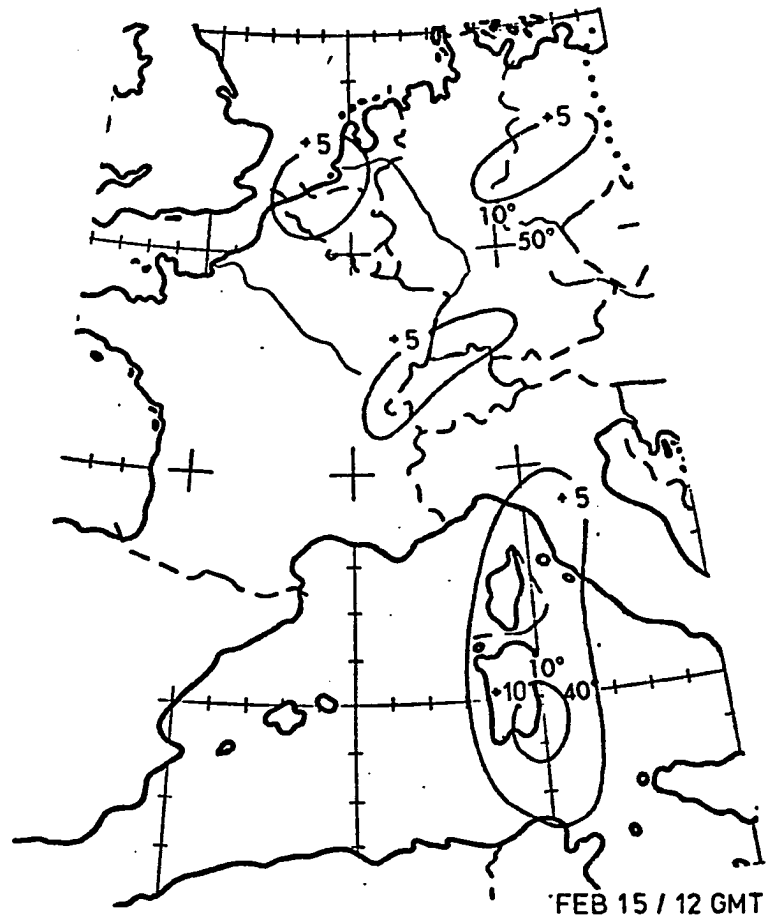
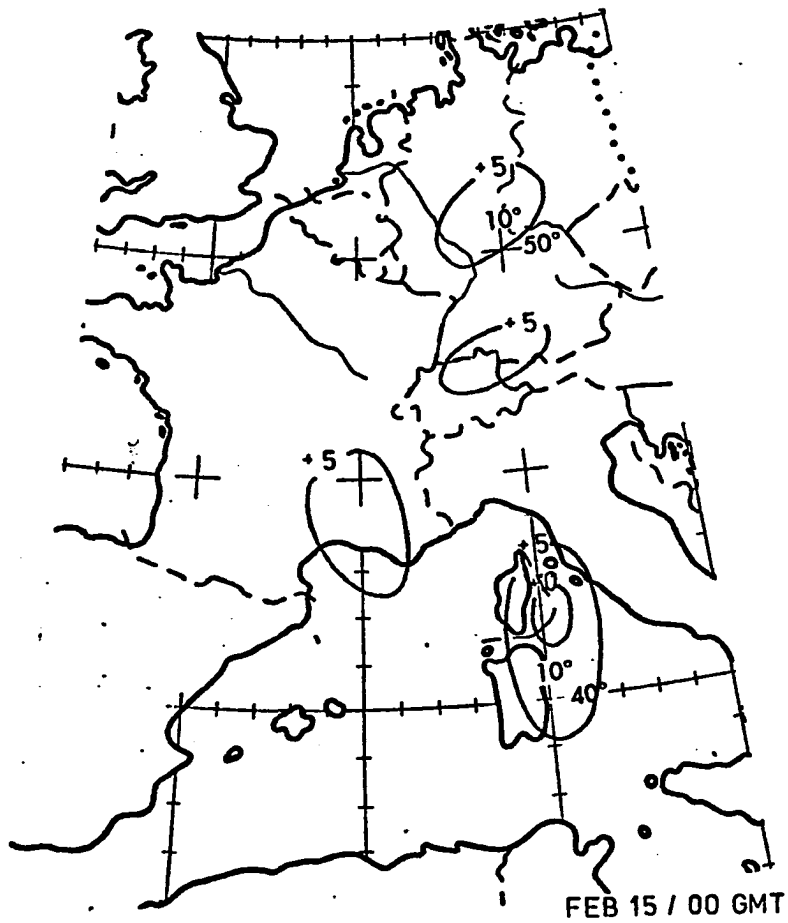


Fig. IV-12. Relative vorticity for 850 mb during period 13 to 15 Feb. for ICD II.





GMT 13 Feb to 12 GMT 14 Feb. An interesting feature is the evolution of the vorticity axis with time. This is shown in Figures IV-13. Note that when development occurred the axis was nearly vertical.

Previous investigators (Buzzi and Tibaldi, 1978; Petterssen and Smebye, 1971; and Phillips, 1979) indicate that lee cyclogenesis occurs in two stages. In the first, a cyclone or relative vorticity maximum forms in response to flow over the barrier, normal to the ridge line. This phenomenon, a consequence of conservation of potential vorticity, also induces an anticyclone over the mountain. Buzzi and Tibaldi (1977) attribute the strengthening of this cyclone to Ekman effects. However, the maximum strength and depth that a typical lee cyclone can attain is limited. In the second stage, the superposition of vorticity advection and consequent upward vertical motion (associated with an approaching upper level wave), combine with the low level effects of blocked cold air and downslope motion to produce rapid cyclogenesis in what Petterssen terms a "Type B" development. This disturbance is characterized by a circulation axis that is nearly vertical, in contrast to the more classical "Type A" structure which has an axis that tilts westward with height. Our analysis suggests that LCD I was a Type B development, while LCD II was more a Type A.

From another view, we can look at the Eulerian changes in vorticity and vertical velocity for the volume (see Figure IV-14) placed in the lee of the Alps. In Figure IV-15, horizontally averaged vorticity is plotted against time, for both LCD I and LCD II. The evolution clearly shows the change from the primarily terrain induced shallow system (call this the orographic stage), characterized by downward vertical motion at low levels and negative vorticity advection aloft, to the deep system with strong upward motion at middle and upper levels and rapid increases in vorticity. The

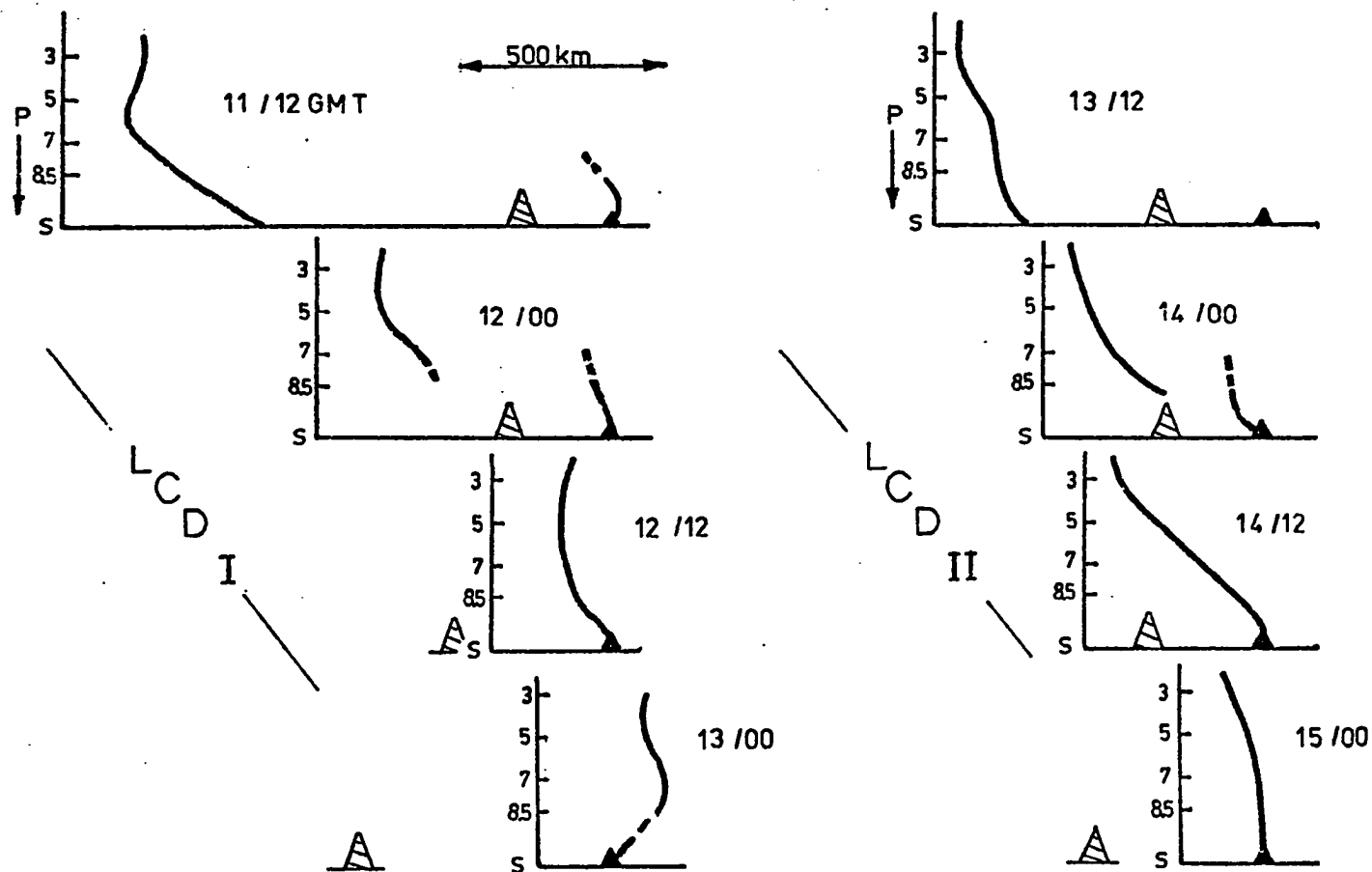


Fig. IV-13. Tilt of disturbance along a northwest-southeast axis. Solid line indicates minimum height as a function of pressure, horizontally displaced from lee cyclone, (▲). Symbols, (▲), show position of Alps along tilt axis. These figures show the early development is primarily along a vertical axis, with upper air system decoupled from the lower. During and after rapid development the two systems are strongly linked.

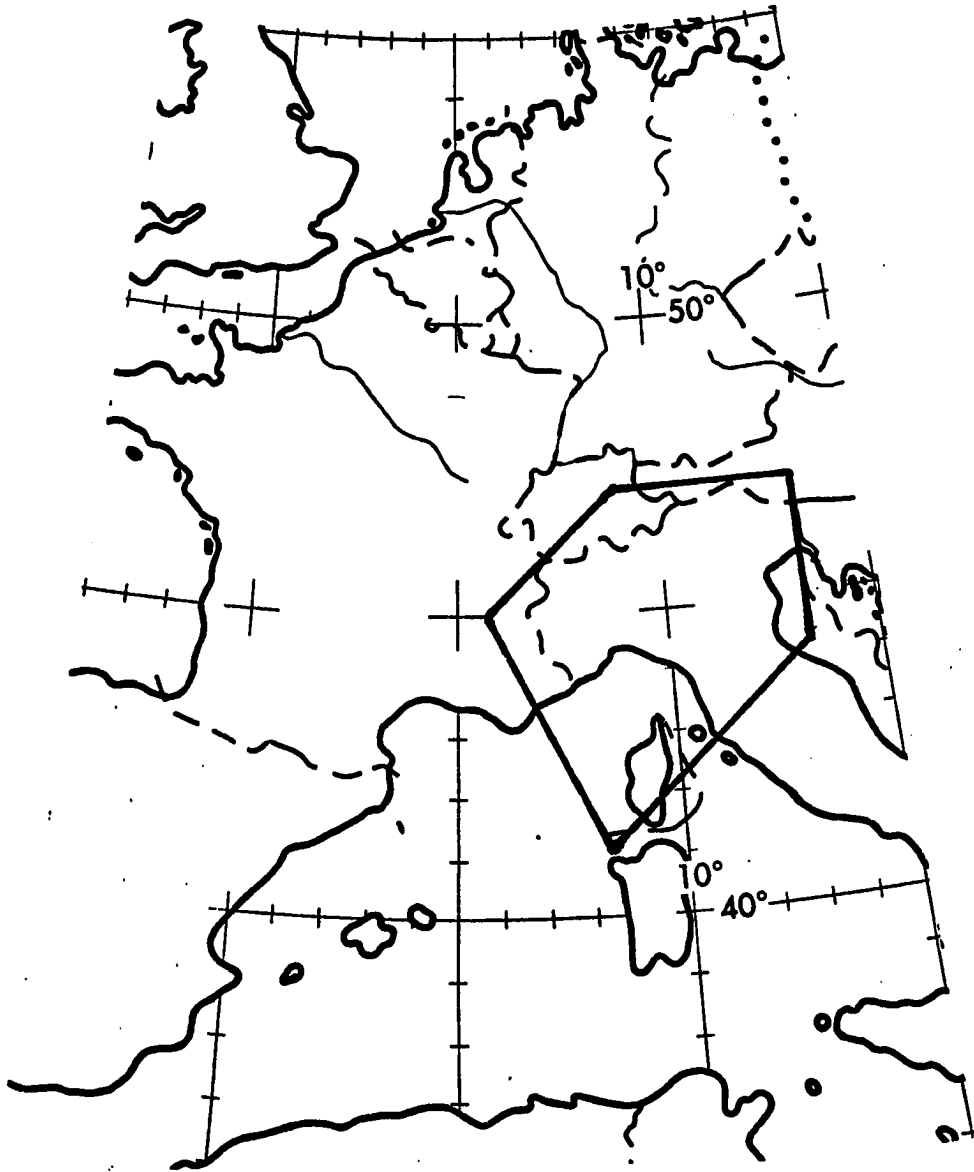


Fig. IV-14. Eulerian volume in lee of the Alps for time plot of vorticity and vertical motion.

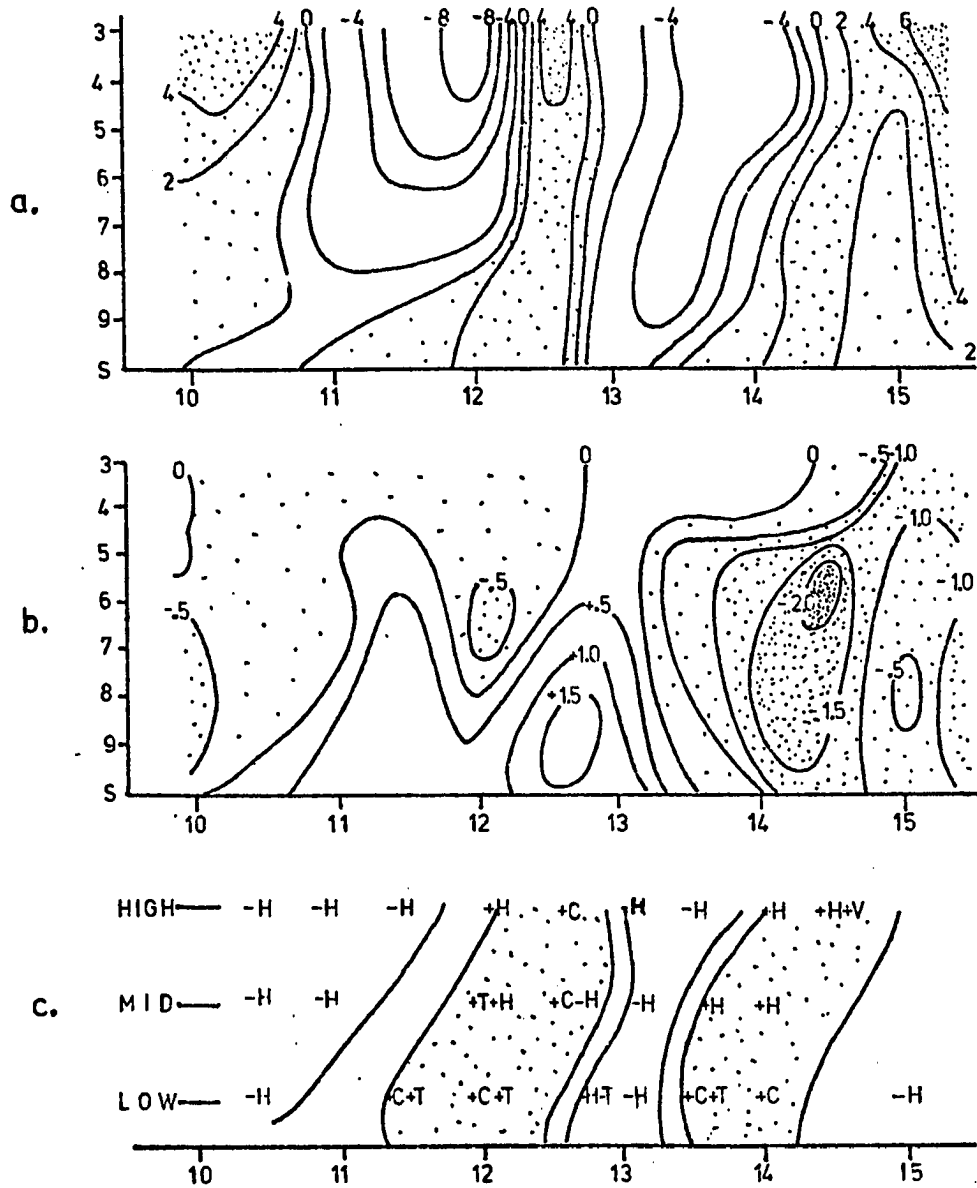


Fig. IV-15. Vertical distribution of quantities with time in the volume in the lee of the Alps specified in fig. IV-14.

a. Relative vorticity, with positive areas shaded, ($\text{sec}^{-1} \times 10^{-5}$).

b. Omega, with upward motion shaded, ($\text{mb}/\text{sec} \times 10^{-3}$).

c. Dominant terms in the vorticity tendency equation. Shaded areas indicate local positive vorticity tendencies.

H: horizontal advection term. T: tilting term.

V: vertical advection term.

C: convergence term.

+, -: indicate whether above mechanisms are increasing or decreasing vorticity at a given time and pressure level.

dominant terms in the vorticity tendency equation are also shown. One can see that vorticity first became positive in the lowest layers 24 to 36 hours prior to the "trigger" stage. The low level downward motion and vertical stretching forced convergence at low levels which produced the orographic vortex. Deep development occurred when this vertical stretching mechanism extended well into the atmosphere. The dynamic motions produced by the advancing upper wave, combined with the externally forced downward motion at low levels, and initiated rapid vorticity production at middle levels. The tendency of this effect alone would give net increases of $2. \times 10^{-5} \text{ sec}^{-1}$ for each 12 hour period averaged over a layer in the middle levels.

In LCD II the orographic period was shorter and the triggering stage not as evident. In LCD I it was the upward development of the vertical stretching mechanism which appeared to be the main generating feature of the cyclone. In LCD II the vertical motion was upward even at low-levels during the period of most rapid development. Thus the cyclogenesis in this case was more classical in a quasi-geostrophic sense in that the terrain-induced downward motion interacted with the upper-level dynamic vertical motion only for a very short period near 12 GMT on Feb 13.

Observational studies of Alpine lee cyclogenesis frequently show that a parent surface cyclone exists to the north of the mountains. This cyclone decreases in strength as the system to the south grows. To see the shift in emphasis from the northern to the lee storm, consider Figure IV-16 which illustrates the changes in vorticity, both north and south of the Alps.

The terms in the vorticity equation are not shown. However, during the period of rapid development in LCD I, the mechanisms contributing most to the increase of vorticity within the volume were: convergence and tilting

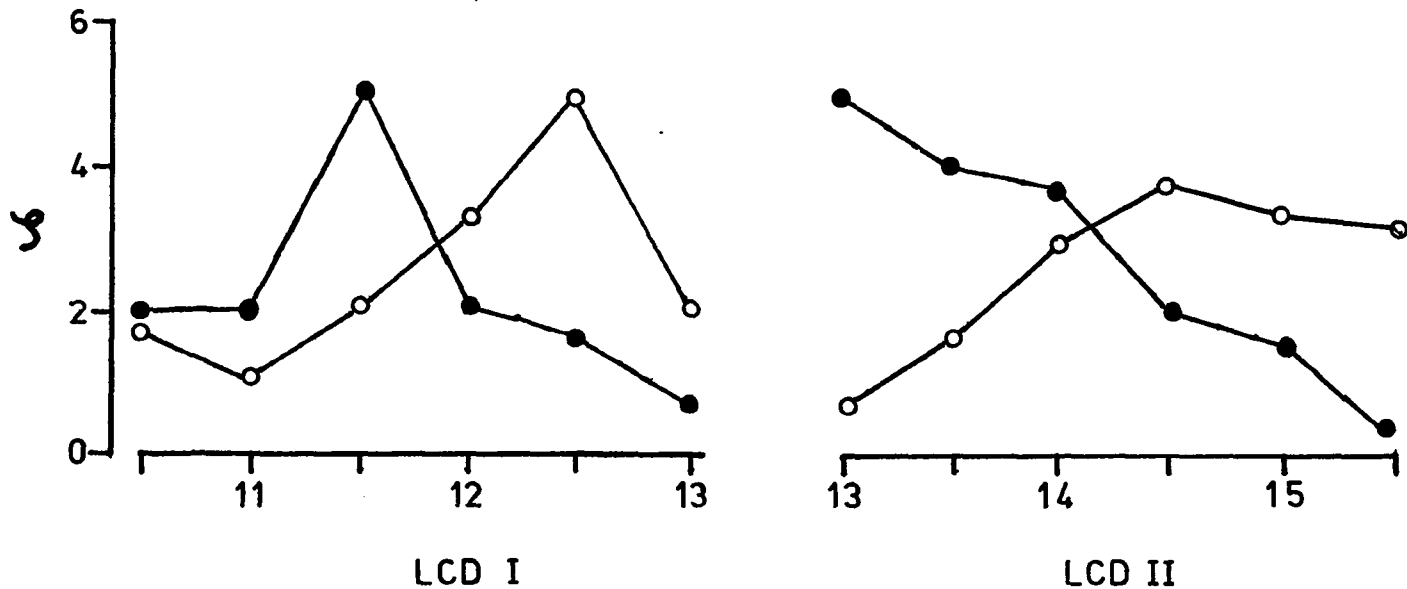


Fig. IV-16. Mean relative vorticity (ζ) within 500 km of surface cyclone, north and south of the Alps. Solid dots (\bullet) indicate disturbance north of the Alps; open dots show lee cyclone south of the Alps (\circ). Plots show shift in emphasis as lee cyclone develops.

at low levels; convergence (vertical stretching) at middle levels; and vertical advection at high levels. For LCD II during the rapid development period, dominant terms were convergence at low levels; vertical advection at middle levels; and horizontal convergence and vertical advection at high levels (both acting against the tilting term).

These observations and diagnostic calculations of vorticity support the previously cited studies concerning the two-stage nature of lee cyclogenesis. LCD I appears to be an example of a terrain enhanced cyclone. The upward extension of the vertical stretching mechanism was a critical element during development. Surging of the front over the mountain barrier further enhanced the stretching process. LCD II represents a cyclone somewhat enhanced by, but not critically linked to, the presence of the mountains.

Energy

The diagnosis of energy is accomplished in two ways. First we look at the bulk energy quantities within a moving volume; and second we compute the energy conversions necessary to account for the changes in the bulk amounts. The two methods, shown in Chapter III to calculate available potential energy, differed in that one was an approximation to the other. The Johnson method, Equation III-2, gave results 5 to 7 times larger than the more approximate Haltiner method. Since the Haltiner computation facilitates the decomposition into mean and perturbation terms, it was decided to use the ratio of APE' to \overline{APE} , to partition the available potential energy computed with Equation III-2.

Figures IV-17 and 18 show the mean and perturbation quantities for LCD I and II. Some features are immediately evident. The mean kinetic energy in the volume decreased with time. \overline{APE} also decreased with time but energetically was of small magnitude. APE' increased as the volume interacted with

the mountains. This was followed by increases of KE' which became maximum as the cyclone peaked in strength. The interaction among these quantities is shown in Figures IV-20 and 21. The energy conversion and transfer terms were computed from the quasi-geostrophic equations for energy transformation (Equation III-3) and the actual observed changes in energy seen in Figures IV-17 and 18. The conversions were averaged in time and assumed to extend over 12 hours. The differences between the computed and observed trends required adjustments (\rightsquigarrow) which represent unparameterized processes or errors. The direction of the energy conversion or transfer (\rightarrow) on Figures IV-20 and 21 represents the computed quasi-geostrophic trend.

The plots in Figure IV-17 and 18 show the imbalance in the total energy, which may be due to sources of energy such as radiation, latent heat, boundary flux errors, or errors in parameterization of frictional dissipation. Estimates of friction are shown on both figures. The limited rainfall data indicated that rain was produced over Italy from 12 GMT of the 14th to the end of the data period. The source of latent heat should influence the residual during this time and the total energy plot on Figure IV-18 indeed shows that a source was most likely active. This can be explored qualitatively by looking at a cross section of the efficiency factor, ϵ , in the region at this time. Figure IV-19 shows ϵ through the volume for 00 GMT Feb 15. Precipitation occurring in the regions of cloud cover would be producing a net increase in APE, thus accounting for the apparent source in Figure IV-18. Unfortunately, without full coverage of precipitation amounts, the impact cannot be evaluated quantitatively. Sources and sinks on Figure IV-17 cannot be readily explained since it appeared that precipitation did not occur.

On Figure IV-20 and 21 energy transformations are given for the

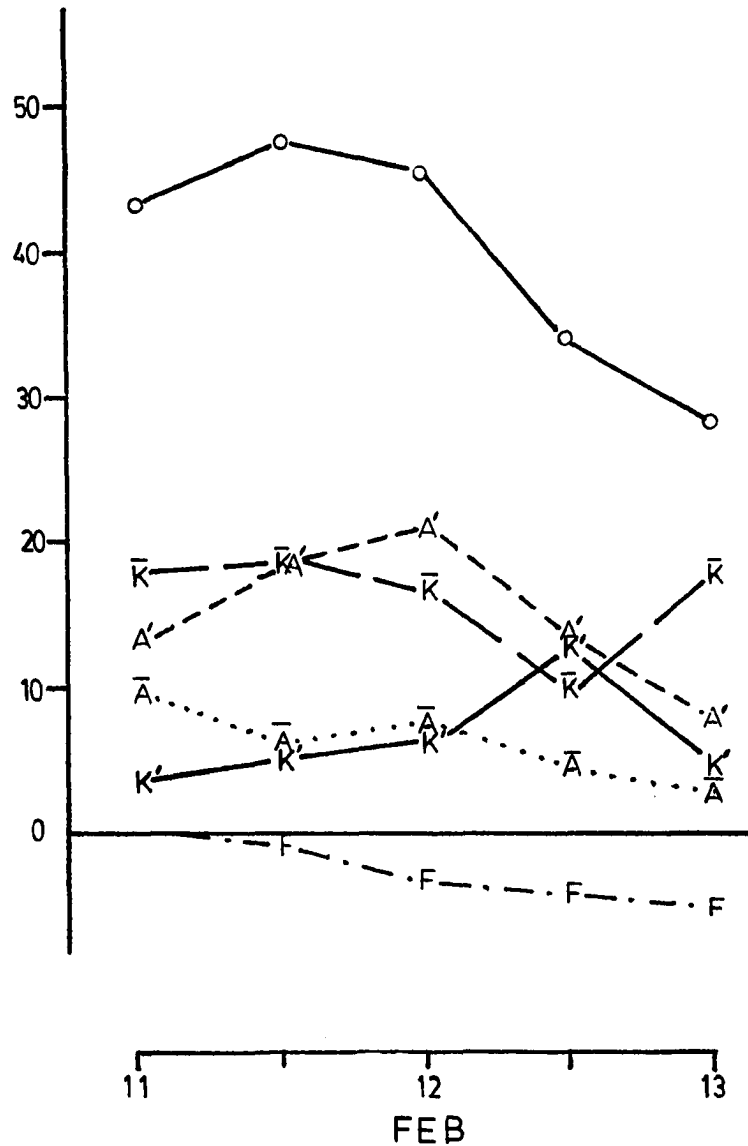


Fig. IV-17. Bulk energy quantities ($\text{Joules/m}^2 \times 10^5$) within the quasi-Lagrangian volumes for LCD I (see fig. IV-7), plotted as a function of time. K is kinetic energy; A is available potential energy; and ()' and () refer to perturbation and volume mean, respectively. F is the cumulative frictional sink, and the open circles show the total energy, (the sum of A', K', \bar{A} , \bar{K} , and F.)

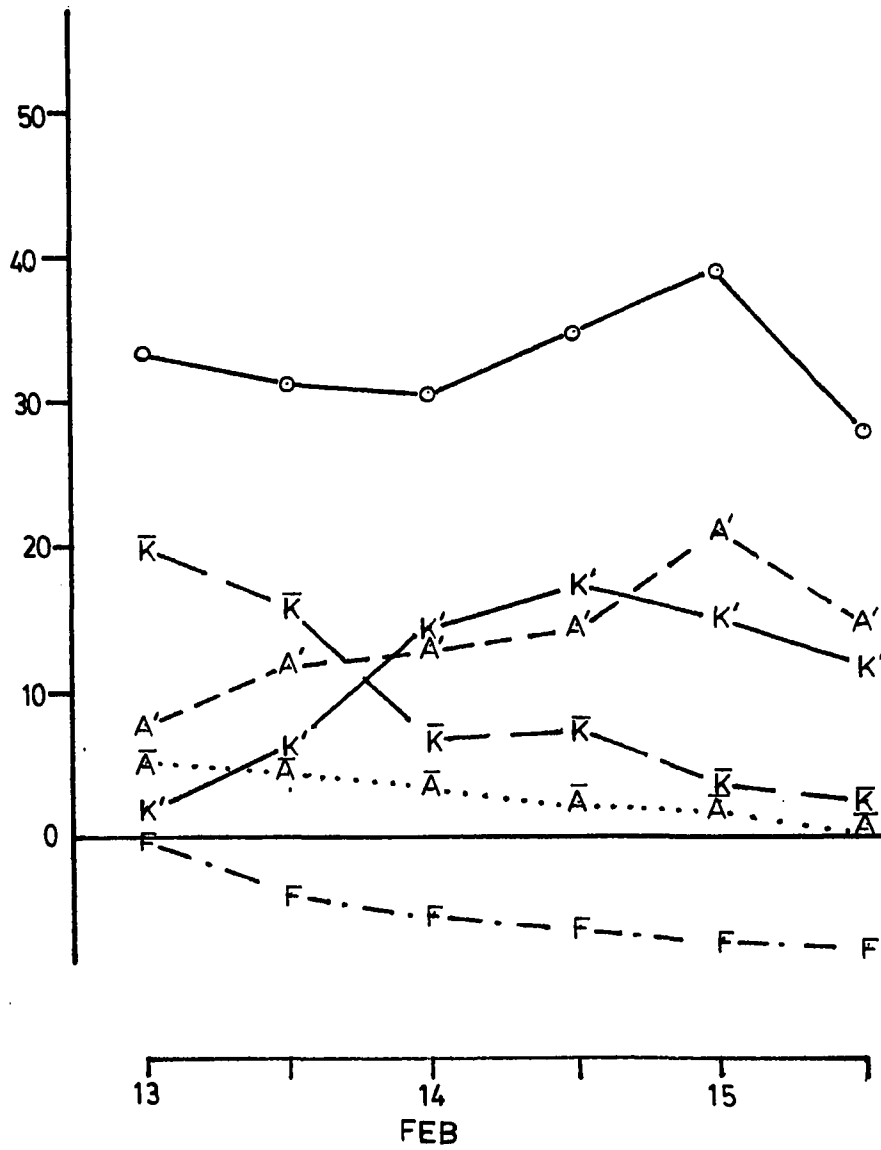


Fig. IV-18. Bulk energy quantities for LCD II. For explanation of symbols see fig. IV-17.

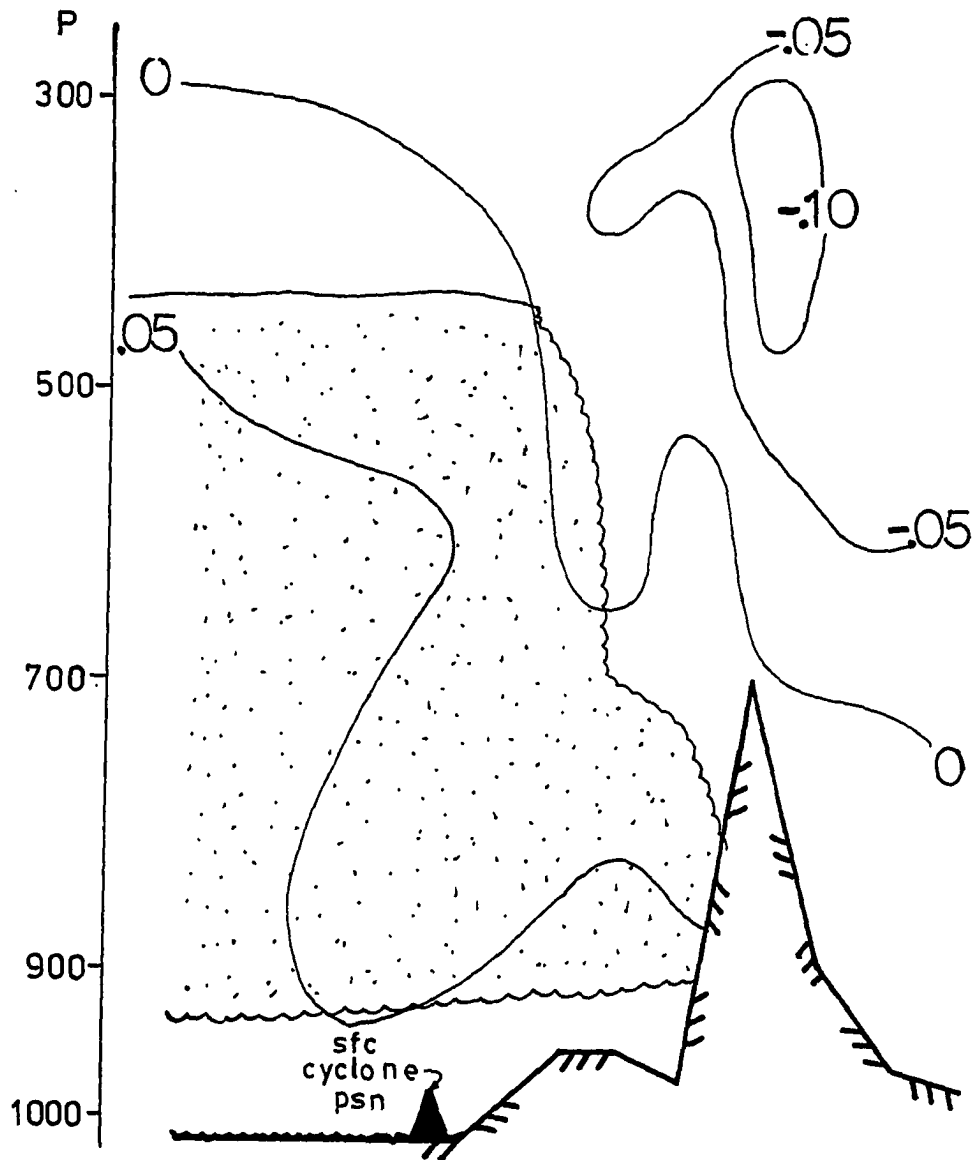


Fig. IV-19. Cross section of the efficiency factor (ϵ), clouds, and terrain northeast of the surface cyclone on 15 Feb. 00 GMT. Clouds are estimated from satellite imagery.

processes defined by the equation set III-3. Transformations which cannot be explained are indicated, and may be considered to be due to non-geostrophic processes or errors. There are some interesting conclusions one may draw from both the consistent and inconsistent estimates of the energy transformation processes. One that stands out immediately is the transition of \bar{K} to K' . This is opposite to the usual atmospheric energy cycle (Figure III-4). This process is consistent with the findings earlier in this chapter, namely that vertical stretching, which is produced externally, converts earth or large scale vorticity into disturbance vorticity. In the same way, particularly when the lee cyclone was undergoing intensification, mean kinetic energy was converted to disturbance KE. This process was playing as large a role as the typical conversion in which APE' goes to K' during baroclinic development. The energy transfer ($K \rightarrow K'$) is the barotropic contribution to development; while ($A' \rightarrow K'$) is the baroclinic contribution.

Another feature of the kinetic energy budget is the possible underestimation of kinetic energy dissipation by mountain induced friction. Toward the time periods when the disturbance had reached maximum intensity and was decreasing in strength there are large implied sinks of kinetic energy.

A mysterious source of APE appears in both cases from about 24 hours before the cyclone reached maximum intensity in the lee. This is about the time the volume was interacting with the mountains. From the calculations of frontogenesis we can estimate the amount of APE that was produced in the volume by primarily the mean flow components interacting with the mountain. They are shown in Table IV-2. These calculations are based on departures of frontal strength over and above the mean thermal gradient.

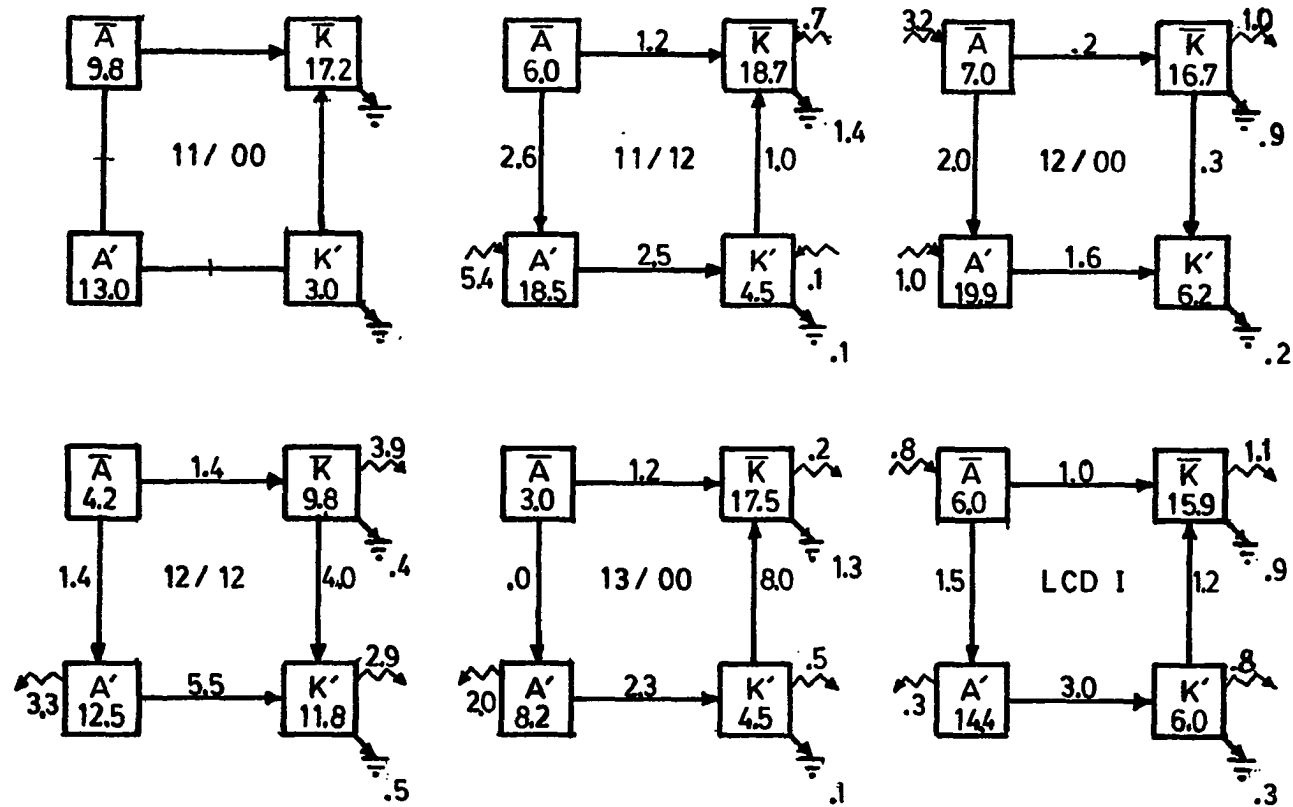


Fig. IV-20. Bulk energetics and transformations within moving volumes for date and time indicated. Energy quantities within boxes are in $\text{Joules}/\text{m}^2 \times 10^5$. Arrows (\longrightarrow) indicate quasi-geostrophic redistribution processes time averaged in $\text{J}/\text{m}^2 \times 10^5$ per 12 hours. Frictional dissipation is given similarly. Diagram on lower right shows the time average for the entire cyclone episode. Arrows (\rightsquigarrow) show energy processes required to balance energy budget. These are related to non-geostrophic or diabatic mechanisms (radiation and latent heat), errors in boundary flux or parameterization of frictional dissipation.

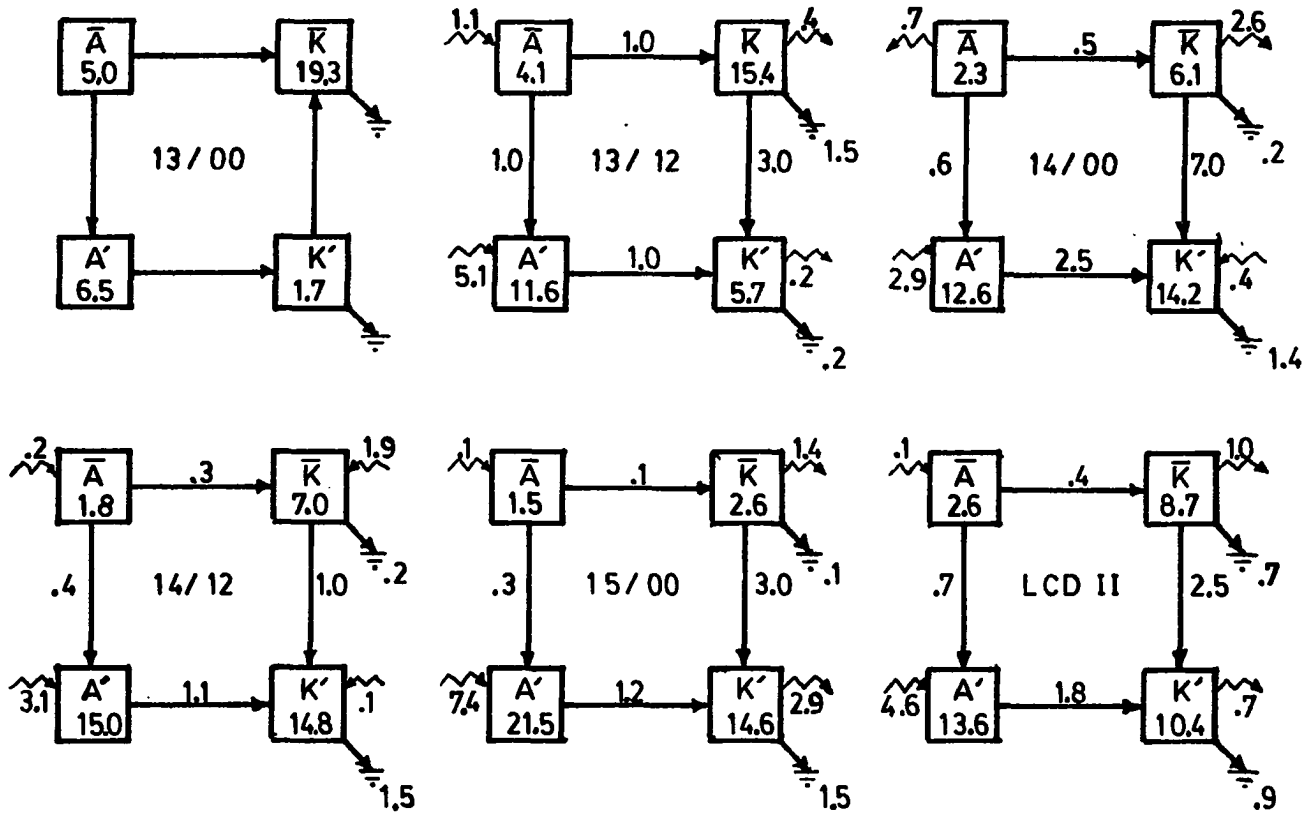


Fig. IV-21. Bulk energy and energy transformation for LCD II. Symbols and figures are explained in caption for IV-20.

Table IV-2

FRONTOGENESIS AND PRODUCTION OF APE			
Period	Mean frontogenesis (deg/1000km/24hr)	Estimate of APE ¹ Production by frontogenesis (J/m ² /24hr x 10 ⁵)	Observed change in APE ¹ (J/m ² /24hr x 10 ⁵)
11/00 - 12/00 GMT	+4.63	+6.74	+8.21
13/00 - 14/00 GMT	+3.62	+4.77	+4.05

The implication is that a link may be established between \overline{KE} and APE' . On reexamination of the conditions during the frontogenetic phase, we find that the mean flow is strong and northwesterly. This flow impinged on the mountain producing the vertical motion couplets which induced the tilting process. The mean flow was also horizontally disturbed and we should expect to see a $\overline{KE} \rightarrow KE'$ conversion as we indeed do. The tilting mechanism would appear to be the conversion link between the mean flow kinetic energy \overline{KE} , and perturbation potential energy, APE' . Unfortunately this should be seen in the $KE' \rightarrow APE'$ conversion, which upon examination is actually in the other direction. It would appear the parameterized energy transformations are inadequate to explain the observed changes in APE' . Use of more complex energy conversion equations derived from more complete forms of the vorticity equation may provide for conversions of this type.

Baroclinicity and the Scale of the Lee Cyclone

The time scale for a typical cyclone in middle latitudes is about 4 days (Holton, 1972). This appears to be much longer than one of our cases of lee cyclone development. As Buzzi and Tibaldi (1978) point out, there are major alterations in the structure and scale of these storms. Figure IV-22 shows the estimated change of scale of the lee cyclone as it passed from the orographic to the quasi-geostrophic scale. This measurement was based on the wavelength distance between positive and negative vorticity centers. The initial perturbation was quite small, well below the estimated "critical wavelength" suitable for conventional baroclinic instability to dominate, allowing the perturbation to grow.

There is a certain class of baroclinic instabilities which operate at scales well below the critical wavelength. As shown by Stone (1966),

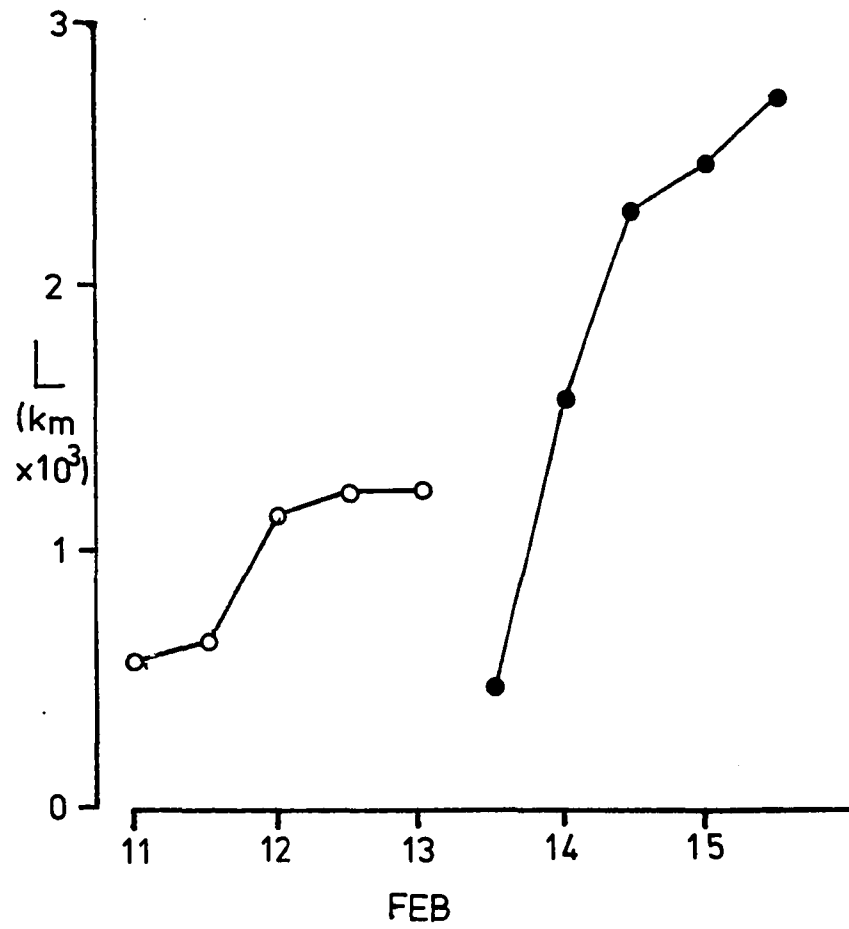
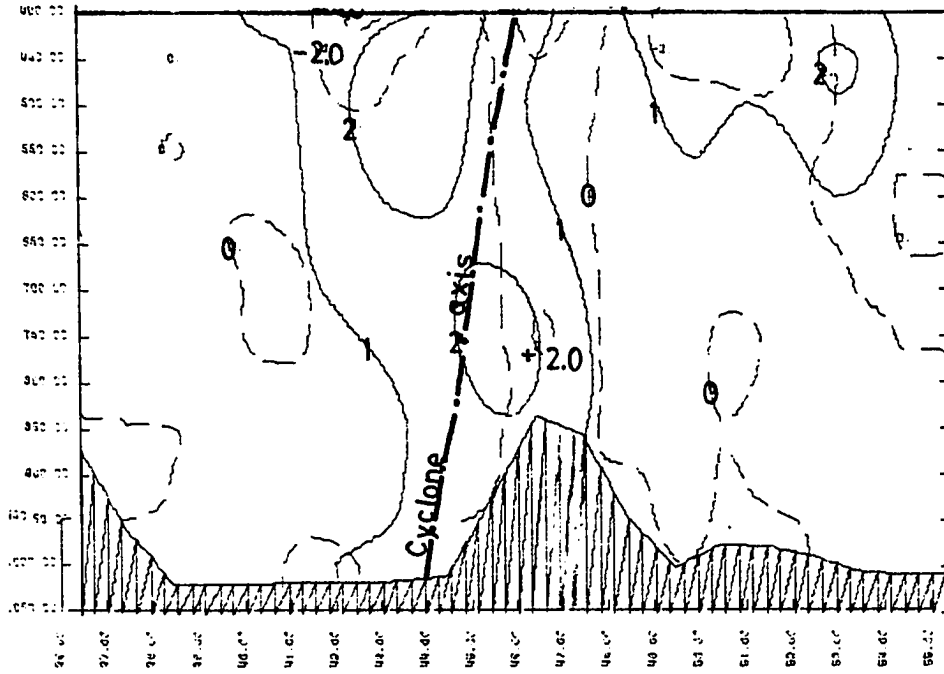


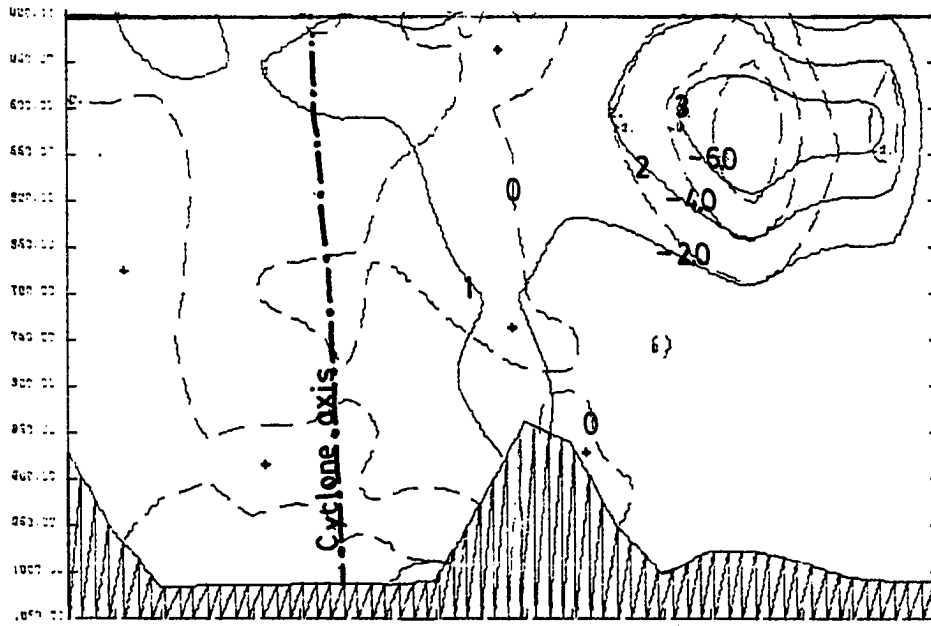
Fig IV-22. Scale of lee cyclone versus time, for LCD I (—○—) and II (—●—). These are estimated from geopotential and vorticity fields.

Tokioka (1970), and Emanuel (1979), these environments are characterized by Richardson Numbers ($Ri = \frac{g\partial\theta}{\partial z} \left(\frac{\partial|\vec{v}|}{\partial z}\right)^{-2}$) of about 1 or less (actually $Ri < \frac{\zeta+f}{f}$), in which small wave growth can dominate. Checking the Richardson Numbers in the lee region during development in both cases showed values from 10 to 20. Buzzi and Tibaldi (1978), showed that even in its initial state, the lee cyclone may be too large for the symmetric instability growth rates to dominate the conventional baroclinic process.

As clearly revealed in the analysis, the Alps significantly alter the airflow and thermal fields. During the explosive development stage, strong vertical stretching occurs which is primarily due to the externally forced motions combined with dynamics of the approaching wave. Thus, the barotropic mechanisms which initiate the lee cyclone, and the baroclinic processes which move into the region, combine to overcome the baroclinic stability of the initial wave. By the time thermal advection enters the picture the storm is no longer a weak perturbation on which stability theory is based. The wave may move away from the lee region and die as often seen in the Great Plains of the United States and Canada. However, the storm may increase its horizontal scale and survive. The transition stage, when the storm must pass from a terrain assisted baroclinic/barotropic system, to one which must survive baroclinically over flat terrain, is critical to its eventual evolution. We saw the case of a dying cyclone in LCD I. The cyclone in case I outran its source of externally forced motion and baroclinicity, as shown in Figure IV-23. In LCD II the slow moving system which was associated with a larger parent wave, seemed to profit by its association with the Alps. The cyclone remained near the source of baroclinicity and vertical motion. The suspected effects of latent heat may have maintained the storm for the 3



FEB 12, 1976 00 GMT LON 352 DEG



FEB 12, 1976 12 GMT LON 352 DEG

Fig. IV-23. Frontal strength (—) [deg/100km], and frontogenetic rate (---) [deg/1000km-sec x 10⁻⁴] for LCD I. Note how lower portion of baroclinic zone is first retarded by blocking effects, then becomes fixed to mountain. The cyclone moves away from this zone with time and dies.

days it remained in the area. Latent heating produces amplification of vorticity by diabatically forcing vertical motions. As shown, this is supported by generated perturbation available potential energy. The cyclones that develop in the lee of the Rockies and become long lived, usually require input of latent heat (Phillips, 1979).

Storm development is significantly influenced by the Alps. This influence can be resolved by conventional data sources. Surely, mechanisms operating at unresolvable scales are influencing the course of development. Many of the quantities which we have derived, have great potential for error. However, the qualitative relationships among independently derived functions like energetics, vorticity, and frontal strength are in essential agreement leading support to the observations on which we commented. Experiments designed exclusively for measuring mountain-cyclone interaction are in the planning stage (ALPEX).

CHAPTER V

Summary

The study undertaken is admittedly broad in scope. Many new techniques were used in the primary data analysis. Evaluating elements of cyclogenesis from many perspectives was a major task meeting with frustration owing to the limited information available from the data. Ideally, observations at three or six hour intervals would be required to perform a detailed and fully quantitative analysis of a phenomenon with a time scale of 12-24 hours. In both space and time we tried to resolve processes near the limits of resolution. This resulted in evaluations of processes which are necessarily diminished by the response of the analyses. Still, the Alps produce effects which can be measured within a large scale or quasi-geostrophic framework and we have proceeded on this basis, supported by the previous studies in this region.

The two case studies considered illustrate two different lee cyclones. The first case, LCD I, was a storm for which the Alps appear to have been the major cause of cyclogenesis. The cyclone in LCD II was associated with a larger upper wave, and most likely would have developed with or without the mountain effect. However, certain aspects (and eventual position) of the stationary surface cyclone were more than likely influenced by the forced lifting and positioning of the frontal zone near the mountain.

The findings of this study are summarized on the following page.

Stages of Development

The Alps significantly enhance cyclogenetic processes in their vicinity. In this study the cyclones seemed to pass through a series of steps during their lifetimes:

1. Orographic stage: Flow normal to the mountain produces small shallow cyclones maintained by low level vertical stretching in the downslope region.
2. Frontal stage: The frontal zone interacts with the mountain and strengthens through tilting and horizontal deformation. This process increases the available potential energy on the perturbation scale.
3. Explosive or "trigger" stage: The intensity of the lee cyclone increases rapidly as terrain-forced vertical motion and dynamically produced upward motion are superimposed. This results in strong convergence at middle levels and consequent vorticity production. The disturbance at this stage is vertically stacked and has a barotropic character at low to mid-levels.
4. Transition stage: The influence of the strong mid-level circulation from stage 3 and the increased frontal zone strength from stage 2 allows the storm to take on a baroclinic structure. Whether the development continues depends on the scale of the parent wave, the strength of the front and the advecting circulation. The storm moves away from the mountain.
5. Mature stage: The lee cyclone is "on its own" and must maintain itself by thermal advection and quasi-geostrophic secondary circulations. The more persistent cyclones normally include the effects of latent heating in the energy budget.

Table V-1 further describes the five development stages. Symbols used have been explained in the text or in Appendix 7. Figure V-1 illustrates schematically the development of an Alps cyclone, summarized from the case studies.

Conclusions and Recommendations

Certain findings of the diagnosis were important and should be reviewed.

The rapid development phase appeared to be a complex interaction of barotropic and baroclinic processes. The signals calculated from the quasi-geostrophic energy terms verified both barotropic and baroclinic mechanisms in increasing the perturbation kinetic energy. In the lee of the Alps strong vertical stretching was indicated with consequent vorticity production through the column. Large imbalances in the energy budget and rapid increase of cyclone scale during the 12 hour period strongly suggest that processes at mesoscale (i.e. related to the transverse scale of the Alps, 200-300 km) or smaller may be playing important roles. For further definition of this phenomenon observations must be increased in both space and time. A minimum requirement would be to sample the upper air at three-hour intervals and supplement the existing network with observations in the Alps and over the Gulf of Genoa.

The systematic increase in intensity of the baroclinic zone is another feature which has not been examined quantitatively in other papers. It was determined that orographically forced tilting was the most important mechanism in this process.

Table V-1.
Stages of Lee Cyclone Development

Stage of Development	Primary Energy Process	Primary Vorticity Production Process	Remarks
Orographic	1. $\bar{K} \rightarrow K'$	1. Low level vertical stretching	1. Barotropically derived lee trough (potential vorticity).
Frontogenetic	1. $\bar{A} \rightarrow A'$ 2. undiagnosed source of A' (perhaps $\bar{K} \rightarrow A'$)	1. Vertical stretching in low levels. 2. Tilting term important in lower levels.	1. Frontogenesis by deformation and tilting near mountain. 2. This phenomena seen in other diagnostic studies and numerical simulations.
Rapid Growth	1. $\bar{K} \rightarrow K'$ 2. $A' \rightarrow K'$	1. Positive vorticity at upper levels. 2. Strong vertical stretching at mid levels (convergence). 3. Tilting and weak convergence at low levels.	1. Barotropic/baroclinic hybrid 2. Petterssen's Type B cyclogenesis. 3. Buzzi and Tibaldi's "trigger" stage. 4. Frontal zone aloft moves over lee region. Low level front retarded.
Transition	1. $A' \rightarrow K'$	1. Low level horizontal convergence. 2. Upper level divergence.	1. Upward vertical motions extend nearly to surface. 2. Cyclone moves from mountain, increases scale. 3. Cyclone takes on a more baroclinic character although appears well advanced into occlusion.
Mature	1. $R_d^1 \rightarrow A'$ 2. $A' \rightarrow K'$	1. Mid level vertical motion from diabatic forcing produces convergence at low levels.	1. Occluded cyclone maintained by latent heat release
...and/or.....and/or.....and/or.....and/or.....
Dissipation	1. $K' \rightarrow F'$ 2. $K' \rightarrow \bar{K}$	2. Flux divergence of vorticity out of cyclone.	2. Dissipation by frictionally induced spin down.

Note: R_d are diabatic contributions to A (in this case suspected latent heating).

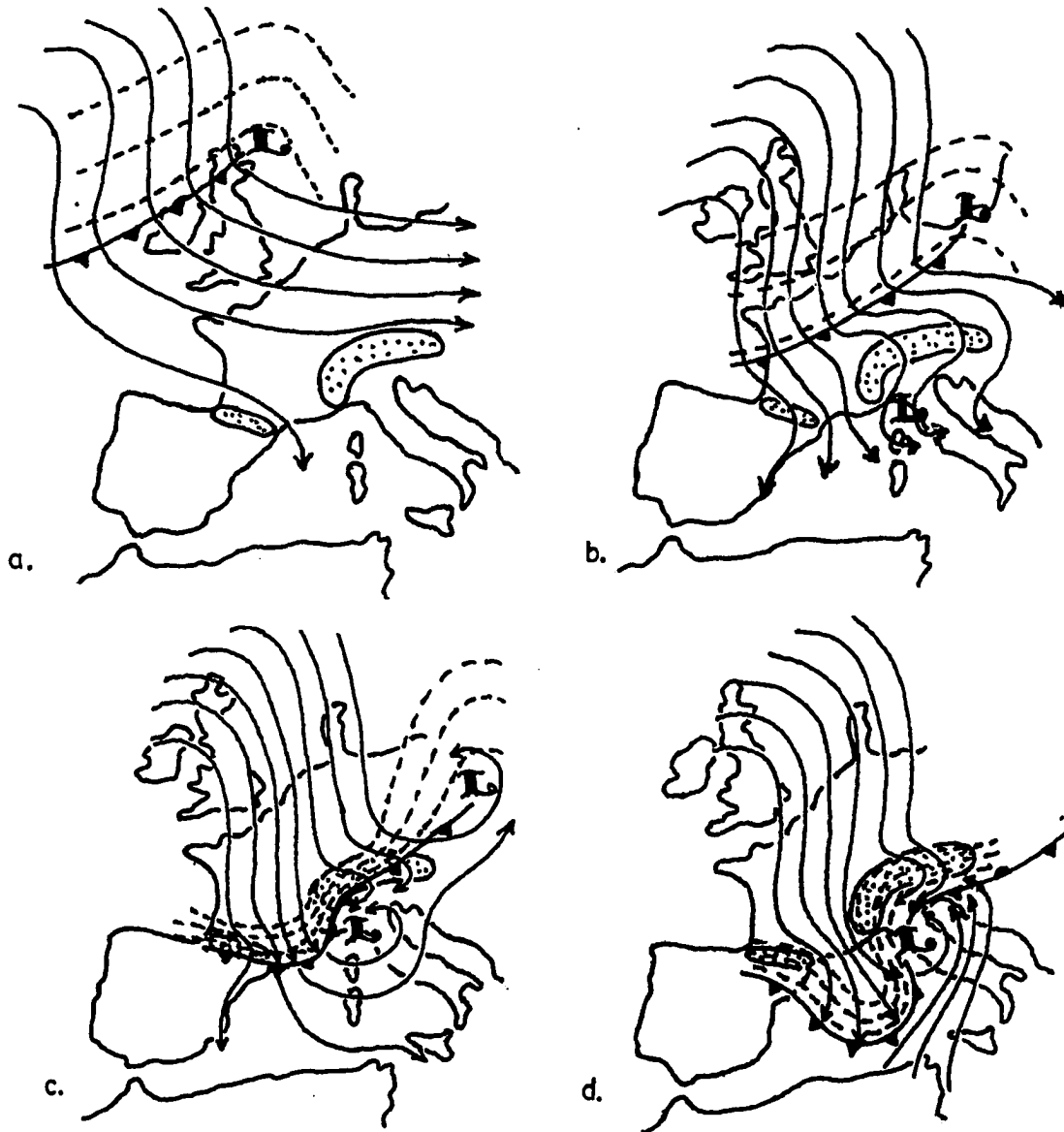


Figure V-1 Development cycle for a Genoa cyclone. Streamlines given for 700 mb (~3000m) flow (\rightarrow); 700 mb front (\dashrightarrow); 700 mb low (\bullet); 700 mb isotherms (-----); significant terrain (shaded). a. Initial phase - High pressure ridge builds over E. Atlantic; disturbance with front moves southeast. b. Barotropic phase - Strong mean flow interacts with terrain; incipient Genoa cyclone develops in lee. c. Frontogenetic/Transition stage - Frontal zone intensifies over mountain barrier; cyclone begins transition as thermal advection increases rapidly. d. Baroclinic stage - Strong vertical motion in cyclone converts available potential energy to kinetic energy. Cyclone is now fully baroclinic, developing rapidly, and is producing organized clouds and heavy rain.

In the analysis scheme we selected weighting factors based on consideration of scale, availability of data, relative quality of data, and nature of the imposed dynamical relation. A meteorologists subjective evaluation of the analyses showed that the structure and evolution of systems were well defined. Definition of features at the smallest resolvable scales was reasonable and little noise was evident. The computation of vertical motion used a new approach to combine independent estimates of omega. The ability to control the vertical penetration of orographically forced flow is attractive and could be applied in other problems. Comparison between vertical (upward) motion and observed clouds showed good correspondence. Although the used of satellite data in a diagnostic scheme can be a somewhat risky proposition, the technique designed in this paper allowed this data to make a positive contribution to the description of atmospheric structure at certain data times, particularly over the Mediterranean. Equally important but not as obvious was that the inclusion of satellite data did not add structure to the analysis where there was obviously none.

BIBLIOGRAPHY

- Achtemeier, G.L., 1975: On the initialization problem: a variational adjustment problem. Mon. Wea. Rev., 103, 1089-1103
- Barnes, S.L., 1973: Mesoscale objective map analysis using weighted time series observations. NOAA Tech. Memo. ERL-NSSL-62, National Severe Storms Lab., Norman, OK, 60 pp.
- Baxter, T., 1975: Pattern conserving technique. Tech. Memo., Ocean Data Systems, Inc.
- Bleck, R., 1977: Numerical simulation of lee cyclogenesis in the Gulf of Genoa. Mon. Wea. Rev., 105, 428-445.
- Bloom, S.C., 1980: The objective analysis of prestorm mesoscale rawinsonde data through the imposition of dynamical constraints. Ph.D. dissertation, University of Illinois 109 pp.
- Buzzi, A., and S. Tibaldi, 1977: Inertial and frictional effects of rotating and stratified flow over topography. Quart. J. Roy. Meteor. Soc., 103, 135-150.
- _____, 1978: Cyclogenesis in the lee of the Alps: a case study. Quart. J. Roy. Meteor. Soc., 104, 271-287.
- Dickerson, M., 1978: MASCON-A mass consistent atmospheric flux model for regions with complex terrain. J. Appl. Meteor., 17, 241-253.
- Doswell, C., 1976: The use of filtered surface data to reveal subsynoptic scale dynamics. Ph.D. dissertation, University of Oklahoma 126 pp.
- Dutton, J.A. and D.R. Johnson, 1976: The theory of available potential energy and a variational approach to atmospheric energetics. Advances in Geophysics, 12, 333-436.
- Eady, E.T., 1949: Long waves and cyclone waves. Tellus, 1, 33-52.
- Edmon, H., 1978: A reexamination of limited-area available potential energy budget equations. J. Atmos. Sci., 35, 1655-1659
- Emanuel, K.A., 1979: Inertial instability and mesoscale convective systems. Part I: linear theory of inertial instability in rotating viscous fluids. J. Atmos. Sci., 36, 2425-2449.

- Fritsch, J., 1971: Objective analysis of a two dimensional data field by the cubic spline technique. Mon. Wea. Rev., 99, 179-186.
- Gandin, L.S., 1963: Objective Analysis of Meteorological Fields, National Tech. Inf. Service publication TT-65-50007. Springfield, VA 242 pp.
- Godske, C.L., T. Bergeron, J. Bjerknes, R. Bungeard, 1957: Dynamic Meteorology and Weather Forecasting, Amer. Meteor. Soc., Boston, MA 670 pp.
- Gutman, L.N., 1969: Vedeneye v Nelineanuyu Teoriyu Mesometeorologicheskikh Protssosov, Hydrodynamical Inst., Leningrad, USSR, 295 pp.
- Hage, K.D., 1961: On summer cyclogenesis in the lee of the Rocky Mountains, Bull. Amer. Meteor. Soc., 42, 20-33.
- Halem, M., M. Ghil, R. Atlas, J. Suskind, W. Quick, 1978: The GISS sounding temperature impact test. NASA, Tech. Memo. 78063, NASA Goddard Space Flight Center, Greenbelt, Md., 368 pp.
- Haltiner, G., 1971: Numerical Weather Prediction. John Wiley and Sons, New York, 317 pp.
- Hess, S.L., 1959: Introduction to Theoretical Meteorology. Holt, Rinehart and Winston, New York, 362 pp.
- Hillger and Vonder Haar, 1977: Deriving mesoscale temperature and moisture information from satellite radiance measurements over the United States, J. Appl. Meteor., 16, 715-726.
- _____, 1979: An analysis of satellite infrared soundings at the mesoscale using statistical structure and correlation functions, J. Atmos. Sci., 36, 287-305.
- Holton, J., 1972: An Introduction to Dynamic Meteorology. Academic Press, New York, 319 pp.
- Hoskins, B. and F. Bretherton, 1972: Atmospheric frontogenesis models: mathematical formulation and solution. J. Atmos. Sci., 29, 11-37.
- _____, and N. West, 1979: Baroclinic waves and frontogenesis Part II: uniform potential vorticity jet flows-cold and warm fronts. J. Atmos. Sci., 36, 1663-1680
- Hylton, D., 1972: The application of low pass and band pass filtering techniques to surface and upper air fields. M.S. Thesis, University of Oklahoma, 79 pp.
- Jenkins, G.M. and D.G. Watts, 1968: Spectral analysis and its applications. Holden-Day, Inc., San Francisco, CA, 524 pp.

- Johnson, D.R., 1970: The available potential energy of storms. J. Atmos. Sci., 27, 727-741.
- _____, C.H. Wash, and R.A. Petersen, 1976: The mass and angular momentum budgets of the Alberta cyclone of 30 March - 2 April 1971. Preprints, Sixth Conference on Weather Forecasting and Analysis, Albany, New York, Amer. Meteor. Soc., 350-356.
- Kessinger C. and H. Bluestein, 1979: The role of deformation at the dryline front intersection, Preprints, 11th Conference on Severe Local Storms Kansas City, MO, Am. Meteor. Soc., 91-95.
- LaSuer N., 1974: Subsynoptic extratropical weather systems: observation, analysis, modeling and prediction colloquim, National Center for Atmospheric Research, Boulder, CO, Col. I 213 pp.
- McClain, E.O., 1960: Some effects of the western cordillera of North America on cyclonic activity. J. Meteor., 17, 104-115.
- McGinley, J., 1973: Environmental energy fields associated with severe storms, M.S. Thesis, Univ. of Oklahoma 130 pp.
- _____, 1979: Use of satellite temperature in a dynamical analysis scheme. Preprints, 11th Conference on Severe Local Storms, Kansas City, MO. Amer. Meteor. Soc., 15-19.
- Merkine, L., 1975: Steady finite amplitude flow over long topography in a rotating stratified atmosphere. J. Atmos.Sci., 32, 1881-1893
- _____, and E. Kalnay-Rivas, 1976: Rotating stratified flow over finite isolated topography, J. Atmos. Sci., 33, 908-922.
- Miller, J.E., 1948: On the concept of frontogenesis. J. Meteor., 5, 169-171.
- Morel, P., 1973: Dynamic Meteorology. edited by P. Morel, D. Reidel Pub. Co., Boston, 622 pp (Chpt. by J.P. Charney)
- Oort, A.H., 1964: On estimates of the atmospheric energy cycle. Mon. Wea. Rev., 92, 483-493.
- Petterssen, S., 1956: Weather Analysis and Forecasting. 2nd ed., Vol. 1, McGraw-Hill, New York, Chapters 2 and 11.
- _____, and S.J. Smebye, 1971: On the development of extratropical cyclones Quart. J. Roy. Meteor. Soc., 97, 457-482.
- Phillips, G., 1979: On the development of an Alberta cyclone. M.S. Thesis, Univ. of Oklahoma, 74 pp.
- Sasaki, Y., 1958: Objective analysis based on the variational method. J. Meteor. Soc. Japan, 36, 77-88.

- Saskai, 1969: Proposed inclusion of time variation terms, observational and theoretical, in numerical variational objective analysis. J. Meteor. Soc. Japan, 47, 115-124.
- _____, 1970: Some basic formalisms in numerical variational analysis. Mon. Wea. Rev., 98, 875-883.
- _____, J.A. McGinley, and T.L. Baxter, 1977: Final report of contract no. N0028-76-C-3160, Naval Environmental Prediction Research Facility, Monterey, California, 79 pp.
- _____, and J.A. McGinley, 1978: Dynamical analysis of Mediterranean cyclones. Naval Environmental Prediction Research Facility Technical Report, Monterey, California, 45 pp.
- Sherman, C., 1978: A mass consistent model for wind fields over complex terrain, J. Appl. Meteor., 17, 312-379.
- Smith, P., and C. Ping Lin, 1978: A comparison of synoptic scale vertical motions computed by the kinematic method and two forms of the omega equation. Mon. Wea. Rev., 106, 1687-1694.
- Stephens, J.J., 1971: On definable scale reduction by simultaneous observations. J. Appl. Meteor., 10, 23-25.
- Stone, P., 1966: On non-geostrophic baroclinic instability. J. Atmos. Sci., 27, 390-400.
- Tibaldi, S., A. Buzzi and P. Malguzzi, 1980: Orographically induced cyclogenesis: analysis of numerical experiments. Mon. Wea. Rev., 108, 1302-1314.
- Tokioka, T., 1970: Non-geostrophic and non-hydrostatic stability of a baroclinic fluid. J. Meteor. Soc. Japan, 48, 503-520.
- Trevisan, A., 1976: Numerical experiments on the influence of orography on cyclone formation with an isentropic equation model. J. Atmos. Sci., 33; 768-780.
- Trewartha, G.T., 1965: An Introduction to Climate, McGraw-Hill, New York, 403 pp.
- Wagner, K. 1971: Variational analysis using observational and low-pass filtering constraints. M.S. Thesis, Univ. of Oklahoma, 39 pp.
- Wahba, G and J. Wendelberger, 1980: Some new mathematical-methods for variational objective analysis using splines and cross validation. Mon. Wea. Rev., 108, 1122-1143.
- Wei, M., 1979: The energy budgets of a developing cyclone over the east China Sea during the 1975 air mass transformation experiment. Ph.D. dissertation, Univ. of Oklahoma, Norman, 136 pp.

APPENDIX 1

Assimilation of Satellite Data

Satellite Data

The vertical sounders on satellites measured the radiance return of known narrow frequency bands in the infrared range, from 4 μm to 15 μm . At each of the wavelengths, carbon dioxide has a known atmospheric transmittance (τ_i), which has an inflection point at a discrete atmospheric pressure, (Fig. A-1-1). The clear column radiance for band i is given by,

$$R_{ai} = \epsilon_s B(\nu_i, T_s) \tau(\nu_i, P_s) + \int_{\ln p_0}^{\ln p} B(\nu_i, T(p)) \frac{d\tau_i}{d \ln p} d (\ln) p,$$

where B is the Planck black body radiation at sounding frequency ν ; and temperature T . T_s is the surface temperature; ϵ_s is the emissivity of the surface, and P_s the surface pressure.

Since $\frac{d\tau}{d \ln p}$ is known and the surface temperature can be directly estimated from independent microwave data or climatology, the equation takes the form of an integral equation and $T(p)$ is solvable by inversion techniques.

$\frac{d\tau}{d \ln p}$ becomes the weight function or kernel. Each channel measures mean temperature for a layer according to Figure A-1-1. Much detailed information is smoothed by this process, accounting for the large RMS departures from the "true" atmosphere (defined by coincident rawinsonde observations). It should be noted that radiance data is generally processed over oceans, since over land there is ambiguity in the value of surface emissivity, ϵ_s .

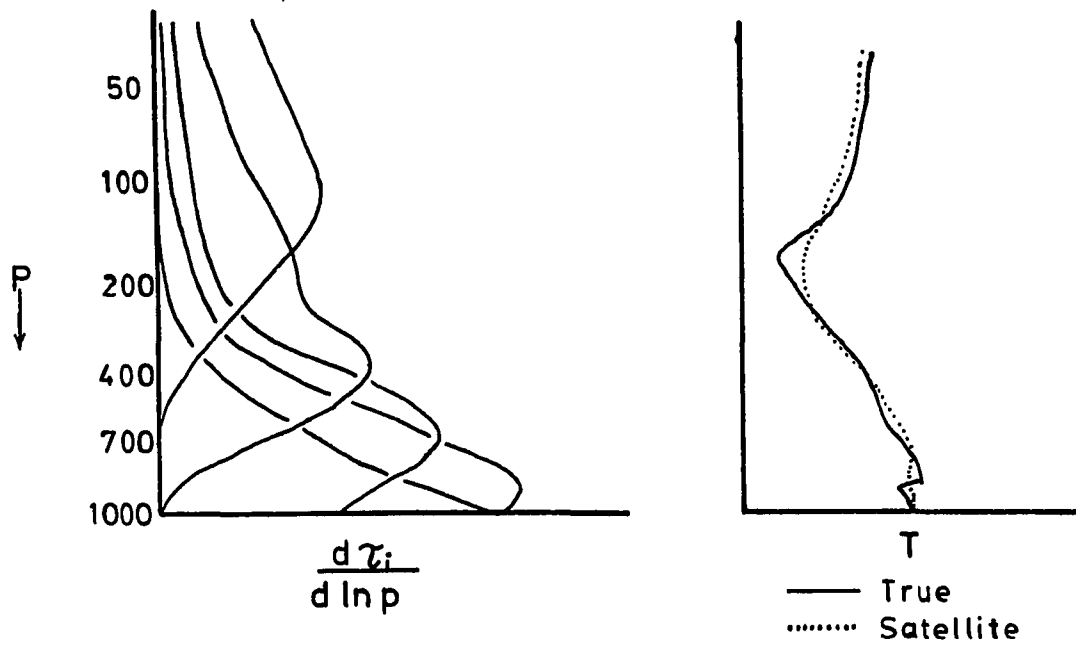


Fig. A-1-1. Weighting functions for a typical five channel radiance sensor. Note how the resulting temperature profile on left, loses detail.

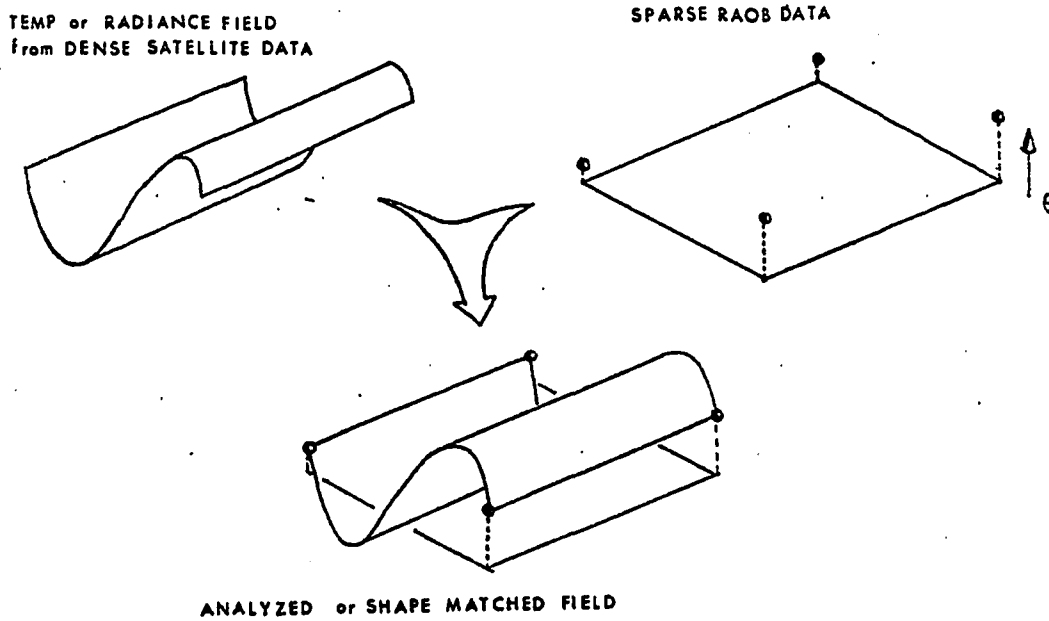


Fig. A-1-2. Schematic illustrating the shape matching technique.

Moisture data from satellites is obtained by measuring a band near $18\mu\text{m}$. This band indicates total precipitable water in the column, and when available can be used to assist in moisture analysis. A technique developed by Hillger and Vonder Haar (1977) computes a difference between observed radiance in the $18\mu\text{m}$ band and that radiance at $18\mu\text{m}$ associated with the temperature profile derived from the other channels. The residual is then related to moisture content.

Use of Satellite Observations During Assimilation of Data

The large inaccuracies in the magnitude of temperature are generally areally biased allowing us to exploit the definition of field structure provided by the radiance data, (Figure A-1-2).

Using the formalism (Equation II-2) outlined in Chapter II and expanded in Appendix 3, tests were run with simulated dense satellite data combined with widely scattered RAOB observations. This was done by introducing a known meteorological signal which was sampled by simulated SATOB's and RAOB's. Figure A-1-3 shows the RMS error in the resulting analysis for varying densities of RAOB data. The three curves show how the RMS error varies for: a) RAOB's only ($\alpha_S=0, \gamma_{1,2}=0$); b) Raw RAOB and SATOB temperatures combined ($\alpha_S=0, \alpha_R=1, \gamma_{1,2}=0$); c) RAOB's and SATOB field structure ($\alpha_S=0, \alpha_R=1, \gamma_{1,2}=10$). RMS error is minimized for c) with RAOB data densities commonly seen over the northern hemisphere.

To illustrate this process in the present study we look at a case where the frontal zone was over the Mediterranean. RAOB's are available around the sea and on a few islands. Representative satellite observations are shown in Figure IV-1.

Figure A-1-4 a through c show spline analyses for the three data conditions in the test case. Of course here there is no true field for comparison, but frontal zone definition is slightly improved.

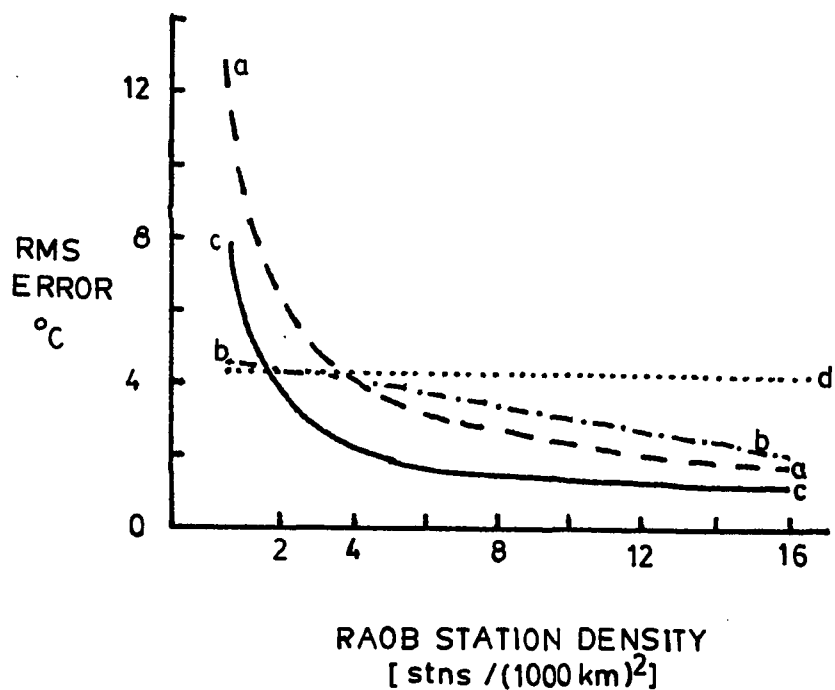


Fig. A-1-3. RMS error in the reproduction of a known temperature field, Satellite data was assumed to have a density of 30 reports per $(1000\text{km})^2$. This is similar to actual data. RAOB data density over Europe is about 11, over the Mediterranean, 6. Curve "a" is error with RAOBs only; curve "b", RAOBs and raw SATOBs; curve "c", RAOBs with shape matched satellite data. Curve "d" shows the level of error for SATOBs alone.

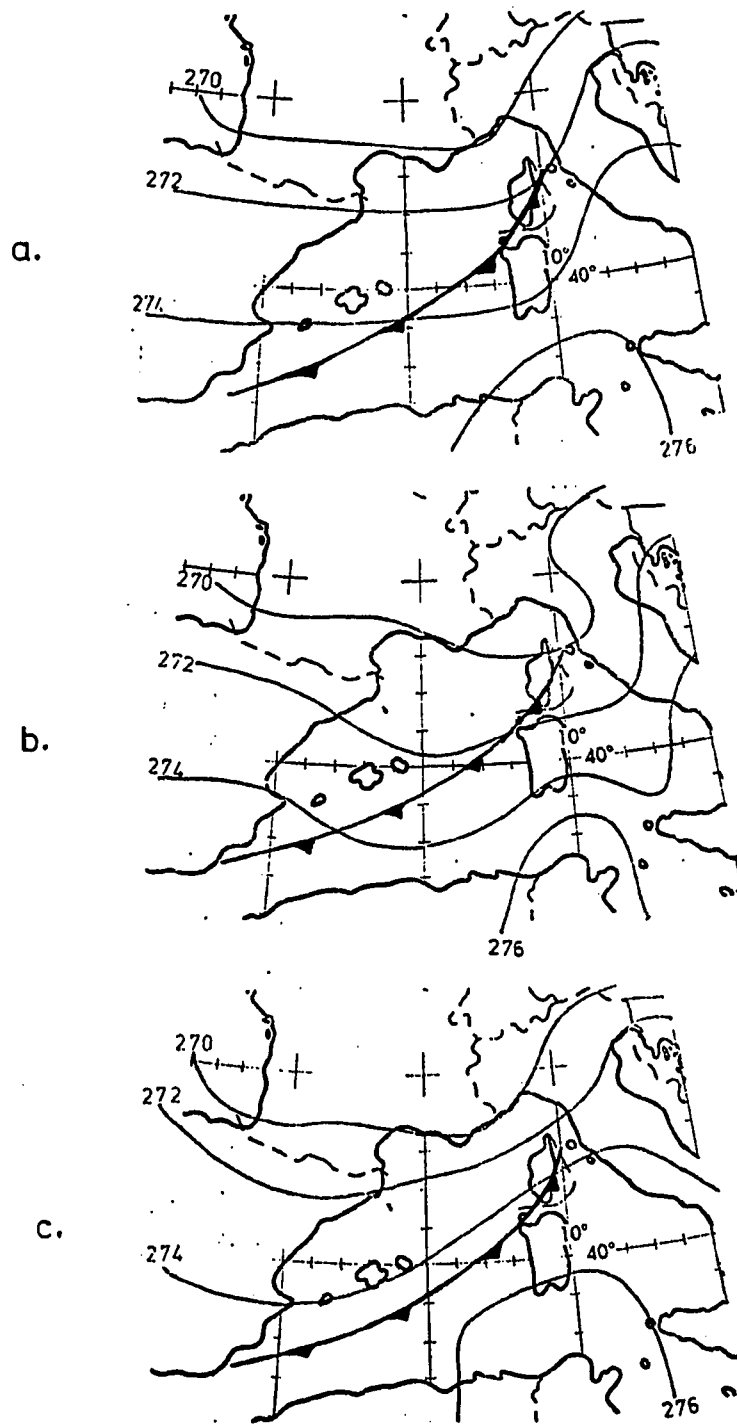


Fig. A-1-4. 850 mb temperature analyses over Mediterranean for 14 Feb. 1976, 1200 GMT ($^{\circ}$ K). Frontal position is based on surface reports.

- a. RAOB only.
- b. RAOB and raw SATOBs.
- c. RAOB with shape matching.

APPENDIX 2

Development of Low Pass Filter

From the text, Formalism 1 was given as:

$$F_1 = \int_{\lambda} \int_{\phi} \int_{\pi} \{ \tilde{\alpha} (\theta - \tilde{\theta})^2 + \beta (\nabla_3^2 \theta - \tan \phi \frac{\partial \theta}{a \partial \phi})^2 \} d\lambda d\phi d\pi$$

Applying the variational operator, δ yields

$$\delta F_1 = \int_{\lambda} \int_{\phi} \int_{\pi} \{ 2(\theta - \tilde{\theta}) \delta \theta + 2(\nabla_3^2 \theta - \tan \phi \frac{\partial \theta}{a \partial \phi}) (\nabla_3^2 \delta \theta - \tan \phi \frac{\partial \delta \theta}{a \partial \phi}) \} d\lambda d\phi d\pi .$$

Setting $\delta F_1 = 0$, gives

$$\int_{\lambda} \int_{\phi} \int_{\pi} \{ (\theta - \tilde{\theta}) \delta \theta + \nabla_3^2 \theta \nabla_3^2 \delta \theta - \tan \phi \frac{\partial \theta}{a \partial \phi} \nabla_3^2 \delta \theta - \nabla_3^2 \theta \tan \phi \frac{\partial \delta \theta}{a \partial \phi} + \tan^2 \phi \frac{\partial \theta}{a^2 \partial \phi} \frac{\partial \delta \theta}{\partial \phi} \} d\lambda d\phi d\pi = 0$$

and integration by parts yields

$$\begin{aligned} & \int_{\lambda} \int_{\phi} \int_{\pi} \left\{ \frac{\beta}{a^4} \left[\frac{1}{\cos^4 \phi} \frac{\partial^4 \theta}{\partial \lambda^4} + \frac{\partial^4 \theta}{\partial \phi^4} + \frac{a^4 \partial^4 \theta}{\partial r^4} + \frac{2}{\cos^2 \phi} \frac{\partial^4 \theta}{\partial \phi^2 \partial \lambda^2} \right] + \frac{\beta}{a^2} \right. \\ & \left. \left[\frac{2}{\cos^2 \phi} \frac{\partial^4 \theta}{\partial \lambda^2 \partial r^2} + \frac{2 \partial^4 \theta}{\partial r^2 \partial \phi^2} + \frac{4 \sin \phi}{a \cos^3 \phi} \frac{\partial^3 \theta}{\partial \phi \partial \lambda^2} + \frac{9 \sin^2 \phi}{\cos \phi} + \frac{3}{\cos^2 \phi} \right) \right. \\ & \left. \frac{\partial^2 \theta}{\partial \lambda^2} + \left(-\frac{1}{\cos^2 \phi} - \tan^2 \phi \right) \frac{\partial^2 \theta}{\partial \phi^2} + \frac{a^2}{\cos^2 \phi} \frac{\partial^2 \theta}{\partial r^2} - \frac{4 a \sin \phi}{\cos^3 \phi} \frac{\partial \theta}{\partial \phi} \right] \\ & + \tilde{\alpha} (\theta - \tilde{\theta}) \} d\pi d\phi d\lambda + \text{boundary terms} = 0 \end{aligned} \quad (\text{A-2-1})$$

If we assume $\delta\theta$ and $\vec{n} \cdot \nabla\delta\theta$ (where \vec{n} is an outward directed normal vector) are zero on the boundary, the boundary terms vanish and {} term must be zero. This equation is the analysis equation which is finite differenced and solved over the domain. The boundary condition requires that variations $\delta\theta$ are zero on two boundary rows of grid points about the analysis area. The vertical smoothing characteristics can be controlled (reduced) by transforming the vertical coordinate π to a new axis r . The horizontal filter response for the spline is obtained by assuming a known harmonic for $\theta (= Ae^{ika(\cos\phi\Delta\lambda + \Delta\phi)})$, where $\Delta\lambda$ and $\Delta\phi$ are grid spacing and k is the wave number. Substituting θ into the bracketed {} part of A-2-1, and computing the ratio of amplitudes as a function of L ,

$$r^* = \left\{ 1 + \beta/\tilde{\alpha} \frac{1}{a^4} \frac{16 \sin^4 \left(\frac{\pi}{L} a \cos \phi \Delta \lambda \right) - \frac{4 \sin^2 \left(\frac{\pi}{L} R \cos \phi \Delta \lambda \right)}{\cos^4 \phi} \right. \\ \left. 9(\sin^2 \phi + 3 \cos^2 \phi) \Delta \lambda^2 + 16 \sin^4 \left(\frac{\pi}{L} a \Delta \phi \right) + 4 \sin^2 \left(\frac{\pi a \Delta \phi}{L} \right) \right. \\ \left. \left(\frac{1}{\cos^2 \phi} + \tan^2 \phi \right) \Delta \phi^2 - \frac{8}{\cos^2 \phi} \left(\sin^2 \left(\frac{\pi a \cos \phi \Delta \phi}{L} - \frac{\pi a \Delta \phi}{L} \right) \right. \right. \\ \left. \left. + \sin^2 \left(\frac{\pi a \cos \phi \Delta \phi}{L} + \frac{\pi a \Delta \phi}{L} \right) \right) \right\}^{-1}$$

where L is wave length. Here π is 3.14159.... The response, r^* is plotted in Figure II-1.

The equation A-2-1 is solved by relaxation which reduces the residual 5 orders of magnitude in 20 iterations. RMS deviations from grid points with data are .5 to 1.°C for temperature and .5 to 1.m/sec for winds. Satellite data alone is processed with this filter prior to introducing it as a structural constraint as shown in Chapter II (Equation II-2) and Appendix 3.

APPENDIX 3

Horizontal Shape Matching

Formalism 2 is given in the text as

$$F_2 = \int_{\lambda} \int_{\phi} \int_{\pi} \{ \alpha_r (\theta - \tilde{\theta}_r)^2 + \alpha_s (\theta - \tilde{\theta}_s) + \beta (\nabla_3^2 \theta)^2 + \gamma_1 (\nabla \theta - \nabla \hat{\theta}_s)^2 + \gamma_2 (\nabla^2 \theta - \nabla^2 \hat{\theta}_s)^2 \} d\pi d\phi d\lambda$$

Development is similar to that in Appendix 2.

The analysis equation is

$$\begin{aligned} & \frac{\beta + \gamma_2}{a^4} \left[\frac{1}{\cos^4 \phi} \frac{\partial^4 \theta}{\partial \lambda^4} + \frac{\partial^4 \theta}{\partial \phi^4} + a \frac{\partial^4 \theta}{\partial r^4} + \frac{2}{\cos^2 \phi} \frac{\partial^4 \theta}{\partial \phi^2 \partial \lambda^2} \right] \\ & + \frac{\beta}{a^2} \left[\frac{2}{\cos^2 \phi} \frac{\partial^4 \theta}{\partial \lambda^2 \partial r^2} + \frac{2 \partial^4 \theta}{\partial r^2 \partial \phi^2} + \frac{4 \sin \phi}{a \cos^3 \phi} \frac{\partial^3 \theta}{\partial \phi \partial \lambda^2} \right. \\ & + \left(\frac{9 \sin^2 \phi}{\cos^4 \phi} + \frac{3}{\cos^2 \phi} \right) \frac{\partial^2 \theta}{\partial \lambda^2} + \left(\frac{-1}{\cos^2 \phi} - \tan^2 \phi \right) \frac{\partial^2 \theta}{\partial \phi^2} \\ & \left. + \frac{a^2}{\cos^2 \phi} \frac{\partial^2 \theta}{\partial r^2} - \frac{4 a \sin \phi}{\cos^3 \phi} \frac{\partial \theta}{\partial \phi} \right] \\ & - \frac{\gamma_1}{a^4} \left[\frac{1}{\cos^4 \phi} \frac{\partial^4 \hat{\theta}_s}{\partial \lambda^4} + \frac{\partial^4 \hat{\theta}_s}{\partial \phi^4} + \frac{2}{\cos^2 \phi} \frac{\partial^4 \hat{\theta}_s}{\partial \phi^2 \partial \lambda^2} \right] \\ & + \left(-\frac{1}{\cos^2 \phi} - \tan^2 \phi \right) \frac{\partial^2 \hat{\theta}_s}{\partial \phi^2} \\ & - \frac{\gamma_1}{a^2 \cos^2 \phi} \left(\frac{\partial^2 \theta}{\partial \lambda^2} - \frac{\partial^2 \hat{\theta}_s}{\partial \lambda^2} \right) - \frac{\gamma_1}{a^2} \left(\frac{\partial^2 \theta}{\partial \phi^2} - \frac{\partial^2 \hat{\theta}_s}{\partial \phi^2} \right) + \tilde{\alpha}_s (\theta - \tilde{\theta}_s) \\ & + \tilde{\alpha}_r (\theta - \tilde{\theta}_r) = 0 \end{aligned}$$

Again ($\tilde{}$) refers to observations at discrete grid points; ($\hat{}$) refers to fields resulting from F_1 ; $\tilde{\alpha}_s$ and $\tilde{\alpha}_r$ are zero where no observations exist. This equation is solved using Liebmann relaxation with boundary condition defined as in Appendix 2. Similar convergence is noted as with Equation A-2-1. $\gamma_1 = 0$ and $\gamma_2 = 10$ gives the fastest convergence for the amount of satellite structure imposed on the temperature field. Boundary values which are very important, are derived using a Barnes (1973) technique. Data outside the boundaries are included.

APPENDIX 4

Dynamic Adjustment

Beginning with the three-dimensional version in x, y, σ coordinates ($\sigma = \frac{p}{p_s}$) of E_3 and taking the variation results in

$$\begin{aligned} \delta F_3 = & \int_{\lambda} \int_{\phi} \int_{\sigma} \{ 2(\Phi - \tilde{\Phi})\delta\Phi + 2\gamma(u - \tilde{u})\delta u + 2\gamma(v - \tilde{v})\delta v \\ & + 2\Delta \left(fv - \frac{\partial\Phi}{\partial x} + \frac{1}{p_s} \frac{\partial\Phi}{\partial\sigma} \frac{\partial p_s}{\partial x} \right) (f\delta v - \frac{\partial\delta\Phi}{\partial x} + \frac{1}{p_s} \frac{\partial\delta\Phi}{\partial\sigma} \frac{\partial p_s}{\partial x}) \\ & + 2\Delta \left(fu + \frac{\partial\Phi}{\partial y} - \frac{1}{p_s} \frac{\partial\Phi}{\partial\sigma} \frac{\partial p_s}{\partial y} \right) (f\delta u + \frac{\partial\delta\Phi}{\partial y} - \frac{1}{p_s} \frac{\partial\delta\Phi}{\partial\sigma} \frac{\partial p_s}{\partial y}) \} d\sigma d\phi d\lambda, \end{aligned}$$

where $x = a \cos \phi \lambda$, $y = a \phi$, and a is the earth's radius. To use for data on a pressure surface we let $p_s = p_0$ (a constant).

Expansion of terms, integration by parts, and assuming that all variations vanish on the boundary, results in 3 equations in 3 unknowns (Φ, u, v):

$$\begin{aligned} 1. \quad & \frac{\partial^2 \Phi}{\partial x^2} + \frac{\partial^2 \Phi}{\partial y^2} + \frac{1}{p_s^2} \frac{\partial^2 \Phi}{\partial \sigma^2} (|\nabla p_s|^2) - \frac{2}{p_s} \frac{\partial p_s}{\partial x} \frac{\partial^2 \Phi}{\partial x \partial \sigma} \\ & - \frac{2}{p_s} \frac{\partial p_s}{\partial y} \frac{\partial^2 \Phi}{\partial y \partial \sigma} - \frac{2\beta}{fA} \frac{\partial \Phi}{\partial y} + \frac{\partial \Phi}{\partial \sigma} \left(\frac{1}{p_s^2} |\nabla p_s|^2 - \frac{1}{p_s} \frac{\partial^2 p_s}{\partial x^2} - \frac{1}{p_s} \frac{\partial^2 p_s}{\partial y^2} \right) \quad A-4-1 \\ & + \frac{2\beta}{fp_s A} \frac{\partial p_s}{\partial y} - \frac{1}{B\Delta} (\Phi - \tilde{\Phi}) - \frac{\gamma}{Bf\Delta} \tilde{\zeta} + \tilde{u}\beta A = 0 \end{aligned}$$

Boundary condition: $\Phi = \tilde{\Phi}$ on horizontal and vertical boundaries.

$$2. \quad u = B\tilde{u} + A\left(-\frac{1}{f} \frac{\partial \Phi}{\partial y}\right) \quad A-4-2$$

$$3. \quad v = B\tilde{v} + A\left(\frac{1}{f} \frac{\partial \Phi}{\partial x}\right) \quad A-4-3$$

where $A = (1 + \frac{\gamma}{\Delta f^2})$ and $B = \frac{\gamma}{\Delta f^2}/A$, $\tilde{\zeta}$ is the vertical component of vorticity and β is $\partial f/\partial y$. Equation 1 is solved by relaxation, then 2 and 3 are used to obtain u and v . The numerical convergence to solution of A-4-1 is sensitive to the choice of Δ . As Δ increases, convergence becomes slower in an iterative sense.

The three-dimensional graph in Figure II-3 applies only to the known signal which defines the curve \tilde{R}_G (the error in the geostrophic equation computed from the observed data). In general, \tilde{R}_G is a function of the particular data set and filtering steps leading up to the dynamical adjustment. The value of \tilde{R}_G at low wavelengths is normally much reduced (owing to the low pass filter). We have measured \tilde{R}_G for the various cases only in an average sense. Spectral decomposition of this residual was not accomplished.

APPENDIX 5

MASS CONSTRAINT, IMPLIED VERTICAL SCALE

As shown in the text, the formalism is

$$F_4 = \int_{\lambda} \int_{\phi} \int_{\sigma} \left\{ (u-\hat{u})^2 + (v-\hat{v})^2 + \tau(\dot{\sigma}-\hat{\sigma})^2 + \Omega \left(\frac{p_s}{a} \frac{\partial u}{\cos\phi\partial\lambda} + \frac{u}{a} \frac{\partial p_s}{\cos\phi\partial\lambda} \right. \right. \\ \left. \left. + \frac{p_s}{a} \frac{\partial v}{\partial\phi} + \frac{v}{a} \frac{\partial p_s}{\partial\phi} + p_s \frac{\partial \dot{\sigma}}{\partial\sigma} + \frac{\partial p_s}{\partial\tau} - p_s v \frac{\tan\phi}{a} \right) \right\} d\sigma d\phi d\lambda$$

Taking the variation,

$$\delta F_4 = 0 = \int_{\lambda} \int_{\phi} \int_{\sigma} \left\{ 2(u-\hat{u}) \delta u + 2(v-\hat{v}) \delta v + 2\tau(\dot{\sigma}-\hat{\sigma}) \delta \dot{\sigma} \right. \\ \left. + \delta\Omega \left(\frac{p_s}{a} \frac{\partial u}{\cos\phi\partial\lambda} + \frac{u}{a} \frac{\partial p_s}{\cos\phi\partial\lambda} + \frac{p_s}{a} \frac{\partial v}{\partial\phi} + \frac{v}{a} \frac{\partial p_s}{\partial\phi} + p_s \frac{\partial \dot{\sigma}}{\partial\sigma} + \frac{\partial p_s}{\partial\tau} \right) \right. \\ \left. + \Omega \left(\frac{p_s}{a} \frac{\partial \delta u}{\cos\phi\partial\lambda} + \frac{\delta u}{a} \frac{\partial p_s}{\cos\phi\partial\lambda} - p_s \frac{\tan\phi}{a} \delta v + \frac{p_s}{a} \frac{\partial \delta v}{\partial\phi} + \frac{\delta v}{a} \frac{\partial p_s}{\partial\phi} + p_s \frac{\partial \delta \dot{\sigma}}{\partial\sigma} \right) \right\} \\ d\sigma d\phi d\lambda$$

The Euler-Lagrange equations are found by integrating by parts and assuming variations vanish on the boundary. These equations are:

$$u = \hat{u} + \frac{p_s}{a} \frac{\partial \Omega}{\cos\phi\partial\lambda} \quad \text{A-5-1}$$

$$v = \hat{v} + \frac{p_s}{a} \frac{\partial \Omega}{\partial\phi} - \frac{p_s \Omega \tan\phi}{a} \quad \text{A-5-2}$$

$$\dot{\sigma} = \hat{\sigma} + \frac{p_s}{\tau} \frac{\partial \Omega}{\partial\sigma} \quad \text{A-5-3}$$

$$\frac{p_s}{a} \left(\frac{u}{\cos\phi\partial\lambda} + \frac{\partial v}{\partial\phi} \right) + \frac{u}{a} \frac{\partial p_s}{\cos\phi\partial\lambda} + \frac{v}{a} \frac{\partial p_s}{\partial\phi} + p_s \frac{\partial \dot{\sigma}}{\partial\sigma} + \frac{\partial p_s}{\partial\tau} = 0 \quad \text{A-5-4}$$

To solve this system of equations, we substitute u , v , $\dot{\sigma}$ from A-5-1 to A-5-3 into A-5-4. This results in an elliptic equation for Ω . The weight τ is the only controlling parameter and basically determines the contribution of the quasi-geostrophic estimate of vertical motion, $\hat{\sigma}$.

The equation for Ω is found to be:

$$\begin{aligned} & \frac{1}{a^2} \left(\frac{\partial^2 \Omega}{\cos \phi \partial \lambda^2} + \frac{\partial^2 \Omega}{\partial \phi^2} \right) + \frac{1}{\tau} \frac{\partial^2 \Omega}{\partial \sigma^2} + \frac{1}{a^2 \cos^2 \phi} \left(\frac{2 p_s}{p_s} \frac{\partial \Omega}{\partial \lambda} \right) \frac{\partial \Omega}{\partial \lambda} + \frac{1}{a} \left(\frac{2}{p_s} \frac{\partial p_s}{\partial \phi} \right) \frac{\partial \Omega}{\partial \phi} \\ & + \frac{1}{a p_s} \frac{\partial \hat{u}}{\cos \phi \partial \lambda} + \frac{\partial \hat{v}}{\partial \phi} + \frac{\hat{u}}{p_s} \frac{\partial p_s}{\cos \phi \partial \lambda} + \frac{\hat{v}}{p_s} \frac{\partial p_s}{\partial \phi} + \frac{a}{p_s} \frac{\partial p_s}{\partial \tau} + \frac{a \partial \hat{\sigma}}{\partial \sigma} \\ & - \frac{p_s}{a} \frac{\partial \Omega}{\partial \phi} \tan \phi - \frac{p_s}{a} \Omega \sec^2 \phi = 0 \end{aligned}$$

with boundary conditions $\Omega = 0$ on the horizontal boundary ($u = \hat{u}$, $v = \hat{v}$); and $\frac{\partial \Omega}{\partial \sigma} = 0$ on the lower boundary (owing to the fact that $\dot{\sigma} = \hat{\sigma} = 0$ at $\sigma = 1$). At the upper boundary we want $\omega = 0$, or $\dot{\sigma}_s = \sigma_{top} \dot{p}_s / p_s$. This implies that $\frac{\partial \Omega}{\partial \sigma} = - \frac{\tau}{p_s} \left(\frac{\sigma_{top}}{p_s} \dot{p}_s - \hat{\sigma} \right)$. This equation is solved and the solution (Ω) substituted into A-5-1, 2 and 3 to find u , v , and $\dot{\sigma}$.

A more useful definition of τ can be derived if we run a test of flow over an obstacle. Assume that we have a bell shaped mountain defined by an exponential with maximum height at 500 mb. A uniform wind field from west to east interacts with the mountain. Figure A-5-1a shows the vertical motion profile on the slope of the mountain for varying values of τ . The exponential decay of the externally generated vertical motion (ω) with decreasing pressure can be controlled with τ (Figure A-5-1b). Figure 1c shows the maximum deflection in the horizontal wind and the distribution of horizontal wind modification with height. For τ small the horizontal wind adjustment is spread evenly through each layer similar to other kinematic vertical motion schemes discussed. As shown in Chapter II a vertical scale can be derived

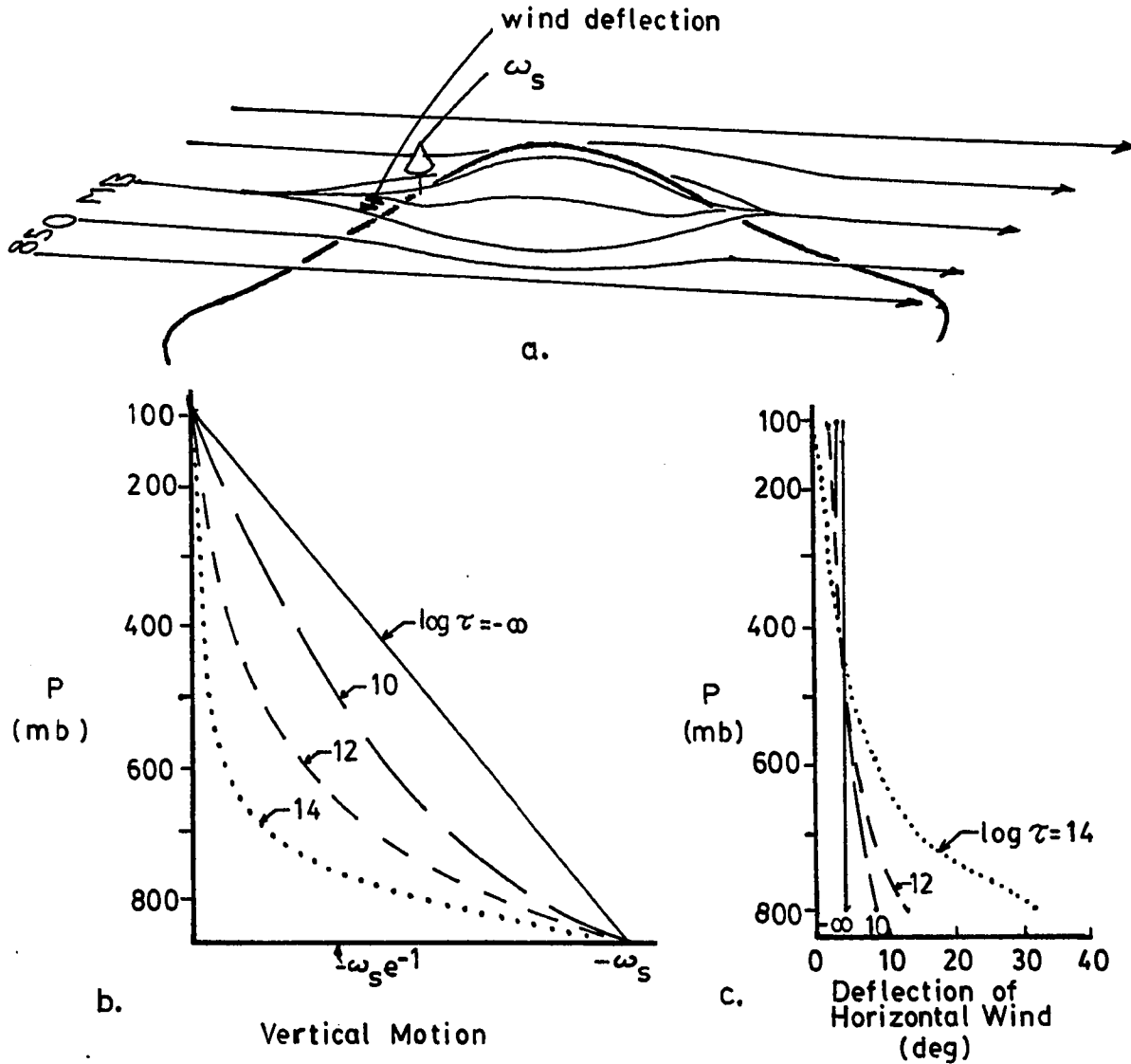


Fig. A-5-1. Air flow moving over bell-shaped obstacle. Environmental vertical motion (ω_e) is assumed to be zero. A straight west to east flow of air at 20 m/sec impinges on mountain.

- Schematic of experiment. ω_s is -0.033 mb/sec.
- Vertical motion (ω) above point on slope of mountain at 850 mb. Arrow indicates where ω falls off an exponential factor. Curves indicated are functions of τ as indicated.
- Maximum horizontal deflection of wind at each level for a given τ . For τ small, adjustment occurs at all levels equally; as τ increases, adjustments move closer to surface and increase.

by knowledge of the regional stability and terrain dimensions (Buzzi and Tibaldi, 1977). The vertical scale,

$$H_0 = L_T \left(\frac{1 - R_0^2}{\frac{g}{f_0^2 \sigma} \frac{\partial \theta}{\partial z}} \right)$$

is a function of terrain scale, L_T ; Rossby number, and stability, $\frac{\partial \theta}{\partial z}$. For the Alps H_0 is about 3.0km. This corresponds to a value of $\tau \sim 10^{11} \text{ m}^2$ (from A-5-1d).

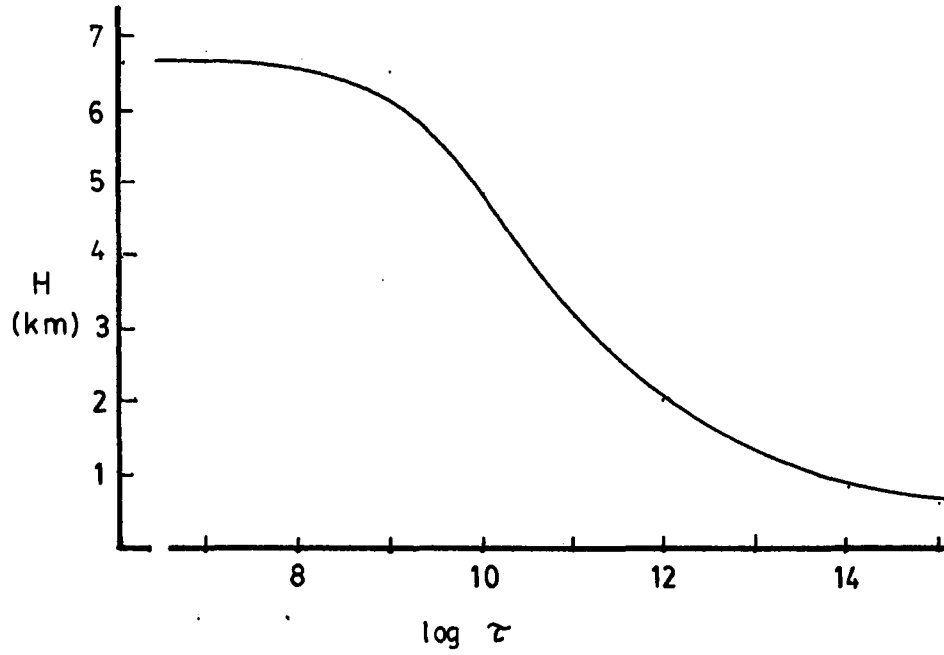


Fig. A-5-1

d. Scale height versus $\log z$. The indicated heights are the vertical distance between the point on the slope and the point at which the vertical motion has decayed one exponential factor.

APPENDIX 6

POTENTIAL VORTICITY CONSTRAINT AND GEOSTROPHIC ADJUSTMENT

A strong constraint which conserves potential vorticity can help to make wind fields more representative especially over obstacles of limited size. For the Alps the observed data did a marginal job in defining the anticyclone over the ridge and low in the lee. Such a constraint allows the wind field to reflect these features even in areas where no data is available.

A simplified representation of potential vorticity can be defined as

$$P \equiv \frac{1}{p_s - p_t} (\zeta + f)$$

Where $p_s(x,y)$ is the surface pressure and p_t is the pressure at the top of the column. Conservation of the above quantity is applied as a strong constraint during the geostrophic adjustment phase. The formalism includes observed wind fields and geopotential fields, introduced through the vorticity.

Let

$$F_3 = \int_A \int_{p_s}^{p_t} \{ (\zeta_g - \tilde{\zeta}_g)^2 + \gamma(\zeta - \tilde{\zeta})^2 + \Delta(\zeta - \zeta_g) \} dp$$

$$+ \lambda \int_{p_s}^{p_t} \left[\frac{d}{dt} S(\zeta + f) \right] dx dy$$

where $S = \left(\frac{1}{p_s - p_t} \right)$, $\zeta = \frac{\partial v}{\partial x} - \frac{\partial u}{\partial y}$, $\zeta_g = \frac{1}{f} \nabla^2 \phi(\sim)$ imply observed fields, $\lambda(x,y)$

is the Lagrange multiplier and γ and Δ have similar meanings as in Appendix 4, and $\frac{d}{dt}$ is the linearized operator $(\frac{\partial}{\partial t} + \tilde{u}\frac{\partial}{\partial x} + \tilde{v}\frac{\partial}{\partial y})$.

Taking the variation, integrating by parts, and allowing the variations to be arbitrary over the domain, we obtain 3 equations in the 3 unknowns, ζ , ζ_g and λ , and associated boundary conditions.

These are

$$\zeta_g = \frac{\zeta_g}{(\gamma + \Delta)} + \left(\frac{\Delta}{1+\Delta}\right) \zeta$$

$$\zeta = \frac{w_1 \gamma \tilde{\zeta}}{w_2} + \frac{\Delta}{w_2} \tilde{\zeta}_g + \frac{\lambda w_1}{2w_2} \tilde{\delta} + \frac{S w_1}{2w_2} (\tilde{u} \frac{\partial \lambda}{\partial x} + \tilde{v} \frac{\partial \lambda}{\partial y})$$

where $w_1 \equiv (1+\Delta)$, $w_2 \equiv (\gamma+\gamma\Delta+\Delta)$, $\tilde{\delta}$ is observed divergence and \tilde{u} and \tilde{v} are the observed winds, and

$$\begin{aligned} \langle \tilde{u}^2 \rangle \lambda_{xx} + \langle \tilde{v}^2 \rangle \lambda_{yy} + \langle 2\tilde{u}\tilde{v} \rangle \lambda_{xy} + \langle \tilde{u}\tilde{\delta} \rangle + \frac{2\tilde{u}^2}{S} \frac{\partial S}{\partial x} + \tilde{u} \frac{\partial \tilde{u}}{\partial x} + \frac{2\tilde{u}\tilde{v}}{S} \frac{\partial S}{\partial y} \\ + \tilde{v} \frac{\partial \tilde{u}}{\partial y} + \tilde{\omega} \frac{\partial \tilde{u}}{\partial p} \lambda_x + \langle \tilde{v}\tilde{\delta} \rangle + \frac{2\tilde{v}^2}{S} \frac{\partial S}{\partial y} + \tilde{v} \frac{\partial \tilde{v}}{\partial y} + 2\tilde{u}\tilde{v} \frac{\partial S}{\partial x} \\ + \tilde{u} \frac{\partial \tilde{v}}{\partial x} + \tilde{\omega} \frac{\partial \tilde{v}}{\partial p} \lambda_y + \langle \tilde{u}\tilde{\delta} \rangle + \tilde{v} \frac{\partial \tilde{\delta}}{\partial y} + \tilde{\omega} \frac{\partial \tilde{\delta}}{\partial p} + \frac{2\tilde{u}}{S} \frac{\partial S}{\partial x} \tilde{\delta} \\ + \frac{2\tilde{v}}{S} \frac{\partial S}{\partial y} \tilde{\delta} \rangle \lambda = -\frac{2w_2}{w_1} \left\langle \frac{1}{S} \frac{\partial \tilde{\zeta}}{\partial t} + \frac{1}{S} \tilde{v}\beta + \frac{f}{S^2} (\tilde{u} \frac{\partial S}{\partial x} + \tilde{v} \frac{\partial S}{\partial y}) \right. \\ \left. + \frac{\gamma w_1}{S^2 w_2} \tilde{\zeta} (\tilde{u} \frac{\partial S}{\partial x} + \tilde{v} \frac{\partial S}{\partial y}) + \frac{\Delta}{S^2 w_2} \tilde{\zeta}_g (\tilde{u} \frac{\partial S}{\partial x} + \tilde{v} \frac{\partial S}{\partial y}) \right. \\ \left. + \frac{\gamma w_1}{S w_2} (\tilde{u} \frac{\partial \tilde{\zeta}}{\partial x} + \tilde{v} \frac{\partial \tilde{\zeta}}{\partial y}) + \frac{\Delta}{S w_2} (\tilde{u} \frac{\partial \tilde{\zeta}_g}{\partial x} + \tilde{v} \frac{\partial \tilde{\zeta}_g}{\partial y}) \right. \\ \left. + \frac{\gamma w_1}{w_2 S} \tilde{\omega} \frac{\partial \tilde{\zeta}}{\partial p} + \frac{\Delta}{S w_2} \tilde{\omega} \frac{\partial \tilde{\zeta}_g}{\partial p} \right. \end{aligned}$$

with boundary condition $\int_y \int_p (\tilde{u}\lambda S \delta \zeta) \Big|_0^{x_0} dy dp$, $\int_x \int_p (\tilde{v}\lambda S \delta \zeta) \Big|_0^{y_0} dx dp$,

$$\int_x \int_y \lambda S (\omega \delta \zeta) \Big|_{p_t}^{p_s} dx dy, \text{ where } \langle \rangle \equiv \int_{p_t}^{p_s} dp. \text{ All tilde } (\tilde{\ }) \text{ terms are known from the}$$

data given.

This equation is parabolic but can be transformed to an elliptic equation by finding the characteristics. The slope of the characteristic lines is $\frac{\tilde{v}}{\tilde{u}}$ which are the streamlines of the observed winds.

Once solutions are obtained for λ , ζ and ζ_g can be found, allowing the nondivergent u and v , and ϕ to be recovered. The adjustment does not effect the divergent part of the observed wind.

To test this scheme an experiment similar to that in Appendix 5 is run. Here we assume west to east observed flow interacting with the same mountain. The characteristic curves are oriented along the x axis. The observed wind field has $\tilde{u} = 20\text{m/sec}$, $\tilde{v} = 0$ with $\tilde{\omega}$ related to terrain uplift. Solutions for λ are obtained with Dirichlet boundary conditions at both upstream and downstream boundaries. This gives spurious cyclonic vorticity near the boundaries. Figures A-6-1 show the geopotential field streamlines, vorticity, and vertical motions above the top of the mountain. The vorticity and geopotential result from the formalism in this appendix. These then serve as input into the continuity conservation scheme discussed in Appendix 5.

This scheme may be useful for analysis in mountainous regions, insuring that wind and geopotential fields reflect the effects of conservation of potential vorticity. Iteration of flow variables between this and the mass conserving scheme may be necessary, although reasonable results (Figure A-6-1) are obtained with only one application of each.

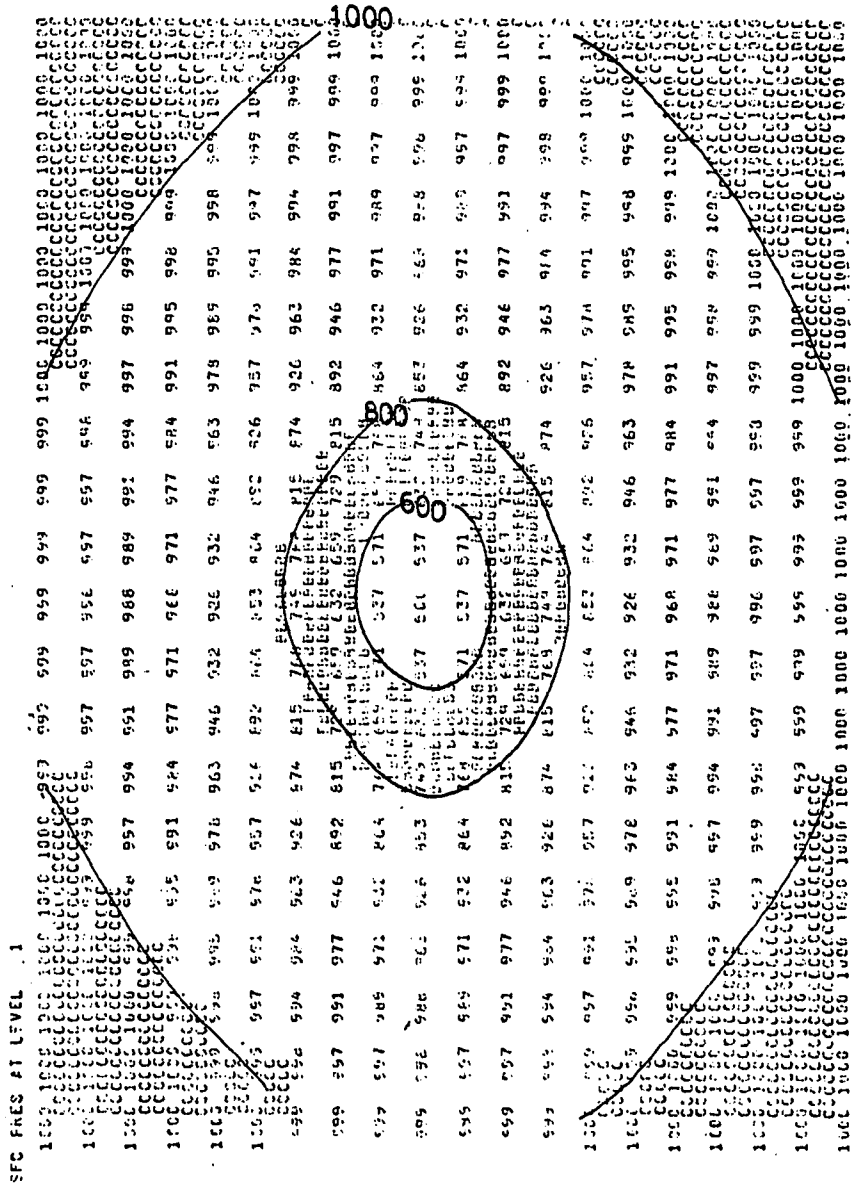


Fig. A-6-1a. Surface pressure over test terrain (mb). Grid spacing ($\Delta x, \Delta y$) is assumed to be 111 km.

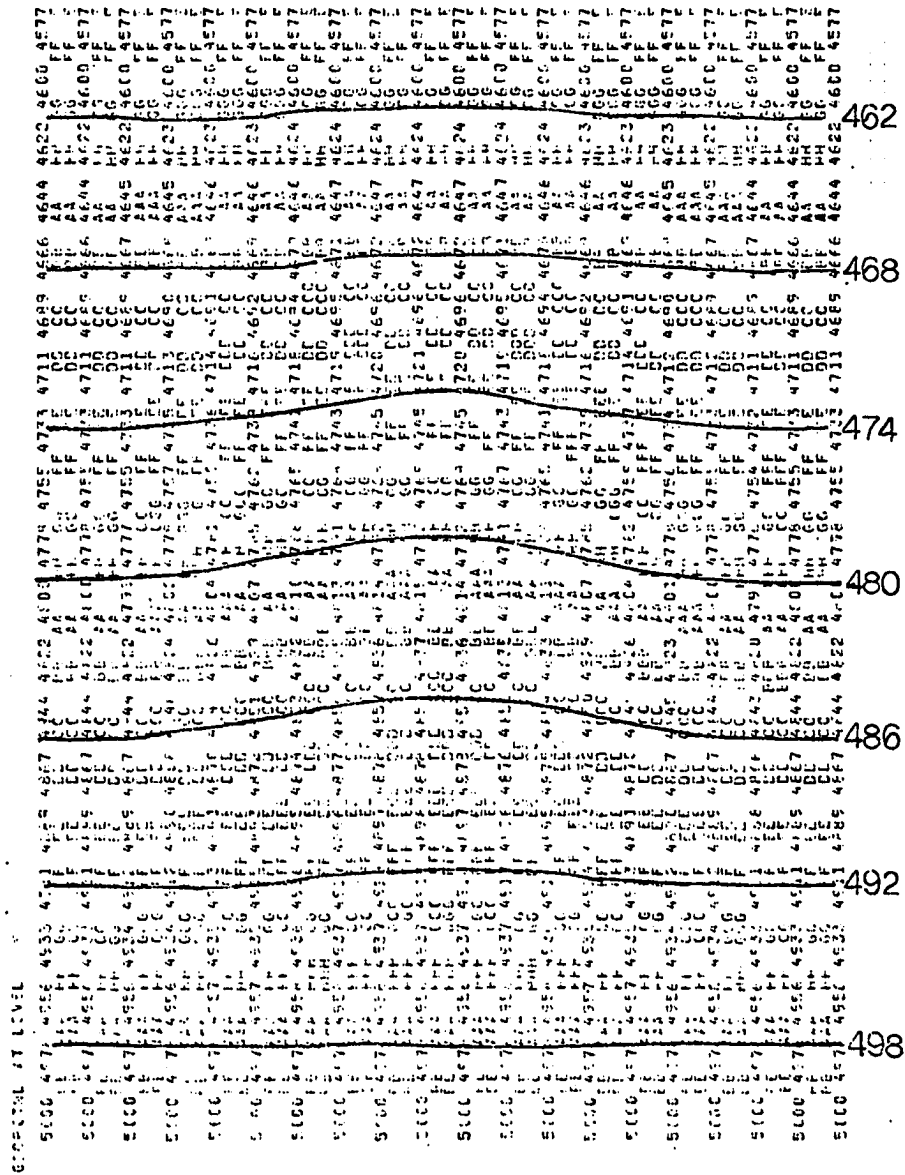


Fig. A-6-1b. Geopotential field from solution for $\gamma = \Delta = 1$, in cm. Observed geostrophic vorticity ζ_g , was assumed to be zero.

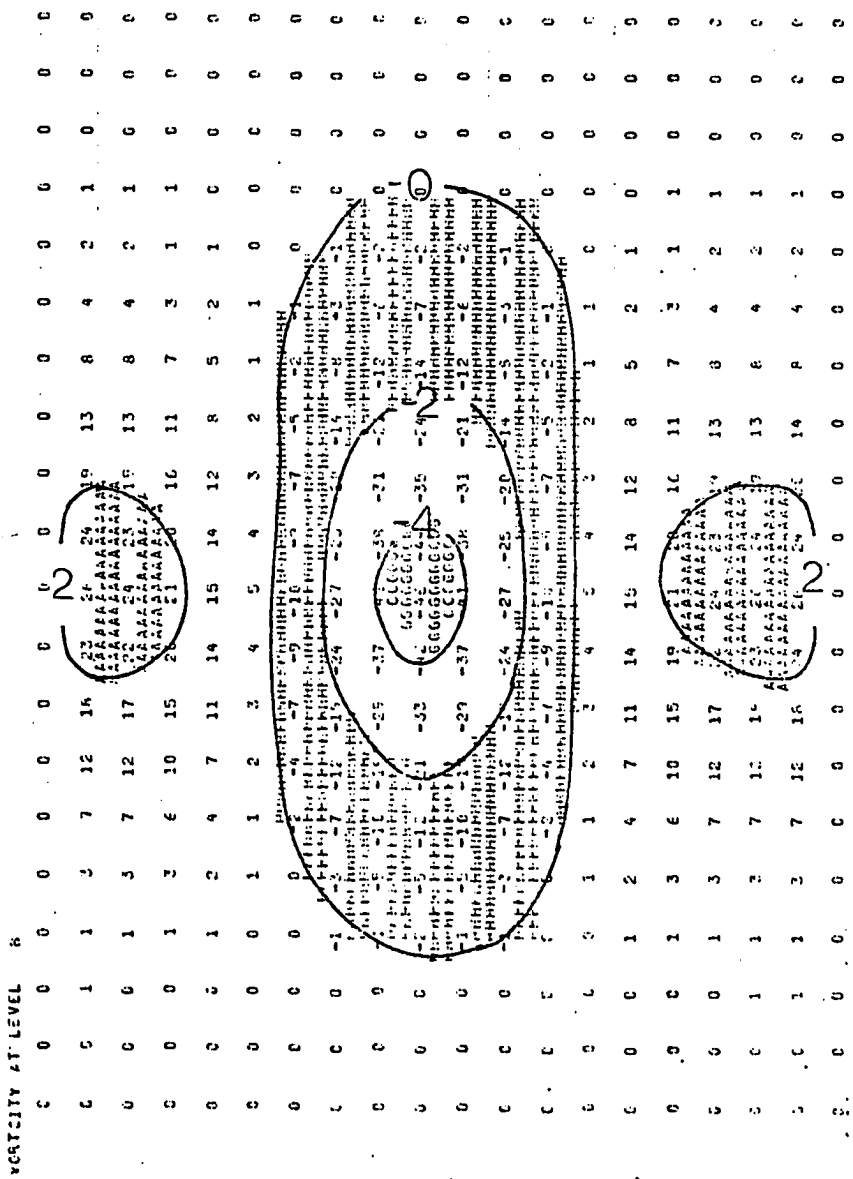


Fig. A-6-1c. Solution relative vorticity ($\text{sec}^{-1} \times 10^{-5}$) for $\gamma = \Delta = 1$. Observed winds were assumed to have zero vorticity, $\bar{\zeta} = 0$.

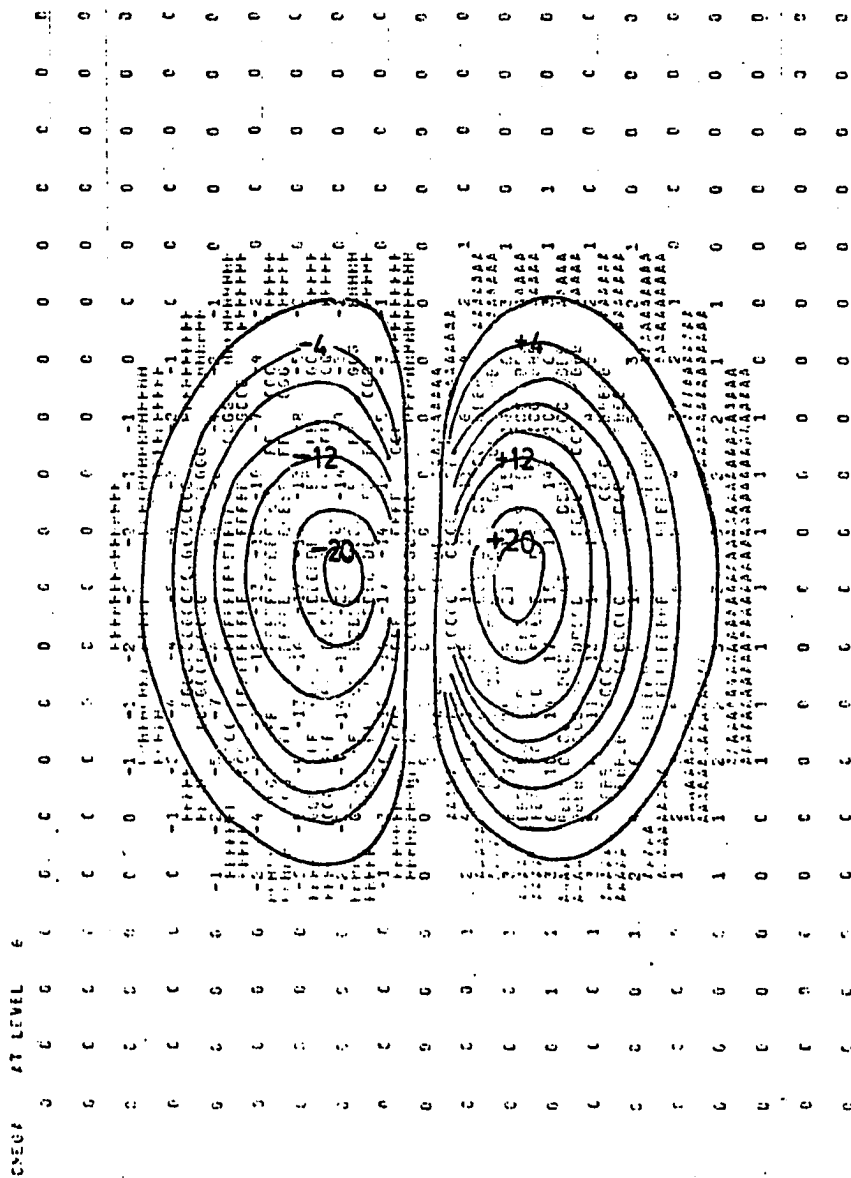


Fig. A-6-1d. Vertical motion (mb/sec x 10⁻³) at 500 mb.

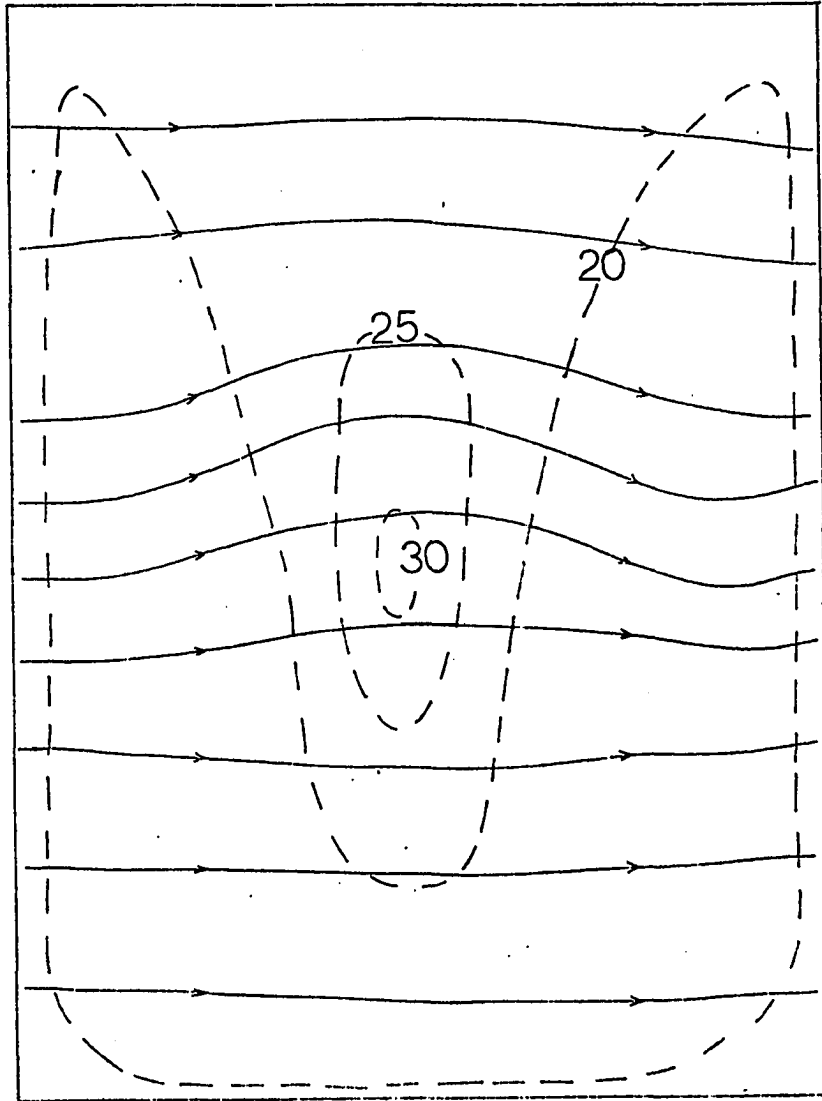


Fig. A-6-1e. Resulting streamlines (—), and isotachs (---) in m/sec for flow at 500 mb.

APPENDIX 7

The Energy Transformation Equations

In Chapter III transformation equations for the various energy quantities were given but not derived. Since we are considering open volumes, boundary fluxes become important. In addition, the meaning of the mean and perturbation quantities must be clarified.

By selecting a volume we have tried to isolate a complete wave from the flow. The flow defining this wave becomes the perturbation if the volume extends over one wavelength. Owing to the limitations of the analyzed region this was not always possible, particularly near the beginning and end of each case.

The equations are derived to describe the quasi-geostrophic energy transformations. In this framework we can assume that the horizontal winds are representable by a quasi-geostrophic stream function ψ^1 . The derived transformations serve as approximations to the actual processes but should be accurate enough to show the most important energy transformations during development. Deviations from the quasi-geostrophic redistributions may be used to infer processes not parameterized.

To define mean and perturbation quantities within the volumes, an average wind shear for the volume is determined and then used to define both the mean thermal gradient and mean wind. The mean wind at each level is

¹ Here the stream function is defined as $\psi \equiv \Phi / f_0$ where Φ is the geopotential at a given pressure level.

consistent with this wind shear. The stream function field is

$$\bar{\psi} = \psi_0 + \frac{\partial \bar{\psi}}{\partial p} (p - p_0) \text{ where } \psi_0 \text{ is the reference stream function}$$

at each level. The wind and specific volume are

$$\bar{V}(p) = \vec{k} \times \nabla \bar{\psi} \text{ and } \bar{\alpha} = -f_0 \frac{\partial \bar{\psi}}{\partial p} + \alpha_0$$

where $\alpha_0 = -f_0 \frac{\partial \psi_0}{\partial p}$.

Perturbation quantities are defined as departures from the mean values,

$$\begin{aligned} \psi' &= \psi - \bar{\psi} \\ \vec{V}' &= \vec{k} \times \nabla \psi' \\ \alpha' &= \alpha - \bar{\alpha} \end{aligned}$$

The bar notation should be clarified.

($\bar{\quad}$) defines the fields associated with the environment
(i.e. with the volume)

($\bar{\quad}$)^A $\equiv \frac{1}{A} \int () dA$, area average over volume cross section A

($\bar{\quad}$)^S $\equiv \frac{1}{S} \oint () dS$, line average around S, the boundary of A

$\langle \quad \rangle \equiv \frac{1}{g} \int () dp$, integral from top to surface of volume.

The vorticity equation in flux form is given by

$$\frac{\partial \nabla^2 \psi}{\partial t} = - \nabla \cdot (\vec{V} \nabla^2 \psi) + f_0 \frac{\partial \omega}{\partial p} \quad \text{A-7-1}$$

The mean vorticity equation can be found by averaging over a layer in the volume

$$\frac{\partial \bar{\nabla}^2 \psi}{\partial t} = - \nabla \cdot \bar{V} \nabla^2 \psi' + f_0 \frac{\partial \bar{\omega}}{\partial p} \quad \text{A-7-2}$$

The perturbation form of the vorticity equation is obtained by subtracting

A-7-2 from A-7-1.

$$\frac{\partial \nabla^2 \psi'}{\partial t} = - \nabla \cdot \vec{v} \nabla^2 \psi + \nabla \cdot \vec{v}' \nabla^2 \psi' + f_0 \frac{\partial \omega'}{\partial p} \quad \text{A-7-3}$$

Kinetic energy equations can be derived by multiplying A-7-2 and A-7-3 by $\bar{\psi}$ and ψ' , respectively, and integrating over the volume. The term on the left of A-7-2 becomes

$$\begin{aligned} \frac{1}{g} \iint \bar{\psi} \frac{\partial \nabla^2 \psi}{\partial t} dAdp &= \frac{1}{g} \iint \nabla \cdot (\bar{\psi} \frac{\partial \nabla \bar{\psi}}{\partial t}) dAdp - \frac{1}{g} \iint \nabla \bar{\psi} \cdot \frac{\partial}{\partial t} \nabla \bar{\psi} dAdp \\ &= \frac{S}{g} \int (\bar{\psi} \nabla \frac{\partial \bar{\psi}}{\partial t} \cdot \vec{n}) dp - \frac{1}{g} \iint \frac{1}{2} \frac{\partial}{\partial t} (\nabla \bar{\psi} \cdot \nabla \bar{\psi}) dAdp \end{aligned}$$

where \vec{n} is a unit outward directed normal to S. With $\bar{K} = \frac{1}{2} \nabla \bar{\psi} \cdot \nabla \bar{\psi} = \frac{1}{2} V^2$

$$= S \langle \bar{\psi} \nabla \frac{\partial \bar{\psi}}{\partial t} \cdot \vec{n} \rangle - A \frac{\partial}{\partial t} \langle \bar{K} \rangle$$

For a unit cross section

$$= \frac{S}{A} \langle \bar{\psi} \nabla \frac{\partial \bar{\psi}}{\partial t} \cdot \vec{n} \rangle - \frac{\partial}{\partial t} \langle \bar{K} \rangle$$

The right side of equation A-7-2 becomes

$$\begin{aligned} \frac{1}{g} \iint \bar{\psi} f_0 \frac{\partial \omega}{\partial p} - \bar{\psi} \nabla \cdot (\vec{v}' \nabla^2 \psi') dAdp &= \\ \frac{1}{g} \iint [-f_0 \frac{\partial \psi}{\partial p} \omega + f_0 \frac{\partial}{\partial p} (\omega \psi)] dAdp - \frac{1}{g} \iint \bar{\psi} \nabla \cdot (\vec{v}' \nabla^2 \psi') dAdp \\ &= \frac{A}{g} \int \bar{\alpha} \bar{\omega} dp + \frac{A}{g} (\bar{\omega} \bar{\Phi})_{p=p_s} - \frac{A}{g} \int \bar{\psi} \nabla \cdot (\vec{v}' \nabla^2 \psi') dp \end{aligned}$$

For a unit area

$$= \langle \alpha_0 \bar{\omega} \rangle + \frac{1}{g} (\bar{\omega} \bar{\Phi}_0)_{p=p_s} - \langle \psi_0 \nabla \cdot (\vec{v}' \nabla^2 \psi') \rangle$$

The mean kinetic energy equation is

$$\frac{\partial}{\partial t} \langle \bar{K} \rangle = -\langle \alpha_0 \bar{\omega} \rangle + \langle \psi_0 \overline{\nabla \cdot (\vec{v}' \nabla^2 \psi')} \rangle^A - \overline{(\omega \phi_0)}_{p=p_s}^A + \frac{S}{A} \overline{\langle \psi' \nabla \frac{\partial \psi'}{\partial t} \cdot \vec{n} \rangle}^S \quad A-7-4$$

Holton (1972) used the lower boundary condition $-(\omega \phi_0)_{p=p_s}$ to derive a frictional loss owing to Ekman layer pumping. In our analysis we have chosen to separately parameterize frictional effects since the boundary term may be dominated by orographic forcing. The last term is also a boundary flux. The volumes in our study had translation speeds from 10% to 25% of the mean wind. The volume changes will be determined by the Eulerian time changes.

The perturbation equation A-7-3 becomes

$$\begin{aligned} \frac{1}{g} \iint \psi' \frac{\partial}{\partial t} \nabla^2 \psi' \, dAdp &= -\frac{1}{g} \iint \psi' \nabla \cdot (\overline{\vec{v}' \nabla^2 \psi'}) \, dAdp - \frac{1}{g} \iint \psi' \nabla \cdot (\vec{v}' \nabla^2 \psi') \, dAdp \\ &- \frac{1}{g} \iint \psi' \nabla \cdot (\overline{\nabla \nabla^2 \psi'}) \, dAdp - \frac{1}{g} \iint \psi' \nabla \cdot (\vec{v}' \overline{\nabla^2 \psi'}) \, dAdp \\ &+ \frac{1}{g} \iint \psi' \overline{\nabla \cdot \vec{v}' \nabla^2 \psi'} \, dAdp + \frac{1}{g} \iint \psi' f_0 \frac{\partial \omega'}{\partial p} \, dAdp \end{aligned}$$

After similar manipulations as before the perturbation kinetic energy equation is

$$\begin{aligned} \frac{\partial \langle \bar{K} \rangle^A}{\partial t} &= -\langle \alpha_0 \bar{\omega}' \rangle^A - \langle \psi_0 \overline{\nabla \cdot (\vec{v}' \nabla^2 \psi')} \rangle^A - \frac{1}{g} \overline{(\omega \phi_0)}_{p=p_s}^A \\ &+ \frac{S}{A} \overline{\langle \psi' \nabla \frac{\partial \psi'}{\partial t} \cdot \vec{n} \rangle}^S + \frac{S}{A} \overline{\langle \psi' \nabla^2 \psi' \cdot \vec{v}' \cdot \vec{n} \rangle}^S \end{aligned} \quad A-7-5$$

Equations for available potential energy are obtained from the first law of thermodynamics, $\frac{d \ln \theta}{dt} = \frac{\dot{Q}}{c_p}$, where \dot{Q} describes the non-adiabatic processes. Since $\frac{RT}{f_0 p} = -\frac{\partial \psi}{\partial p} = -\psi_p$, the first law can be written

$$\frac{\partial \psi_p}{\partial t} = -\nabla \cdot (\vec{v}' \psi_p) - \frac{\sigma}{f_0} \omega - Rd$$

where $\sigma = -\frac{\alpha_0}{\theta} \frac{\partial \bar{\theta}}{\partial p}$, and $Rd = \frac{\alpha_0}{f_0 c_p} \dot{Q}$.

Proceeding as before, we separate the equation into mean and perturbation components. The mean equation is

$$\frac{\partial \bar{\psi}_p}{\partial t} = - \overline{\nabla \cdot \vec{v} \psi_p^{\prime A}} - \frac{\sigma}{f_0} \bar{\omega} - \bar{R}_d \quad \text{A-7-6}$$

The perturbation equation is

$$\frac{\partial \psi_p^{\prime}}{\partial t} = - \nabla \cdot (\vec{v} \bar{\psi}_p + \bar{v} \psi_p^{\prime} + \vec{v} \psi_p^{\prime}) + \overline{\nabla \cdot \vec{v} \psi_p^{\prime A}} - \frac{\sigma \omega^{\prime}}{f_0} - R_d^{\prime} \quad \text{A-7-7}$$

Energy equations are obtained by multiplying A-7-6 and A-7-7 by $\frac{f_0^2}{\sigma} \bar{\psi}_p$ and $\frac{f_0^2}{\sigma} \psi_p^{\prime}$ respectively, and integrating over the volume. For A-7-6,

$$\begin{aligned} \frac{1}{g} \iint \frac{f_0^2}{2\sigma} \frac{\partial \bar{\psi}_p^2}{\partial t} dAdp = & - \frac{1}{g} \iint \frac{f_0^2}{\sigma} \bar{\psi}_p \overline{\nabla \cdot \vec{v} \psi_p^{\prime A}} dAdp - \frac{1}{g} \iint f_0 \bar{\psi}_p \bar{\omega} dAdp \\ & - \frac{1}{g} \iint \frac{f_0^2}{\sigma} \bar{\psi}_p \bar{R}_d dAdp \end{aligned}$$

The integral on the left is the mean available potential energy.

After some manipulation, for a unit area,

$$\begin{aligned} \frac{\partial \langle \overline{\text{APE}} \rangle}{\partial t} = & \frac{\overline{\alpha_0 \bar{\omega}}}{\sigma} A + \left\langle \frac{f_0^2}{\sigma} \overline{\nabla \psi_p} \cdot \overline{\vec{v} \psi_p^{\prime A}} \right\rangle - \left\langle \frac{f_0^2}{\sigma} \bar{\psi}_p \bar{R}_d \right\rangle \\ & - \frac{S}{A} \frac{f_0^2}{\sigma} \overline{(\bar{\psi}_p \vec{v} \psi_p^{\prime}) \cdot \vec{n}} \quad \text{A-7-8} \end{aligned}$$

The perturbation equation becomes

$$\begin{aligned} \frac{1}{g} \iint \frac{f_0^2}{2\sigma} \frac{\partial \bar{\psi}_p^2}{\partial t} dAdp = & - \frac{1}{g} \iint \frac{f_0^2}{\sigma} \bar{\psi}_p \nabla \cdot (\vec{v} \bar{\psi}_p + \bar{v} \psi_p^{\prime} + \vec{v} \psi_p^{\prime}) dAdp \\ & + \frac{1}{g} \iint \frac{f_0^2}{\sigma} \psi_p^{\prime} \overline{\nabla \cdot \vec{v} \psi_p^{\prime A}} dAdp - \frac{1}{g} \iint f_0 \bar{\psi}_p \omega^{\prime} dAdp \\ & - \frac{1}{g} \iint \frac{f_0^2}{\sigma} \bar{\psi}_p R_d^{\prime} dAdp \end{aligned}$$

With the term on the left representing APE^{\prime} we get, for a unit area

$$\frac{\partial \langle APE \rangle}{\partial t} = \overbrace{\langle \bar{\alpha} \bar{\omega} \rangle}^A - \overbrace{\langle \frac{f_0^2}{\sigma} \nabla \bar{\psi}_p \cdot \bar{v} \bar{\psi}_p \rangle}^A - \overbrace{\langle \frac{f_0^2}{\sigma} R_d \bar{\psi}_p \rangle}^A - \overbrace{\langle \frac{f_0^2}{\sigma} \bar{\psi}_p^2 \rangle}^S \cdot \bar{n}$$

A-7-9

The last two terms of equations A-7-8 and 9 are a diabatic source-sink term, and a boundary flux term respectively.

The equations A-7-4, 5, 8, and 9 describe the energetics of the quasi-geostrophic portion of the flow. The boundary conditions can be minimized by selecting volumes that encompass a complete disturbance. The boundary conditions can contaminate results when the disturbance is entering or leaving the gridded region.

The transfers and conversions among the energy quantities are the processes shown in equation set III-3. We assume these are the important processes for evolution of the lee cyclone. These terms are evaluated instantaneously and time averaged over 12 hours to obtain the results shown in Figures IV-20, and 21. The resulting estimates are compared to actual changes in kinetic and available potential energy, and adjustments are made to insure a balance for each energy type for each data time. Implicitly contained within the adjustments are the boundary flux terms, non-parametrized processes and errors. The directions and magnitudes of the energy conversions or transfers are for quasi-geostrophic processes only. The adjustments will have no influence on the computed magnitude or direction of a particular energy conversion or transfer.